Matrix-producing neutrophils populate and shield the skin

Tommaso Vicanolo[1]†, Alaz Özcan[3]†, Jackson LiangYao Li[1,2]†, Carla Huerta-López[1], Iván Ballesteros[1], Andrea Rubio-Ponce[1], Andra C. Dumitru[1], Jose Ángel Nicolás-Ávila[1], Miguel Molina-Moreno[3], Pablo Reyes-Gutierrez[3], Andrew D. Johnston[4], Catherine Martone[5], Eric Greto[6], Antonio Quílez-Alvarez[1], Enrique Calvo[1], Elena Bonzon-Kulichenko[1,7], Rebeca Álvarez-Velez[1], Ming Yao Chooi[2,8], Immanuel Kwok[2], Blanca González-Bermúdez[9], Benoit Malleret[2,8], Francisco M Espinosa[10], Ming Zhang[11], Yu-Long Wang[12], Dasheng Sun[13], Shu Zhen Chong[2,8], Ali El-Armouche[12], Kevin K. Kim[13], Irina A. Udalova[14], Valentina Greco[5], Ricardo Garcia[10], Jesús Vázquez[1,15], Ana Dopazo[1, 15], Gustavo R. Plaza[9], Jorge Alegre-Cebollada[1], Stefan Uderhardt[6]¥, Lai Guan Ng[16]¥, Andrés Hidalgo[1,3]¥

[1] Centro Nacional de Investigaciones Cardiovasculares Carlos III, Madrid (Spain)
[2] Singapore Immunology Network (SIgN), Agency for Science, Technology and Research (A*STAR), 8A Biomedical Grove, Singapore 138648, Republic of Singapore
[3] Vascular Biology and Therapeutics Program and Department of Immunobiology, Yale University School of Medicine, New Haven, USA
[4] Department of Dermatology, Yale School of Medicine, New Haven, USA
[5] Department of Genetics, Yale University School of Medicine, New Haven, USA.
[6] Department of Internal Medicine 3 - Rheumatology and Immunology, Deutsches Zentrum für Immuntherapie (DZI), Friedrich-Alexander University Erlangen-Nürnberg (FAU) and Universitätsklinikum Erlangen, Erlangen 91054, Germany
[7] Biochemistry Area, Faculty of Environmental Sciences and Biochemistry, University of Castilla-La Mancha; Avenue Carlos III s/n, 45071 Toledo, Spain
[8] Department of Microbiology and Immunology, Immunology Translational Research Programme, NUS Yong Loo Lin School of Medicine, National University of Singapore, 117545 Singapore
[9] Center for Biomedical Technology, Universidad Politécnica de Madrid, 28223 Pozuelo de Alarcón, Spain and Departamento de Ciencia de Materiales, ETSI de Caminos, Canales y Puertos, Universidad Politécnica de Madrid, 28040 Madrid, Spain
[10] Instituto de Ciencia de Materiales de Madrid, CSIC, 28049 Madrid, Spain
[11] Department of Urology, Renji Hospital, School of Medicine, Shanghai Jiao Tong University, Shanghai 200127, China
[12] Department of Head and Neck Surgery, Fudan University Shanghai Cancer Center, Shanghai, China
[13] OPO and Organ Transplantation Leading Group,Renji Hospital, School of Medicine, Shanghai Jiao Tong University, 200127, China
[12] Institute of Pharmacology and Toxicology, Faculty of Medicine Carl Gustav Carus, Technische Universität Dresden, Dresden, Germany.
[13] Division of Pulmonary and Critical Care Medicine, Department of Internal Medicine, University of Michigan, Ann Arbor, Michigan
[14] Kennedy Institute of Rheumatology, University of Oxford, OX3 7FY, UK
[15] CIBER de enfermedades cardiovasculares (CIBERCV), Madrid 28029, Spain
[16] Shanghai Immune Therapy Institute, Shanghai Jiao Tong University School of Medicine affiliated Renji Hospital, Shanghai, China

† These authors contributed equally as first authors
¥ These authors contributed equally as corresponding authors: ahidalgo@cnic.es, Stefan.uderhardt@fau.de; nglaiguan@renji.com

Abstract

Defense from environmental threats is afforded by physical barriers that confer mechanical protection and prevent microbial entry. If microbes trespass those barriers, however, innate immune cells use toxic chemicals to kill the invading cells. While examining immune diversity across tissues, we discovered a population of neutrophils in the skin that expressed a broad repertoire of proteins and enzymes needed to build extracellular matrix (ECM). We show that, in the naïve skin, these matrix-producing neutrophils contributed to the composition and structure of the ECM, reinforced its mechanical properties, and promoted barrier function. Upon injury, these neutrophils built "rings" of matrix around wounds that shielded against foreign molecules and bacteria. This structural program relied on TGFβ signaling, such that disabling its receptor in neutrophils impaired ring formation around wounds and facilitated bacterial invasion. We infer that the innate immune system has evolved diverse strategies for defense, including one that physically shields the host from the outside world.

Organisms are protected from the outside world by dedicated barriers, among which the skin provides the main physical protection not only against mechanical injuries but also from the microbial ecosystems adapted to the outer side of the skin [1]. These barriers are typically built by layers of epithelial cells and a dense meshwork of fibrillar proteins produced by mesenchymal cells [2]. Once microbes enter the organism, however, new defense mechanisms are engaged to detect, trap, and kill the invading pathogens. While mechanisms of danger sensing inside the body can be provided by essentially any type of cell [3], innate immune leukocytes are particularly committed to pathogen eradication. A paradigmatic response against microbes that breach external barriers is that of neutrophils, a highly migratory leukocyte that rapidly detects and moves to areas of infection [4]. Once in contact with microbes, neutrophils produce and release a plethora of biochemical agents including anti-microbial peptides, highly-reactive chemicals as well as DNA-based traps (NETs) which, combined with their avid phagocytic capacity, allow for rapid elimination of the microbial threat, often at the cost of collateral damage to the host [5,6]. This biochemical response is believed to be the basis for microbial removal that preserves organismal health. Intriguingly, however, neutrophils also populate naïve tissues [7,8], and acquire phenotypic and functional states tailored to the needs of each tissue [9,10]. This functional diversity raises the possibility that neutrophils have evolved complementary strategies for organismal defense that are independent of microbial killing.

Here, we report the discovery of a population of neutrophils in the skin that produce extracellular matrix (ECM; herein matrix). We show that these neutrophils reinforce the barrier function of the skin by enhancing its structural and mechanical properties, thereby protecting from the infiltration of foreign molecules and microbes. We conclude that the innate immune system has evolved strategies to physically shield the organism from external challenges, even before these challenges occur.

Results

Matrix-producing neutrophils populate the skin

Using a combination of parabiosis and bulk transcriptomics, we previously found that neutrophils that infiltrate healthy tissues acquire distinct transcriptional signatures [9]. Reanalysis of this dataset across six different tissues for tissue-specific patterns of gene expression revealed that neutrophils from barrier tissues (lung, colon, and skin; see Extended Data Fig. 1A) displayed a signature associated with the ECM when compared with those from non-barrier tissues (blood, spleen and bone marrow; BM) (Fig.1A). This signature featured transcripts for most collagen-encoding genes as well as for other canonical matrix proteins that included fibronectin, laminins, fibrilins and elastin, transcripts related to metalloprotease activity (*Mmp* and *Adamts* genes), and transcripts for enzymes needed for fibril formation (Fig.1A; see all values in Data Table S1). Quantitative measurement of this signature in barrier versus non-barrier neutrophils revealed a strong and significant increase for genes encoding for collagens 1 and 3 and fibronectin (*Col1a1*, *Col3a1* and *Fn1*), and to a lesser degree laminin 3 (*Lama3*) and elastin (*Eln*), which were particularly prominent in the skin and gut (Fig.1B and Extended Data Fig.1B). Several lysyl oxidases and other genes needed for collagen maturation and assembly into fibers (Lox, Loxl2, Plod2 and Dpt) [11] were also prominent in the transcriptome of barrier neutrophils from the skin and the other barrier tissues (Fig.1B and Extended Data Fig.1B). Despite this unconventional signature, these neutrophils maintained their lineage identity (Extended Data Fig.1C) and retained the capacity to produce reactive oxygen species (ROS) and to phagocytose particles (Extended Data Fig.1D).

To determine whether these transcriptional signatures translated into protein, we first estimated the actual abundance of matrix-producing cells in the barrier tissues by staining neutrophils extracted from all tissues for Col3a1, a prototypical matrix protein found in our dataset. Col3a1+ cells were more abundant in barrier organs, as expected, with the highest frequency found in the skin, where one third of the isolated cells were positive for Col3 (Fig.1C). Direct examination of tissue-populating neutrophils by confocal imaging revealed even higher frequencies of Col3a1+ neutrophils in barrier organs, with up to ~75% of skin neutrophil positive for the protein, and volumetric rendering confirmed that Col3 was inside the cells (Fig.1D, Movie S1 and Extended Data Fig. 1E-F). When considered by tissue volume, the local density of Col3a1+ neutrophils was particularly high in the skin and gut (Extended Data Fig. 1G), although absolute numbers were higher in the lungs [7]. These matrix-producing neutrophils in barrier tissues (but not in blood) were also positive for other matrix proteins found in our transcriptional dataset, including Col1, Fn1 and Laminin (Extended Data Fig.1H). To ascertain that these neutrophils were *bona fide* producers of matrix proteins, we cultured sort-purified neutrophils from blood, lung and skin and tested for appearance of matrix protein over time. We found that neutrophils from barrier organs of wild type mice progressively increased the amount of detectable Col3a1 protein, whereas no signal was detected when neutrophils were extracted from the blood or from mice with neutrophil-specific deletion of the *Col3* gene (Extended Data Fig. 1I). We found comparable content of Col3a1+ neutrophils in the ear, back and plantar skin of mice (Extended Data Fig.1J), indicating their prevalence across skin regions. Importantly, we also found Col3a1+ neutrophils in barrier tissues of humans (Extended Data Fig.2A-C), suggesting conservation of this population of neutrophils across species. Thus, neutrophils populating the skin and other barrier tissues under steady-state conditions produce matrix proteins, an unexpected finding that prompted us to query the underlying mechanism and functional purpose of this program.

Neutrophils control circadian matrix transcription in the skin

We previously reported that neutrophils infiltrate most tissues in a circadian fashion, as they clear out from the circulation [7]. We predicted that, if neutrophils are relevant contributors to the matrix of barrier tissues, then their elimination should leave a temporal footprint in the circadian pattern of expression of such genes. We therefore speculated that temporal patterns, rather than absolute expression, might be a more reliable

proxy to assess the relevance of matrix-producing cells across tissues. We collected BM, lung, gut and skin tissues at multiple times over a full diurnal cycle from control and neutrophil-depleted mice (using a 2-day depletion schedule using the *MRP8*^{Cre}; Rosa26^{iDTR} mouse model of inducible neutropenia, herein iDTR mice; see Extended Data Fig.2D-E and [9]), and performed bulk transcriptomic analysis of the tissues (Fig.2A). Examination of over one hundred genes related to ECM proteins and enzymes in our circadian datasets using custom-built statistical tools [12] provided important insights. First, we found that several genes encoding for collagen isoforms and other matrix proteins like *Eln* and *Fn1* oscillated following strong circadian patterns, as did many *Adamts* and *Mmp* genes (see series for the skin in Extended Data Fig. 3). Second, we noticed that the circadian patterns of these genes aligned with the times at which neutrophils infiltrate most tissues (between ZT0-ZT10 [7], and Fig.2A). Finally, by plotting the differential expression of matrix genes in control versus neutrophil-depleted mice we found marked temporal alterations in the skin, with massive loss of circadian patterns of most matrix genes (almost 80% of genes lost circadianicity, seen as sinusoidal curves in Fig.2B). In contrast, the circadian loss of matrix transcription was mild to moderate in the marrow, lungs and intestine (shown as dominant flat lines in Fig.2B). Among the genes with full loss of circadian expression patterns in the skin we found *Col1a1*, *Col3a1*, *Col5* isoforms, *Eln* and *Fn1* (Fig.2C and Extended Data Fig.3), as well as one lysyl hydroxylase (*Loxl2*; Fig.2C). In general, neutropenia had distinct effects on gene expression patterns in each tissue (see representative comparisons for *Col3a1* in Extended Data Fig. 4A).

Because mesenchymal cells are prototypical matrix-producing cells across all organs, we considered the possibility of indirect effects of neutrophils on these or other cells as a potential cause of change in matrix production in tissues of neutropenic mice. To address this possibility, we purified CD90+ PDGFRα+ fibroblasts from lung and skin and compared their transcriptome in control versus neutropenic mice. Global analysis of principal components and volcano plots revealed, however, no significant alterations of global or matrix-related gene expression in lung or skin fibroblasts from neutropenic mice (Extended Data Fig. 4B), suggesting that neutrophils contribute directly to the matrix landscape by regulating the circadian dynamics of the matrix transcriptome. Given the relevance of barrier integrity in organismal defense, we examined the relevance of this structural immune program for skin physiology.

Neutrophils modulate skin composition and mechanics

We first examined the contribution of neutrophils to the matrix proteome by subjecting the skin of control and neutropenic mice to mass spectrometry. Using two complementary models of neutropenia (constitutive in *Lyz2*^{Cre}; *Mcl1*$^{fl/fl}$, herein Mcl1$^{\Delta N}$ mice [13]) and the inducible iDTR model, both characterized in Extended Data Fig.2), we found consistent changes in the relative abundance of collagen isoforms (Fig.2D and Data Table S2). We also examined post-translational modifications in Col3a1, a representative protein of the skin matrix, and found significant loss in lysine hydroxylation (Extended Data Fig. 4C and Data Table S3). Interestingly, this trend correlated with disrupted circadian expression in neutropenic mice of *Loxl2* (Fig.2C), one of the main enzymes involved in lysine hydroxylation in collagens [14].

The transcriptomic and proteomic analyses suggested that neutrophils contributed to the collagen composition and fiber formation in the skin. To assess if this was the case and to visualize the overall impact of neutrophils in matrix structure in this organ, we subjected the skin of control and neutropenic mice to scanning electron microscopy. This qualitative approach revealed conspicuous loss of collagen fiber thickness and density in the skin of mice depleted of neutrophils (Fig.2E). To define this loss quantitatively, we used second harmonic generation (SHG) through multiphoton imaging to visualize thousands of collagen fibrils from the skin of control and neutropenic mice by label-free microscopy (Fig.2F and Extended Data Fig. 5A), and measured fibril sizes using unbiased image-based tools [15]. Consistent with the electron microscopy data, we detected moderate but highly significant reductions in average fibril width in neutrophil-depleted mice (Fig.2F). We obtained similar results when assessing the morphology of fiber-like structures in the skin of these mice using Frangi filtering of volumetric SHG data (Extended Data Fig. 5B). Thus, neutrophils regulate protein composition and matrix structure in the naïve skin.

We next asked whether, and to what extent, the change in matrix structure would result in functional alterations in tissue mechanics. To address this question, we first performed mechanical stress-strain measurements on barrier tissues from constitutive neutropenic mice (Mcl1$^{\Delta N}$ mice; Fig.2G). We used a custom-built tensile tenser that allowed controlled stretching with concurrent measure of loading force (Extended Data Fig. 5C), a parameter that reflects tissue stiffness and is dictated by the tissue microstructure [16]. We found that neutropenia caused a significant loss of tensile stiffness in the skin, but not in the lung and gut (Fig.2G) and further confirmed this loss of skin stiffness in the inducible model of neutropenia (iDTR mice; Fig.2H). We next posited that the circadian pattern of neutrophil infiltration [7] might cause diurnal variations in the mechanical properties of the skin. Indeed, we found that the tensile stiffness of the skin manifested strong diurnal variations, and these variations were ablated upon neutrophil depletion (Extended Data Fig. 5D-F), suggesting dynamic remodeling of the matrix by neutrophils that infiltrate the skin. Together, these findings revealed that neutrophils control the dynamics of matrix homeostasis in the skin, such that their depletion altered the composition, fibrillary structure and overall mechanical properties of this tissue.

The remarkable control of matrix structure and mechanical properties of the skin contrasted with the reported low numbers of neutrophils in this tissue [7]. These studies, however, relied on flow cytometry, a technique that demands tissue dissociation, does not provide spatial information, and strongly underestimates cell numbers [17]. Hence, we used high-resolution volumetric imaging to determine the distribution and number of neutrophils more accurately in the native skin. Multiphoton 3D imaging of large ear skin explants at high spatial resolution revealed that neutrophils positioned in a sub-epidermal area rich in collagen fibers (Extended Data Fig. 6A-B), such that their elevated density was not random (Extended Data Fig. 6C). In contrast to this specific sub-epidermal compartment, neutrophils were evenly distributed (no difference compared with random) and at lower densities across the rest of the dermis (Extended Data Fig. 6C). Single-cell transcriptomic and imaging analyses demonstrated that neutrophils had substantially less matrix transcript and protein than fibroblasts (Extended Data Fig.6D-F), despite comparable intracellular Col3 on a per area basis (Extended Data Fig.6G). Consistently, imaging the skin of an inducible CNA35-mCherry reporter mouse model to track collagen deposited by specific cell types (model adapted from [18]; Extended Data Fig.7A-B) revealed that neutrophils released detectable collagen *ex vivo* and *in vivo* and, interestingly, deposited this collagen in the sub-epidermal region of the skin. In contrast, fibroblasts deposited larger amounts of collagens preferentially in the lower dermis (Extended Data Fig. 7C-E), revealing regional specialization of matrix-producing neutrophils.

We performed live imaging of reporter mouse lines to visualize the dynamics of extravascular neutrophils and fibroblasts in the naïve skin, using conditions that minimized experimental artifacts (Extended Data Fig.7F and Movie S2). We calculated that, due to their constant migration on the skin, neutrophils scanned the entire sub-epidermal surface in less than one hour despite the moderate densities present in this area (estimated 26.6 neutrophils/mm^2 from these live imaging experiments; Extended Data Fig.7F). This contrasted with fibroblasts, which were larger and more numerous but essentially immotile and only covered 16.9 ± 3.6% of the surface (Extended Data Fig.7G). We then examined whether the transit of neutrophils over specific areas of this subepidermal region would dynamically alter the structure of the matrix, as assessed by calculating 3D Frangi scores of collagen fibers by recording SGH over 30 min (Extended Data Fig.7H and Movie S3). Notably, only areas “visited” by neutrophils increased their Frangi values and this change was not seen outside these areas (Extended Data Fig.7I). Overall, these data revealed strong tropism of neutrophils to the subepidermal region of the skin, dynamic migration on this surface and remodeling of the collagen fibers, thereby providing insights into how these cells modulate the structural and mechanical properties of the skin.

TGFβ signaling drives the matrix program of neutrophils.

Although our data suggested that neutrophils could deposit matrix components in the skin and had only minor effects on fibroblasts (Extended Data Fig. 4B), we could not formally exclude the possibility that they

acted by influencing other cells. Thus, to define the actual contribution of matrix proteins specifically produced by neutrophils, we searched for cell-intrinsic drivers of this program using a simple qPCR-based in vivo screening strategy. Given the low numbers of neutrophils in the skin, for these analyses we harnessed the abundance of lung neutrophils[7] for the initial screening, which we subsequently validated in the skin.

We used mutant mice, or mice treated with antibodies and chemical antagonists to interfere with pathways known to drive neutrophil activation or maturation (GM-CSF, circadian time, NFκB, CXCR2 and CXCR4), with in vivo reprogramming (CXCR4, IFNγ, TGFβ), or generally associated with induction of matrix genes (Adbr3, iron transport and TGFβ), and examined alterations in the expression of a small collection of matrix signature genes by qPCR (*Col3a1*, *Eln* and *Lama3*, from Fig.1A), using their expression in blood neutrophils as reference (Fig.3A and Data Table S4). We identified three pathways that reproducibly affected matrix gene expression in lung neutrophils. These included CXCR2 and CXCR4, two chemokine receptors known to exert opposing roles in neutrophil development and function [19,20]. Consistently, interference with these receptors resulted in opposite effects in the matrix signature (Fig.3A). The third pathway was TGFβ signaling which, interestingly, is known to enhance CXCR4 signaling [21], the only other positive regulator found in our screening. We complemented this in vivo screening with the analysis of a chromatin accessibility dataset of neutrophils from the lung, blood, spleen and BM [9]. We found that a vast fraction (44.6%) of open chromatin sites specific for lung neutrophils were enriched in motifs recognized by the Smad2/3 transcription factors, which control the expression of TGFβ-induced genes [22] (Fig.3B). In line with this computational prediction, a fraction of lung neutrophils was positive for phospho-Smad3 staining, and this was absent in neutrophils from blood (Fig.3C). Hence, we hypothesized that acquisition of the matrix signature was driven by TGFβ signaling.

To formally examine this possibility, we generated mice with neutrophil-specific defects in TGFβ-signaling (MRP8^{CRE}; *Tgfbr2*$^{fl/fl}$ mice, herein TGFbR$^{\Delta N}$), which featured normal hematological parameters and neutrophil maturation in the BM (Extended Data Fig. 8A-B). We inspected matrix gene expression using Nanostring technology (Data Table S5) as well as global transcriptional changes by bulk RNA sequencing to examine alterations in the transcriptional program of lung neutrophils from these mice, using blood neutrophils as reference. Both approaches revealed remarkable reductions in matrix-associated gene expression (Extended Data Fig. 8C) and ECM-related programs in TGFbR$^{\Delta N}$ neutrophils (Fig.3D and Data Table S6). We validated these findings by assessing matrix protein expression in neutrophils from all tissues and found that disrupted TGFβ signaling resulted in marked loss of intracellular Col3 inside neutrophils from the skin, as well as the other barrier organs (Extended Data Fig. 8D-E). We confirmed these findings by using a different genetic driver (Ly6G^{CRE}; *Tgfbr2*$^{fl/fl}$ mice), in which skin neutrophils featured reduced intracellular Col3a1 protein, whereas protein content outside neutrophils was not altered (Extended Data Fig. 8F-G). Altogether, these data indicated that cell intrinsic TGFβ signaling drives the production of matrix by neutrophils.

We next examined whether disabled TGFβ signaling in neutrophils might alter the composition and mechanics of the naïve skin, as seen upon neutrophil depletion (Fig.2E-H). Although TGFbR$^{\Delta N}$ mice presented normal neutrophil numbers (Extended Data Fig. 9A) and skin anatomy (Extended Data Fig. 9B), ultrastructural analysis by SEM revealed disorganization of collagen fibrils in the skin of these mice (Fig.3E) and reduced fiber size (Fig.3F and Extended Data Fig. 9C). These structural alterations were matched by marked reductions in skin stiffness as assessed with the tensile tester (Fig.3G), indicating that tissue-specific programming of neutrophils through TGFβ supports the structural and mechanical properties of the skin. Interestingly, more sensitive mechanical measurements using atomic force microscopy of tissue explants were also able to detect reductions of stiffness in the lungs, but not the intestine, of TGFbR$^{\Delta N}$ mice (Extended Data Fig. 9D), thus extending the potential mechanical impact of neutrophils to other organs. To better understand how this program controlled the skin structure and mechanics, we performed TEM imaging of transversal skin sections and used automated imaging tools to measure thousands of fiber sections in

TGFbR$^{\Delta N}$ and littermate control mice. We found that overall fiber density was reduced in the TGFbR$^{\Delta N}$ skin (Extended Data Fig. 9E-F). By carefully inspecting these images, we noticed that the subepidermal region of WT mice contained a subset of large fibers (>0.02 μm^2 cross-section area), which were nearly absent in the lower dermis regions, a region where the presence of neutrophils is low (Extended Data Fig. 6C). Notably, these large fibers were completely absent in the subepidermal region of TGFbR$^{\Delta N}$ mice (Extended Data Fig. 9F-G), suggesting that neutrophils control the formation or compaction of large fibers specifically in the subepidermal region, but not in deeper areas of the skin.

These observations also raised the possibility that impairment of this program might render the skin more permeable to external molecules. Consistent with this hypothesis, we found that the small fluorescent compound Evans blue (~1 KDa) diffused much more through the skin of TGFbR$^{\Delta N}$ mice than in control animals (Fig.3H). The effect was specific to the skin matrix since permeability to this dye was not affected in other tissues, including lung, intestine, and multiple vascular beds (Extended Data Fig. 9H), and the integrity of the epithelial layer of the skin remained intact in TGFbR$^{\Delta N}$ mice as assessed by unaltered transepidermal water loss (not shown). We could reproduce the alterations in permeability and skin mechanics using the Ly6G^{CRE}; *Tgbr2*$^{fl/fl}$ model, or when neutrophils were depleted with anti-Ly6G antibodies (Extended Data Fig. 9I-J). Interestingly, elimination only of the *Col3a1* gene from neutrophils (Col3A1$^{\Delta N}$ mice) did not alter skin stiffness or permeability relative to littermate controls (not shown), suggesting that the full matrix program induced by TGFβ is needed for neutrophils to regulate these barrier properties of the skin. Thus, matrix producing neutrophils potentiate the barrier function of the naïve skin against potential environmental threats.

Neutrophils build matrix “rings” that shield skin wounds

We reasoned that these barrier-supporting functions of neutrophils might also be relevant during a barrier breach. To address this possibility, we used a model of localized micro wounds caused by needle puncture across the full thickness of the ear skin (see Methods). In this model, we noticed that the healing process occurred in at least two stages: an early phase of wound enlargement (days 1-4) followed by contraction and finally wound closure (days 5-9) (Fig.4A and Extended Data Fig. 10A-B). We found that the early enlargement phase was slightly delayed in neutropenic mice (Extended Data Fig. 10C), a finding that agreed with imaging of wounds of Ly6G^{tdTom} reporter mice revealing early (day 1) and massive recruitment of neutrophils that “cauterized” the wound by removing the proximal tissue around it (Fig.4A and Extended Data Fig. 10A). Interestingly, we also noticed a second wave that surrounded the enlarged wound by day 2, and these neutrophils were strongly immune-reactive for Col3a1 (Fig.4A-C). Timestamp experiments using iLy6G^{CreERT2} mice[9] suggested that both waves of neutrophils originated from the BM and blood (Extended Data Fig.10D), suggesting local acquisition of the matrix program in the skin. Live imaging in LysM-GFP mice suggested that the initially recruited neutrophils that created the extended lesion died after the first day, whereas neutrophils recruited to the periphery of the extended lesion were still motile up to day 3 (Movie S4). Expression of Col3a1 in this second wave of neutrophils, but not their migration into the wound, was controlled by TGFβ signalling because these neutrophils were largely negative for Col3a1 in TGFbR$^{\Delta N}$ mice (Fig.4C-D).

Given the similarity with the population of matrix-producing neutrophils seen in the naïve skin, we focused our attention on this second wave Col3a1+ neutrophils that surrounded the wounded area. We noticed that the recruitment of these Col3a1+ neutrophils coincided with the formation of an optically dense, matrix-rich ring around the wounds that could be as large as 1 mm in diameter, was strongly positive for Col3a1 (Fig.4E and Movie S5) and persisted until late stages of healing (Fig.4F), a time when neutrophils were no longer present (Fig.4A). These structures were additionally positive for other proteins expressed by barrier neutrophils, including Col1, Col4, Laminin and Elastin (Extended Data Fig. 10F). Formation of this matrix-rich ring was compromised when we depleted neutrophils (iDTR model), or in mice in which only neutrophils lacked TGFβ signalling (using TGFbR$^{\Delta N}$ mice or Ly6G^{Cre}; *Tgfbr2*$^{fl/fl}$ mice; Fig.4G and Extended Data Fig.

10G). Even in instances in which neutrophil depletion was partial, Col3a1 deposits appeared in patches that coincided with the few persisting neutrophils (Extended Data Fig. 10H). We examined changes in protein content by unbiased proteomic analysis of the wounded skin and found consistent loss in collagens and fibrinogen both in neutropenic and TGFbR$^{\Delta N}$ mice (Extended Data Fig. 10I, see values in Data Table S7), which was consistent with defective formation of matrix rings in these mice. Of note, we found that a fraction of monocytes and macrophages present in wounds also stained positive for Col3a1 (data not shown), suggesting possible contributions of these other lineages to matrix deposition. However, we show here that no other cells can compensate for matrix ring formation when neutrophils are depleted or genetically impaired in the TGFbR$^{\Delta N}$ mice (Fig.4G and Extended Data Fig.10G).

Neutrophils have been recently shown to carry matrix proteins pre-formed by other cells in the context of internal injury [18,23]. Although analysis of the *Tgbr2* mutants strongly suggested that skin neutrophils produced their own matrix in wounds, we used an additional approach to examine if they also transported pre-formed matrix to the wounds. To this end, we generated Mrp8^{CRE}; *Col3a1*$^{fl/fl}$ mice to delete this matrix gene only in neutrophils (Extended Data Fig. 11A-B), and confirmed that Col3 protein was reduced in neutrophils, but not fibroblasts, from these mice (Extended Data Fig. 11C). Importantly, we found that Col3a1 was absent from skin micro-wounds in these mice (Fig.4H), whereas a different matrix protein was unchanged (laminin; Extended Data Fig. 11D). Thus, neutrophils recruited to the wound's periphery produce and deposit matrix-rich rings, and this process relies on neutrophil-intrinsic TGFβ signalling.

The presence of neutrophil-derived matrix-rich deposits around wounded areas raised the intriguing possibility that neutrophils built physical shielding structures to prevent the entry of noxious molecules or microorganisms into the sterile tissue. To address this possibility, we exposed the surface of day 3 wounds to Evans Blue and examined its diffusion into the surrounding tissue (scheme in Fig.4I). We found that mice depleted of neutrophils, or with neutrophil-specific deficiency in TGFβ signaling, had enhanced diffusion of the dye, indicating a more permeable architecture around wounds (Fig.4I). We finally tested whether these matrix-rich structures also prevented the penetration of larger, common skin commensal or pathogenic bacteria. We transiently exposed day 3 wounds to a suspension of *Staphylococcus aureus* and assessed the number and distribution of bacteria in the wounded tissue. In line with our prediction, the bacteria expanded more and penetrated deeper in the wounds of TGFbR$^{\Delta N}$ mice relative to control animals (Fig.4J-K), and this was not caused by defective immune activity of neutrophils in these mice (Extended Data Fig. 12A). Interestingly, Col3a1$^{\Delta N}$ mice were also more susceptible to bacteria penetration, revealing a significant contribution of neutrophil-derived Col3 in limiting pathogen spread through wounds (Extended Data Fig. 12B). Hence, matrix-producing neutrophils build matrix shields that protect from the entry of small molecules and microorganisms into the sterile tissue when the barrier integrity is compromised (Extended Data Fig. 12C).

Discussion

Effective defense from external aggressions has been traditionally compartmentalized into discrete biological entities: a physical barrier built by structural cells (including epithelial and mesenchymal cells) and a biochemical barrier that entails deployment of phagocytic and cytotoxic responses upon microbial entry and is mediated by innate immune cells. Our findings challenge this conceptual and functional divide by showing that neutrophils, the prototypical first responders to infections and injury, are also capable of reinforcing the barrier properties of the skin, thereby reducing the entry of microbes and potential toxins into the host. We show that this immune-structural program is specific to neutrophils from barrier tissues and engages a discrete signalling pathway (TGFβ) typically associated with matrix deposition by mesenchymal cells [24]. Notably, this same cytokine orchestrates a wealth of additional immune programs across barrier tissues including the specification of alveolar macrophages in lungs, Langerhans cells in the skin and IL17-producing T cells in the gut [25–27], suggesting that neutrophils are part of a larger, coordinated immune program in border regions. Beyond these tissue-specific programs, our findings support a model whereby

the innate immune system not only kills microbes, but actively prevents invasion. This notion has been illustrated by the recent discovery of macrophages sampling fluids in the colon before intestinal absorption [28] and, as shown here, by directly reinforcing passive skin barriers to prevent infection. We foresee potential evolutionary advantages to this strategy, among which the most immediate is the protection of bystander host tissues from highly unspecific and toxic microbicidal responses [6]. The finding that the effect of neutrophils on barrier function are largely restricted to the skin was unexpected given the presence of these matrix-producing cells, albeit at lower frequencies, in the lungs and intestine. This may be partly explained by the distinct abundance and localization of neutrophils in collagen-rich areas of the skin. We do not rule out, however, additional contributions of this program in the other barrier tissues, but these appear to be macroscopically minor and may escape the sensitivity of our approaches, and is an area of future exploration.

Intriguing associations between innate immunity and structural elements have been reported. For example, pre-emptive organismal defense by neutrophils is suggested by the presence of granulocytes within the outer shell of the lungfish [29], although their contribution to mechanical or biochemical functions in this context has not been tested. Physical barriers can also be organized by innate immune cells such as macrophages, which orchestrate the formation of fibrin clots to physically entrap bacteria and seal wounds within serosal cavities [30,31], or modulate the content of collagens around arteries by eliciting mesenchymal activation [32]. In the context of sterile injury, neutrophils have been shown to transport preformed matrix to heal tissues [18] and to contribute to renal fibrosis in part by depositing Col1 [33]. Together with our discovery that barrier-associated neutrophils specialize in producing matrix both in the naïve and wounded skin, it appears that the protective toolbox of innate immune cells is more diverse than anticipated in that it includes production, transport and remodelling of the extracellular matrix, which ultimately serves to reinforce, rebuild, or physically protect the body's inner and outer barriers. This structural protection conferred by neutrophils complements in non-redundant ways the barrier function provided by professional matrix producers, such as fibroblasts, by regulating the matrix dynamics of specific regions of the skin. This is illustrated by the remarkable dynamism of fiber remodelling, diurnal control of skin mechanics, and the rapid sealing of wounds that we show here to be regulated by neutrophils. The unique capacity of neutrophils to migrate and rapidly reach areas inaccessible to other matrix-producing cells is likely to account for this distinct control of structural dynamics.

Our study is limited by the relatively small number of tissues and physiological scenarios explored so far, which should be extended to dissect the contribution of this immune program in the lungs and intestine, where other sources of matrix components appear to be more dominant. Other limitations are the yet unknown source of TGFβ or other possible signals that instruct this unique program in barrier neutrophils, the potential capacity of these neutrophils to also degrade pre-existing matrix, which is not addressed here, and the lack of tools to measure more precisely the extent to which neutrophils contribute to overall matrix quantity and quality (including post-translational modifications) in primary tissues. We are currently generating tools to address these limitations and to tackle new questions at the immune-structural interface. Indeed, our findings raise broader physiological questions in light of the signalling properties of certain matrix proteins, such as Col3 in the context of cancer dormancy [34], or during natural tissue remodelling and repair [35]. The finding that barrier properties vary following circadian patterns of neutrophil infiltration [7] should incite revision of barrier dynamics so as to define the precise alterations in matrix structure and barrier functions in individuals suffering immune anomalies, including patients with neutrophilic dermatoses, systemic neutropenia or other immune alterations associated with diabetes, obesity or organismal age. It is indeed possible that the heightened susceptibility of these individuals to infections and associated morbidities originate from structural, rather than just microbicidal, defects.

References

1. Erin Chen, Y., Fischbach, M. A. & Belkaid, Y. Skin microbiota-host interactions. *Nature* **553**, 427–436 (2018).
2. Driskell, R. R. *et al.* Distinct fibroblast lineages determine dermal architecture in skin development and repair. *Nature* **504**, 277–281 (2013).
3. Krausgruber, T. *et al.* Structural cells are key regulators of organ-specific immune responses. *Nature* **583**, 1–7 (2020).
4. Nourshargh, S. & Alon, R. Leukocyte Migration into Inflamed Tissues. *Immunity* vol. 41 694–707 at https://doi.org/10.1016/j.immuni.2014.10.008 (2014).
5. Burn, G. L., Foti, A., Marsman, G., Patel, D. F. & Zychlinsky, A. The Neutrophil. *Immunity* vol. 54 1377–1391 at https://doi.org/10.1016/j.immuni.2021.06.006 (2021).
6. Phillipson, M. & Kubes, P. The neutrophil in vascular inflammation. *Nat. Med.* **17**, 1381–1390 (2011).
7. Casanova-Acebes, M. *et al.* Neutrophils instruct homeostatic and pathological states in naive tissues. *J. Exp. Med.* **215**, 2778–2795 (2018).
8. Casanova-Acebes, M. *et al.* Rhythmic Modulation of the Hematopoietic Niche through Neutrophil Clearance. *Cell* **153**, 1025–1035 (2013).
9. Ballesteros, I. *et al.* Co-option of Neutrophil Fates by Tissue Environments. *Cell* **183**, 1282-1297.e18 (2020).
10. Becher, B. *et al.* High-dimensional analysis of the murine myeloid cell system. *Nat. Immunol.* **15**, 1181–1191 (2014).
11. Theocharis, A. D., Manou, D. & Karamanos, N. K. The extracellular matrix as a multitasking player in disease. *FEBS J.* **286**, 2830–2869 (2019).
12. Rubio-Ponce, A. *et al.* Combined statistical modeling enables accurate mining of circadian transcription. *NAR Genomics Bioinforma.* **3**, 1–9 (2021).
13. Csepregi, J. Z. *et al.* Myeloid-Specific Deletion of Mcl-1 Yields Severely Neutropenic Mice That Survive and Breed in Homozygous Form. *J. Immunol.* **201**, 3793–3803 (2018).
14. Puente, A. *et al.* LOXL2—A new target in antifibrogenic therapy? *Int. J. Mol. Sci.* **20**, 1–12 (2019).
15. Bredfeldt, J. S. *et al.* Computational segmentation of collagen fibers from second-harmonic generation images of breast cancer. *J. Biomed. Opt.* **19**, 16007 (2014).
16. Chaudhuri, O., Cooper-White, J., Janmey, P. A., Mooney, D. J. & Shenoy, V. B. Effects of extracellular matrix viscoelasticity on cellular behaviour. *Nature* **584**, 535–546 (2020).
17. Gomariz, A. *et al.* Quantitative spatial analysis of haematopoiesis-regulating stromal cells in the bone marrow microenvironment by 3D microscopy. *Nat. Commun.* **9**, (2018).
18. Fischer, A. *et al.* Neutrophils direct preexisting matrix to initiate repair in damaged tissues. *Nat. Immunol.* **23**, 518–531 (2022).
19. Adrover, J. M. *et al.* A Neutrophil Timer Coordinates Immune Defense and Vascular Protection. *Immunity* **50**, 390-402.e10 (2019).
20. Martin, C. *et al.* Chemokines acting via CXCR2 and CXCR4 control the release of neutrophils from the bone marrow and their return following senescence. *Immunity* **19**, 583–593 (2003).
21. Buckley, C. D. *et al.* Persistent Induction of the Chemokine Receptor CXCR4 by TGF-β1 on Synovial T Cells Contributes to Their Accumulation Within the Rheumatoid Synovium. *J. Immunol.* **165**, 3423–3429 (2000).

22. Feng, X. H. & Derynck, R. Specificity and versatility in TGF-β signaling through smads. *Annual Review of Cell and Developmental Biology* 659–693 at https://doi.org/10.1146/annurev.cellbio.21.022404.142018 (2005).

23. Wang, S. *et al.* Venular basement membranes contain specific matrix protein low expression regions that act as exit points for emigrating neutrophils. *J. Exp. Med.* **203**, 1519–1532 (2006).

24. Meng, X. M., Nikolic-Paterson, D. J. & Lan, H. Y. TGF-β: The master regulator of fibrosis. *Nat. Rev. Nephrol.* **12**, 325–338 (2016).

25. Borkowski, T. A., Letterio, J. J., Farr, A. G. & Udey, M. C. A role for endogenous transforming growth factor β1 in Langerhans cell biology: The skin of transforming growth factor β1 null mice is devoid of epidermal Langerhans cells. *J. Exp. Med.* **184**, 2417–2422 (1996).

26. Mangan, P. R. *et al.* Transforming growth factor-β induces development of the T H17 lineage. *Nature* **441**, 231–234 (2006).

27. Yu, X. *et al.* The Cytokine TGF-β Promotes the Development and Homeostasis of Alveolar Macrophages. *Immunity* **47**, 903-912.e4 (2017).

28. Chikina, A. S. *et al.* Macrophages Maintain Epithelium Integrity by Limiting Fungal Product Absorption. *Cell* **183**, 411-428.e16 (2020).

29. Heimroth, R. D. *et al.* The lungfish cocoon is a living tissue with antimicrobial functions. *Sci. Adv.* **7**, eabj0829 (2021).

30. Zindel, J. *et al.* Primordial GATA6 macrophages function as extravascular platelets in sterile injury. *Science (80-.).* **371**, 0–13 (2021).

31. Vega-Pérez, A. *et al.* Resident macrophage-dependent immune cell scaffolds drive anti-bacterial defense in the peritoneal cavity. *Immunity* **54**, 2578-2594.e5 (2021).

32. Lim, H. Y. *et al.* Hyaluronan Receptor LYVE-1-Expressing Macrophages Maintain Arterial Tone through Hyaluronan-Mediated Regulation of Smooth Muscle Cell Collagen. *Immunity* **49**, 326-341.e7 (2018).

33. Ryu, S. *et al.* Siglec-F–expressing neutrophils are essential for creating a profibrotic microenvironment in renal fibrosis. *J. Clin. Invest.* **132**, (2022).

34. Di Martino, J. S. *et al.* A tumor-derived type III collagen-rich ECM niche regulates tumor cell dormancy. *Nat. Portf.* (2021) doi:10.1038/s43018-021-00291-9.

35. Bonnans, C., Chou, J. & Werb, Z. Remodelling the extracellular matrix in development and disease. *Nat. Rev. Mol. Cell Biol.* **15**, 786–801 (2014).

36. Hasenberg, A. *et al.* Catchup: A mouse model for imaging-based tracking and modulation of neutrophil granulocytes. *Nat. Methods* **12**, 445–452 (2015).

37. Tauriello, D. V. F. *et al.* TGFβ drives immune evasion in genetically reconstituted colon cancer metastasis. *Nature* **554**, 538–543 (2018).

38. Adrover, J. M. *et al.* Programmed ‘disarming’ of the neutrophil proteome reduces the magnitude of inflammation. *Nat. Immunol.* **21**, 135–144 (2020).

39. Li, J. L. *et al.* Intravital multiphoton imaging of immune responses in the mouse ear skin. *Nat. Protoc.* **7**, 221–234 (2012).

40. Buenrostro, J. D., Giresi, P. G., Zaba, L. C., Chang, H. Y. & Greenleaf, W. J. Transposition of native chromatin for fast and sensitive epigenomic profiling of open chromatin, DNA-binding proteins and nucleosome position. *Nat. Methods* **10**, 1213–1218 (2013).

41. Wiśniewski, J. R., Zougman, A., Nagaraj, N. & Mann, M. Universal sample preparation method for proteome analysis. *Nat. Methods* **6**, 359–362 (2009).

42. Navarro, P. *et al.* General statistical framework for quantitative proteomics by stable isotope

labeling. *J. Proteome Res.* **13**, 1234–1247 (2014).

43. Bonzon-Kulichenko, E., Garcia-Marques, F., Trevisan-Herraz, M. & Vázquez, J. Revisiting peptide identification by high-accuracy mass spectrometry: Problems associated with the use of narrow mass precursor windows. *J. Proteome Res.* **12**, 700–710 (2015).

44. Uderhardt, S., Martins, A. J., Tsang, J. S., Lämmermann, T. & Germain, R. N. Resident Macrophages Cloak Tissue Microlesions to Prevent Neutrophil-Driven Inflammatory Damage. *Cell* **177**, 541-555.e17 (2019).

45. Li, W., Germain, R. N. & Gerner, M. Y. High-dimensional cell-level analysis of tissues with Ce3D multiplex volume imaging. *Nat. Protoc.* **14**, 1708–1733 (2019).

46. Lämmermann, T. *et al.* Neutrophil swarms require LTB4 and integrins at sites of cell death in vivo. *Nature* **498**, 371–375 (2013).

47. Li, X. *et al.* Reinforcing neuron extraction and spike inference in calcium imaging using deep self-supervised denoising. *Nat. Methods* **18**, 1395–1400 (2021).

48. Frangi, A. F., Niessen, W. J., Vincken, K. L. & Viergever, M. A. Multiscale vessel enhancement filtering. in *Lecture Notes in Computer Science (including subseries Lecture Notes in Artificial Intelligence and Lecture Notes in Bioinformatics)* (1998). doi:10.1007/bfb0056195.

49. Saqlain, F., Popa, I., Fernández, J. M. & Alegre-Cebollada, J. A novel strategy for utilizing voice coil servoactuators in tensile tests of low volume protein hydrogels. *Macromol. Mater. Eng.* **300**, 369–376 (2015).

50. Butt, H. J. & Jaschke, M. Calculation of thermal noise in atomic force microscopy. *Nanotechnology* **6**, 1–7 (1995).

51. Bankhead, P. *et al.* QuPath: Open source software for digital pathology image analysis. *Sci. Rep.* (2017) doi:10.1038/s41598-017-17204-5.

52. Chua, R. Y. R. & Wong, S. H. SNX3 recruits to phagosomes and negatively regulates phagocytosis in dendritic cells. *Immunology* **139**, 30–47 (2013).

Acknowledgements: We thank Marta Dueñas, Lorena Montesino, María Vara, Javier Nieto, Yinhui Qian, Tariq Khoyratty, Sergio Callejas, Danay Cibrián and Laura Morales for technical and analytical support with Nanostring analysis, biomechanical and proteomic experiments, and members of the Hidalgo lab for animal husbandry and discussion. Chen John Yu-Shen kindly provided material assistance with our in vitro bacterial killing assays. We thank the SIgN mouse core facility for technical help and support, SIgN flow cytometry team for assistance with cell sorting and the SIgN functional genomics and SIgN computational immunology team (Nicholas Ang, Lau Mai Chan, Duan Kaibo) for expertise and assistance on transcriptomics, Daniel Lopez for help with the infection experiments, and the Center for Cellular and Molecular Imaging, Electron Microscopy Facility at Yale Medical School for assistance.

Funding:
The project that gave rise to these results received the support of a fellowship from La Caixa Foundation (ID 100010434) with fellowship code LCF/BQ/DR21/11880022 and from Boehringer Ingelheim Fonds to T.V.; A.O. was supported by the Swiss National Science Foundation (P500PB-206852), J.A.N-A was supported by fellowship SVP-2014-068595 and J.L.L. was supported by A*STAR and a Juan de la Cierva JCI-2017-33136 Fellowship from Ministerio de Ciencia e Innovación (MCIN). C.H.L. was the recipient of an FPI predoctoral fellowship (BES-2015-073191). A.C.D. was supported by a Marie Curie Individual Fellowship DILEMMA 101065552 and from the ”La Caixa” Foundation (ID 100010434) under the agreement LCF/BQ/PI22/11910029. A.H. was supported by grant R01AI165661 from NIH/NIAD, RTI2018-095497- B-I00 from MCIN, HR17_00527 from Fundación La Caixa, the Transatlantic Network of Excellence (TNE-18CVD04) from the Leducq Foundation, and FET-OPEN (no. 861878) from the European Commission. L.G.N is supported by National Natural Science Foundation of China (Grant numbers 32270956 and 92374205). G.R.P., R.G. and J.A-C. were supported by Grant Tec4Bio-CM/P2018/NMT-4443 from the Comunidad de Madrid. K.K. was supported by grants NHLBI R01HL156998 and NHLBI R01HL153056 from NIH. I.A.U. was supported by the Wellcome Trust Investigator Award no. 209422/Z/17/Z for neutrophil. J.V. was supported by grants PGC2018-097019-B-I00 from MCIN, PRB3 (PT17/0019/0003- ISCIII-SGEFI / ERDF, ProteoRed from the Instituto de Salud Carlos III (Fondo de Investigación Sanitaria) and HR17-00247 from Fundación La Caixa. genomics work. S.U. was supported by the Hightech Agenda Bayern, the European Research Council (no. 101039438) and the Deutsche Forschungsgesellschaft (DFG; no. 447268119, 448121430, 405969122). I.B. was supported by grants from MICIN (RYC2020-029563-I and PID2022-140534NB-I00). Volumetric imaging was performed at the Optical Imaging Centre Erlangen (OICE, FAU) funded by DFG (project 261193037). J.L.L and C.S.Z. were supported by the Singapore Immunology Network (SIgN) and the Agency for Science, Technology and Research (A*STAR). The CNIC is supported by the MCIN and the Pro CNIC Foundation and is a Severo Ochoa Center of Excellence (CEX2020-001041-S).

Author contributions:
Conceptualization: A.H.
Data Curation: T.V., A.O., J.L.L., C.H-L., I.B., A.R-P., A.C.D., M.M-M., E.C., E.B-K.
Formal analysis: T.V., A.O., J.L.L., C.H., I.B., A.R-P, A.C.D., M.M-M.
Funding acquisition: A.C.D., A.E-A., K.K., I.A.U., J.V., G.R.P., J.A-C., S.U., L.N., A.H.
Investigation: T.V., A.O., J.L.L., C.H-L., I.B., A.C.D., E.C., J.A.N-A., A.D.J., C.M., F.M.E., A.Q-A., E.B-K., R.A-V., E.G., S.Z.C., M.Y.C., I.K., B.G-B., B.M.
Methodology: T.V., A.O., J.L.L., C.H-L, A.C.D., E.C.
Project administration and supervision: A.H.
Resources: M.Z., Y-L W., D.S., V.G., R.G., A.E-A., K.K., I.A.U., A.D., C.S.Z., G.R.P., J.V., J.A.-C., S.U., L.N., A.H.
Software: A.R-P., M.M-M.
Validation: T.V., A.O., J.L.L., A.H.
Visualization: T.V., A.O., J.L.L., A.H.
Writing: T.V., A.O., J.L.L., and A.H. wrote the original draft which was reviewed by all authors.

Competing interest:
The authors declare no conflicts of interest.

Data and materials availability: All the transcriptomics data are available in Gene Expression Omnibus (GEO) and proteomics data in Proteomics Identification Database (PRIDE). The individual GEO accession numbers are as follows: bulk RNA-seq from neutrophils in parabiotic tissues (GSE141745); bulk RNA-seq from tissues at varying circadian timepoints (GSE198770); bulk RNA-seq from TGFbR$^{\Delta N}$ neutrophils (GSE198654); bulk RNA-seq from skin and lung fibroblasts (GSE202738); ATAC-seq from tissue neutrophils (GSE141285). For proteomics data, they have been deposited to the ProteomeXchange Consortium via the PRIDE partner repository with the dataset identifiers as follows: blood and lung cell lysates (PXD031943); neutropenic tissues (PXD031950); and wounded skin tissue (PXD031952).

Extended Data

Materials and Methods

Supplementary Text

Extended data Figs. 1 to 12

References (36–52)

Legends for Movies S1 to S3

Data Tables S1 to S7

Figures and Figure legends

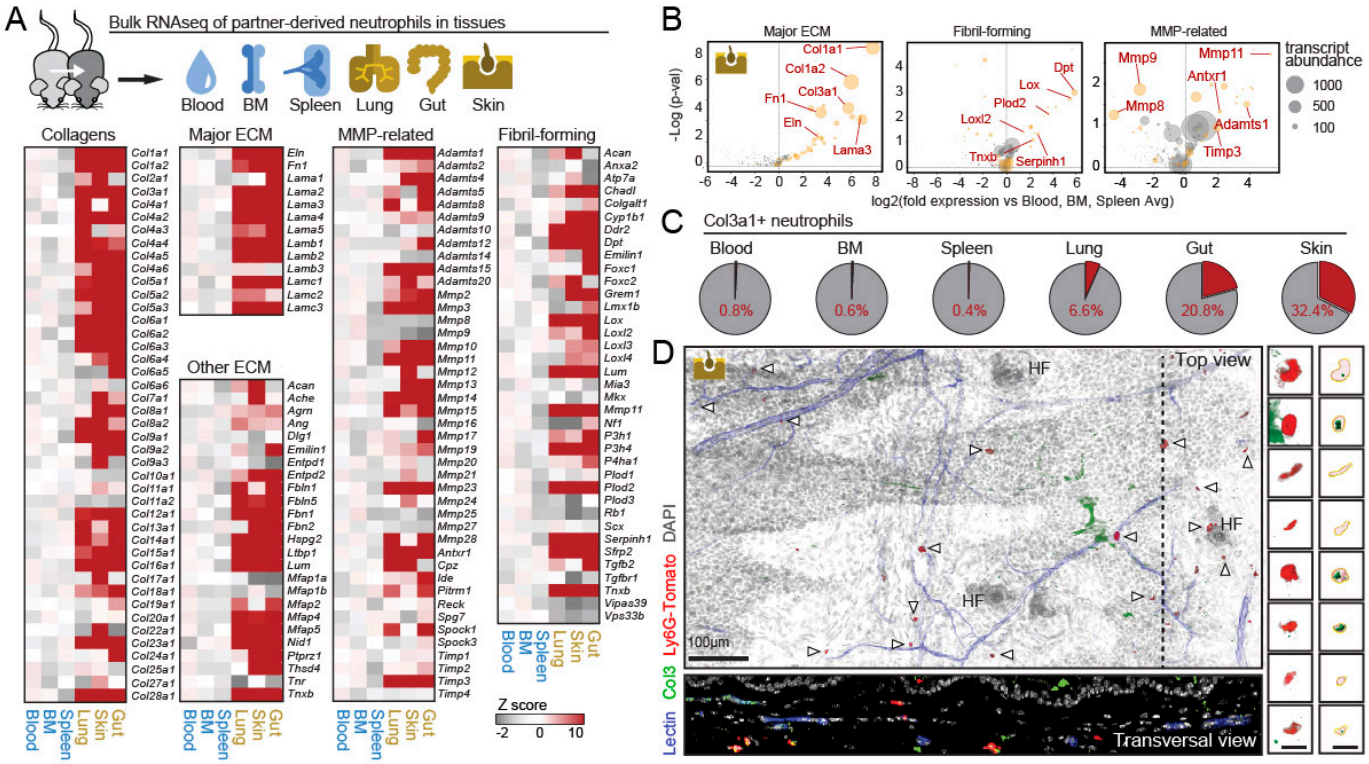

Figure 1. Matrix-producing neutrophils populate the skin. (A) Top, parabiosis strategy to analyze blood-borne neutrophils that infiltrate internal (blood, bone marrow and spleen) and barrier tissues (lung, skin and gut). Bottom, heatmap showing the relative expression of genes associated with the ECM, with increases for most collagens and other ECM proteins, metalloproteases (MMP) and enzymes involved in fibril formation and maturation. Data is from 3 mice per tissue. (B) Volcano plots of data from (A) showing paired comparison of matrix genes from skin neutrophils versus combined blood, BM and spleen, indicating the genes most differentially expressed in each tissue. (C) Pie charts showing the frequency of neutrophils positive for matrix protein (Col3a1) across tissues, as determined by immunofluorescence of isolated cells. Data are averages of 3 mice. (D) Top and transversal views of a representative immunofluorescence of the naïve skin of a Ly6G$^{CRE;\ Tomato}$ mouse, showing neutrophils (red, marked by triangles), vessels (blue), nuclei (grey) and Col3 protein (green). Insets show raw (left) and corresponding segmented images (right) of representative neutrophils with or without intracellular Col3. The dashed line indicates the region chosen for the transversal view. The image is representative of 5 mice. HF, hair follicles. See also Movie S1.

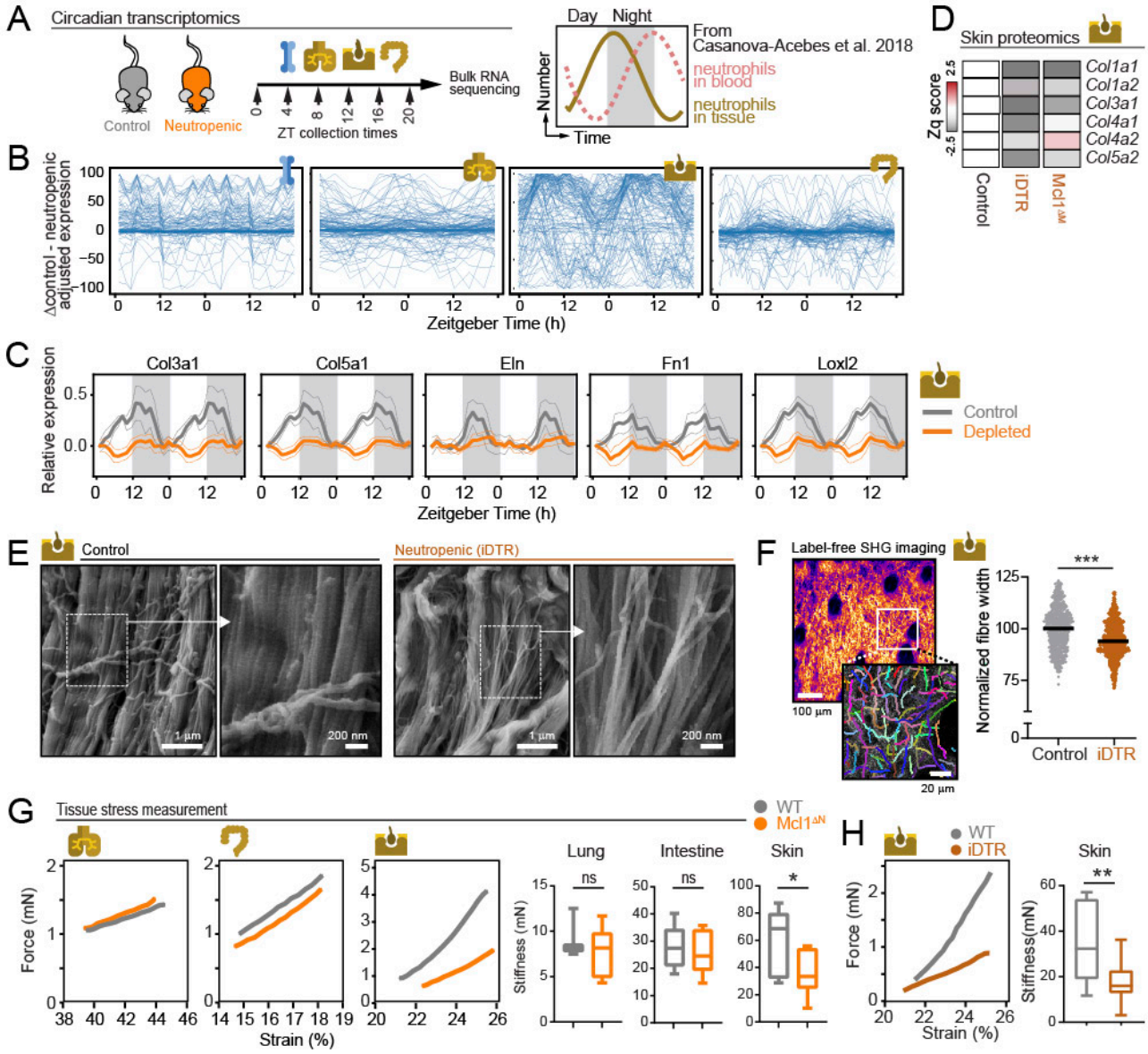

Figure 2. Neutrophils control matrix composition, structure, and mechanics of the naïve skin. (A) Strategy based on collection at multiple diurnal times to determine the circadian transcription in tissues of control and neutropenic mice and control littermates. Right, schematic of neutrophil dynamics in blood versus tissues modelled from [7]. (B) Summary of the effect of neutrophil depletion in the circadian transcription of 124 matrix-related genes (shown in Extended Data Fig.3 for skin), assessed by bulk RNA sequencing. Data is shown as the transcript read values for each gene and time-point in neutropenic mice subtracted from the same gene, times and tissues in control mice, such that flat lines mean no effect in the circadian pattern of expression. (C) Examples of matrix genes whose expression is circadian in the skin of control mice and the circadian pattern is completely lost in the skin of neutropenic mice. Smoothed data is from three mice per time and gene, with confidence intervals (estimated SEM) shown as thin dotted lines. (D) Matrix proteome of the skin of control and two neutropenic mouse models ($Mcl1^{\Delta N}$ and iDTR mice; collected at ZT7), showing a clear decline of most collagen proteins. Each data box is the average from 3 mice. Controls were Cre^{NEG} $Mcl1^{fl/fl}$ littermates also treated with DT. (E) Representative scanning electron microscopy images of the ear skin from 4 mice per group, showing collagen bundles in Cre^{NEG} control mice that are disorganized in neutropenic mice (7day depletion, iDTR model). (F) Images obtained by multiphoton microscopy and SHG and transformed into individual fibers whose width was measured using an automated software (left). Data shown is from 26-36 z-slices per location from 4 different locations per mouse, from 5 mice per group. Each dot represents the average value of approximately 1000 individual analyzed fibers from a single 510 µm by 510 µm z-slice image. Controls were Cre-negative littermates treated with DT. (G) Representative force-strain curves showing force at given strains for each of the indicated tissues in control Cre^{NEG} $Mcl1^{fl/fl}$ littermates and neutropenic mice ($Mcl1^{\Delta N}$). Shown is one example for each group and tissue. Stiffness (in mN) is quantified as the slope of the force-strain curves as in the box and whiskers plots to the right. (H) Force-strain analyses in the acute iDTR neutropenic mice compared with control Cre^{NEG} littermates, both treated with DT. Data in (G) and (H) are from 12 mice per group. Analyses in (F-H) are compared by unpaired Student's t-test. *, $p<0.05$; **, $p<0.01$; ***, $p<0.001$.

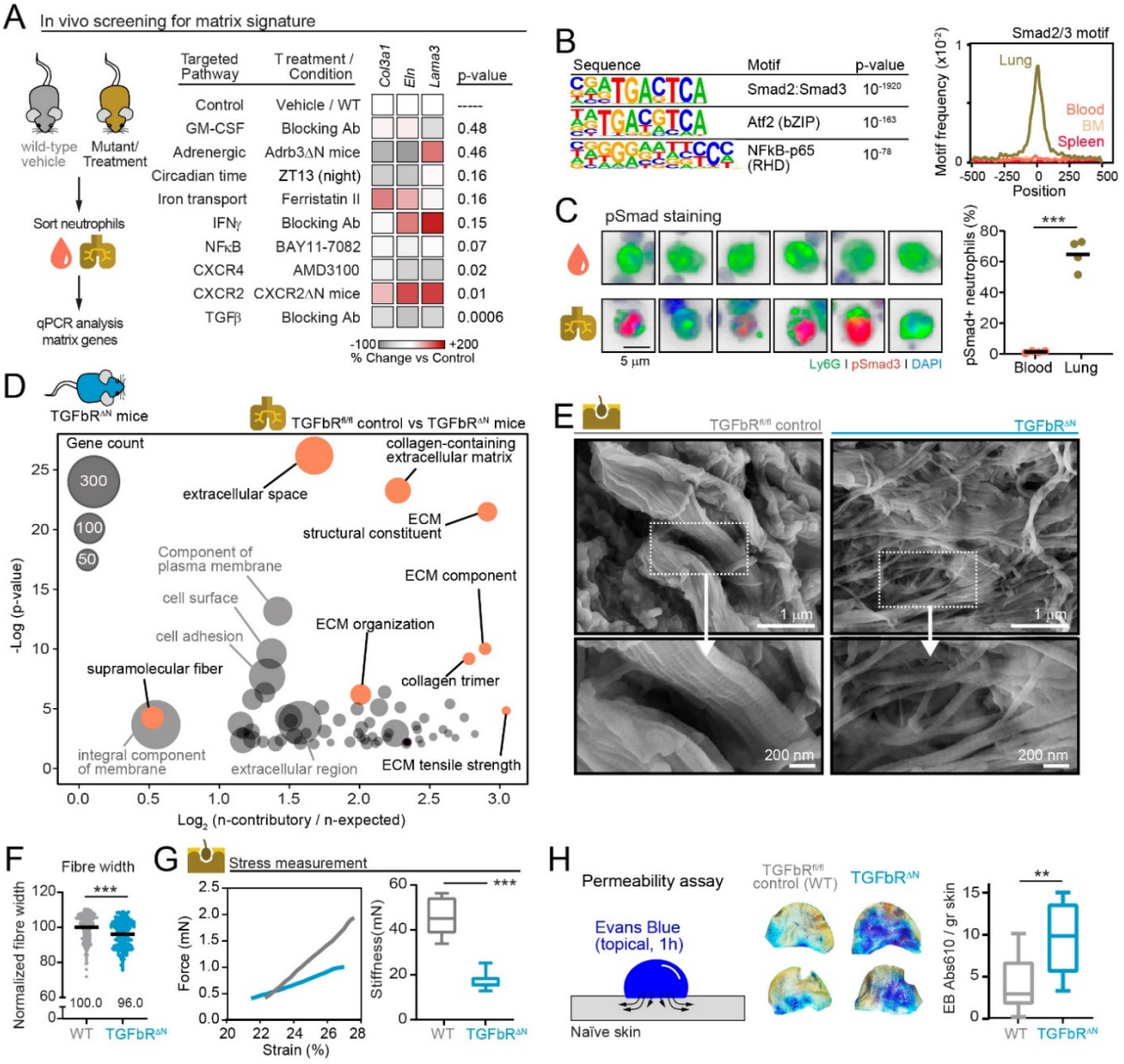

Figure 3. TGFβ signaling drives the matrix program of barrier neutrophils. (A) In vivo screening to identify pathways driving the matrix program using differential expression of signature genes (*Col3a1*, *Eln* and *Lama3*) in blood and lung neutrophils. Mice were treated with vehicle or inhibitors for the indicated pathways, or neutrophil-specific mutant mice compared with control mice. The heatmap represents the mean differential expression in treated lung neutrophils versus controls for each gene and from at least 3 independent mice per group, with p-values calculated by One-sample location t-test shown at right. Calculations for the respective controls are set to zero, and thus shown as a single row for simplicity of representation. (B) Left, enrichment of transcription factor recognition sequences in ATAC-seq peaks in the lung cluster based on HOMER. Right, occurrences of the Smad2/3 motifs among the different tissues. (C) Activation of the Smad3 pathway as determined by detection of the phosphorylated Smad3 protein in neutrophils from lung, but not from blood, which is quantified in the dot plot at right. Data analyzed from 300-2700 cells from 4 mice per group. (D) Bubble plot of Gene Ontology pathways identified from the PCA analysis comparing the transcriptome of lung neutrophils from Cre^{NEG};$TGFbR^{flox}$ control and $TGF\beta R^{\Delta N}$ littermates. Only pathways with adjusted p-values below 0.01 are plotted, with the most relevant ones tagged and those related to ECM in orange. The x-axis represents the log fold enrichment score of the number of contributing genes against the numbers expected by chance for each GO term. For a complete list of pathways see Data S6**.** (E) Representative images of skin from Cre^{NEG};$TGFbR^{flox}$ control and $TGF\beta R^{\Delta N}$ littermates captured by scanning electron microscopy. Images representative of 4 mice per group. (F) Width of collagen fibers in the skin of control Cre^{NEG};$TGFbR^{flox}$ (referred to here as WT) and $TGF\beta R^{\Delta N}$ littermates as measured from SHG in multiphoton imaging by automated software. Data shown is from 15 z-slices per location from 4 different locations per mouse from 4 mice per group. Each dot represents the average value of ~1000 individual analyzed fibers from a single 510 x 510 μm z-slice image. (G) Representative force-strain curves of ear skin from Cre^{NEG};$TGFbR^{flox}$ control and $TGF\beta R^{\Delta N}$ littermates. Left, representative curve of 8-9 mice per group, which are quantified in the box and whiskers plot on the right. (H) Scheme of the permeability assay of Evans blue dispensed topically on the skin surface and allowed to diffuse for 1h. Middle images are representative of treated ears from Cre^{NEG};$TGFbR^{flox}$ control and $TGF\beta R^{\Delta N}$ littermates, and (right) quantification of Evans blue signal captured by the skin; data is from 10-13 mice per group. Data in (C) and (F-H) are compared by unpaired Student's t-test. **, p<0.01; ***, p<0.001.

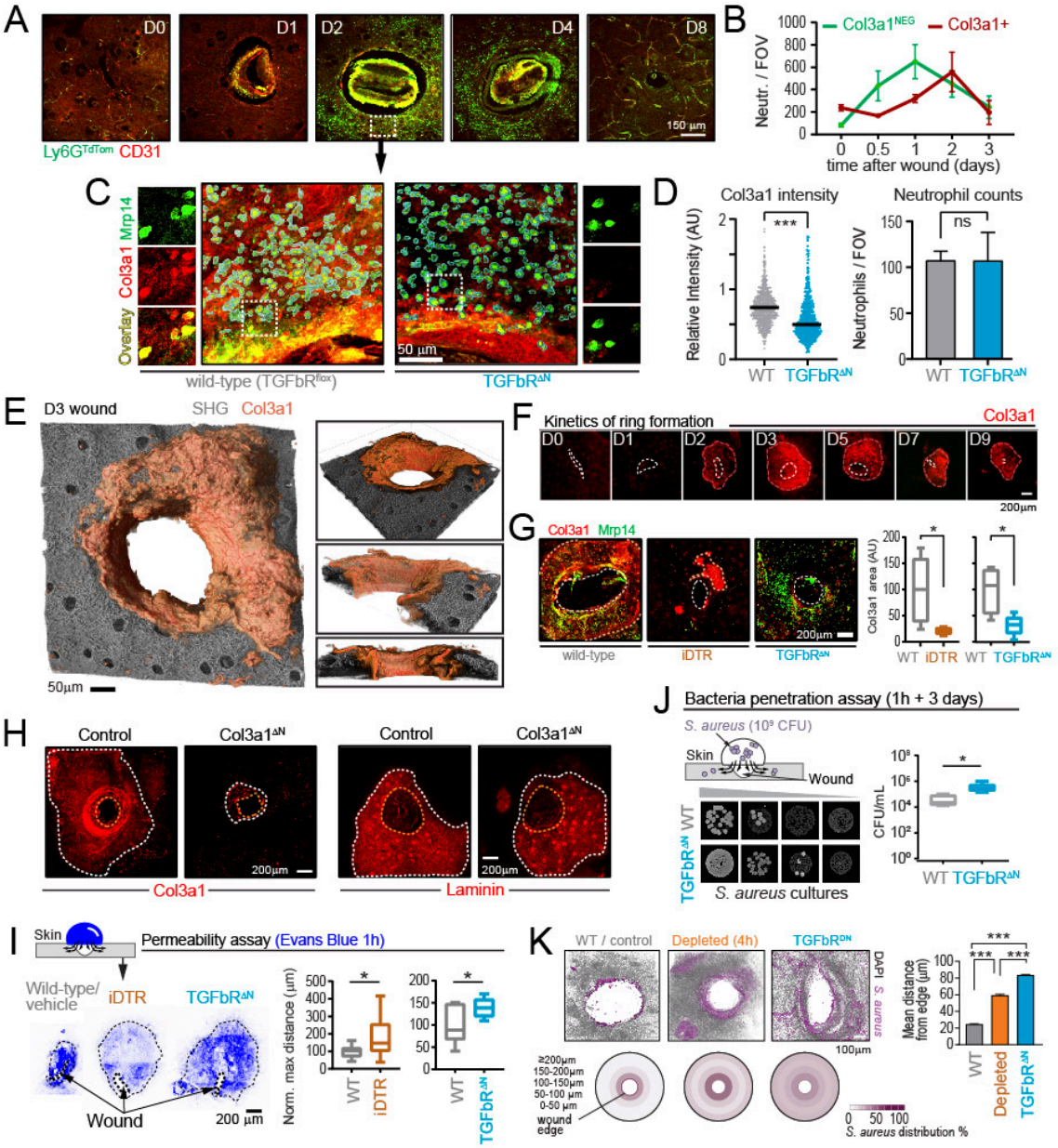

Figure 4. Neutrophils shield skin wounds by building matrix-rich rings. (A) Kinetics of neutrophil recruitment upon skin injury (D0) in Ly6G^{Tomato} mice, showing neutrophils (green) and vessels (red). (B) Quantification of Col3a1^{NEG} and Col3a1+ neutrophils in the wounds; data from 3-4 mice per time point. (C) High resolution multiphoton imaging of neutrophils that accumulate around the wounds at D2 and are strongly immune-reactive for Col3a1 in control TGFbR^{flox} mice, but not in TGFβR^{ΔN} littermates. (D) Quantification of Col3a1 signal and number of neutrophils around wounds in mice from panel (C), with bars indicating median values ± standard deviations; data is from 4-6 mice. (E) 3D reconstruction of a wound from a wild-type mouse, with whole and sectioned side views showing the collagen ring wrapping inner side of the wound. See also Movie S3. (F) Kinetics of Col3a1+ matrix-ring formation around the wound up to D9. Images representative of at least 2 wounds from 1-3 mice per time point. (G) Ring areas in neutropenic (iDTR mice) and TGFβR^{ΔN} mice at day 3, which are quantified in the box and whisker plots at right, compared with their respective controls (Cre-negative floxed littermates). Data from 4 to 6 wounds from at least 3 mice per group. (H) Representative images of Col3 and Laminin deposits in rings (dashed lines) from a Cre-negative floxed control and Col3a1^{ΔN} mice at day 3. The areas covered by each protein are quantified in Fig.S10D; data is from 3-5 mice. (I) Evans blue permeability assay illustrated in the scheme (top), and images showing the diffusion of the dye (dotted lines) from the wound in floxed littermate controls, neutropenic (iDTR) and TGFβR^{ΔN} mice, with quantification box and whiskers plots at right. Data from 10 mice per group. (J) Scheme of the bacteria (*S. aureus*) penetration assay in wounded skin of floxed littermate controls and TGFβR^{ΔN} mice, shown in the scheme (left) and scored as CFU that remain in the full ear skin, 3 days after exposure. Representative CFU (top) and quantification (bottom). Data from 6-7 mice per group. (K) Representative images of wounds showing the spatial distribution of *S. aureus* 4 hours after exposure to the wound. Distribution is shown in the radial plots at the bottom and distances to the wound edge are quantified in the bar graphs at right. Data is from 21 wounds from 3 to 7 mice per group. All data are compared using unpaired Student's t-test (D, G, I, J) or one-way ANOVA followed by Tukey's multiple comparison test (K). *, p<0.05; **, p<0.01; ***, p<0.001.

Supplementary Materials

For *Matrix-producing neutrophils populate and shield the skin*
Vicanolo, Li et al.

Methods

Mice

All experiments were performed on 6–24-wk-old C57BL/6 male and female mice. Chow and water were available ad libitum. Mice with high levels of tdTomato fluorescence in neutrophils ($Ly6G^{tdTom}$) were generated by crossing $Ly6g^{tm2621(cre)Arte}$ ($Ly6G^{CRE}$) mice with $B6.Cg\text{-}Gt(ROSA)26Sor^{tm14(CAG\text{-}tdTomato)Hze/J}$ mice expressing the Cre-inducible tdTomato in the Rosa26 locus, as previously described [36]. Constitutively neutropenic mice ($Mcl1^{\Delta N}$) were generated by crossing $LysM^{Cre}$ with $Mcl1^{tm1Ywh}$ (Mcl1fl/fl) mice [13]. Mice that were inducible for acute neutropenia by diphtheria toxin (DT) injection (iDTR) were generated by crossing $Tg(S100A8\text{-}cre,\text{-}EGFP)^{1Ilw}$ ($MRP8^{CRE}$) with $C57BL/6\text{-}Gt(ROSA)26Sor^{tm1(HBEGF)Awai/J}$ (Rosa26iDTR; characterized in [9]), whereas mice with neutrophil-specific deficiency in *Tgfbr2* signalling ($TGFbR^{\Delta N}$) were generated by crossing $MRP8^{Cre}$ mice with $B6;129\text{-}Tgfbr2^{tm1Karl/J}$ ($Tgfbr2^{fl/fl}$) mice [37], and efficiency of gene deletion assessed by qPCR in lung neutrophils (not shown). Similarly, CXCR2-floxed [38] mice were crossed with $MRP8^{CRE}$ mice. *Col3a1*-floxed mice were generated by Crispr/Cas9 by Cyagen and are characterized in Fig.S10. $Col3al1^{\Delta N}$ mice were generated by crossing the floxed mice with the $MRP8^{CRE}$ driver. $Adbr3^{fl/fl}$ mice were generated by PolyGene (PolyGene AG, Switzerland) using the 'knockout-first' design. Briefly, a transgenic cassette (EUCOMM vector ETPG00281_W_3_E05) was injected into C57Bl/6-derived embryonic stem cells to introduce flanking loxP-sites in exon 2 of the Adrb3 gene, which were then injected into blastocysts of C57Bl/6N mice, and chimeric males were mated to heterozygous Flp-deleter mice to generate the final $Adbr3^{fl/fl}$ allele. These mice were then bred with the $MRP8^{CRE}$ to target expression of Adbr3 in neutrophils. Efficiency of gene deletion in sorted neutrophils was confirmed by qPCR (not shown) or previously characterized [19]. Albino $Lyz2^{GFP}$ reporter mice for intravital imaging were generated by crossing $B6(Cg)\text{-}Tyr^{c\text{-}2J}/J$ mice with $Lyz2^{tm1.1Graf}$ mice [39]. For circadian stretching assays, mice were treated with 3 µg/g bodyweight of either anti-Ly6G (1A8 clone from BioXcell; neutrophil depleted) or control IgG (non-depleted) antibodies for two consecutive days, in normal light-controlled mouse facility. On the third day, mice were sacrificed at ZT9 and ZT17 (4pm and 12am in our facility). Blood and ear skin samples were collected for FACS analysis and stretching measurements. For lungs, we used bulk preparations containing neutrophils from all compartments of this organ (alveolar, interstitial, and intravascular), as we found a similar distribution of Col3+ neutrophils across all these regions. The control mice used in each experiment are indicated in the respective figure legends. Characterization of the iDTR neutropenic mice showed significant increases in monocytes and macrophages in the naïve skin but not in the wounded skin. In contrast, $TGFbR^{\Delta N}$ mice show no alterations in any myeloid population in the naïve or wounded skin.

$Rosa26^{LSL;\ CNA35\text{-}mCherry}$ reporter mice were generated at Cyagen using CRISPR/Cas9-mediated genome engineering. Briefly CAG promoter-loxP-PGK-Neo-6*SV40pA-loxP-Kozak-mCherry-CNA35-rBG pA cassette was cloned into intron 1 of mouse ROSA26 gene. For colony genotyping, we used the following primer sequences: 5′-GAGCATGGTAAGGAAGAAGTGAACG (Wt, forward), 5′-CTTATTAGCCAGAAGTCAGATGC (Wt, reverse), 5′-CACTTGCTCTCCCAAAGTCGCTC (Tg, forward), and 5′-ATACTCCGAGGCGGATCACAA (Tg, reverse). The floxed mice were then crossed to $Ly6G^{CRE}$ or $Dpt^{CreERT2}$ (courtesy of Shannon Turley) driver mice to induce expression of the CNA35-mCherry reporter mice for neutrophils and fibroblasts, respectively. CNA35-mcherry expression in neutrophils and fibroblasts was confirmed by flow cytometry. To induce recombination, $Dpt^{CreERT2}$; $Rosa26^{CNA35\text{-}mCherry}$ mice were given 4mg tamoxifen daily i.p injections for 5 consecutive days and rested for two weeks. Mice were housed in specific pathogen–free facilities at Fundación CNIC, Yale or SIgN and maintained on a 12-h light/12-h darkness schedule. All protocols were approved by the corresponding regional authorities in Spain, Yale University and Singapore.

Genotyping of the Col3a1^{flox} mice (see Fig.S12A) was performed using the primers 1 Forward: 5'-TGGAAGAGGTTTATACTGCCAAGA -3', primer 2 Reverse: 5'- AGCTGGAAATGAACAGTTTTACCCA -3'. To check for excision we used primer 3Forward: 5'- ATATAAACAGAGTTGCCCGTGCTT -3' and primer 4 Reverse: 5'- TCGTGTAAACCCATACAGCAGAAC -3'. Cycles were 95°C 1min, 95°C 15s, 56°C for 15s, 72°C 30s for 35 cycles, and 72ºC for 5 min.

Needle puncture wound model

Mice were anesthetized by isoflurane, and ears were held gently in place with forceps and then pierced with a 30G needle from the ventral side below through the full thickness of the tissue. The pierced site is chosen approximately 3 to 6 mm from the tip of the mouse ear. For in vivo multiphoton microscopy, hair-removed ear skin from LysM-EGFP mice were wounded and followed over time by imaging with a multiphoton microscope (LaVision BioTec TriMScope) at 950 nm with a dichroic filter at 500 nm and bandpass filters of 475/42 (SHG) and 525/50 (EGFP).

Timestamp of neutrophils migrating to the skin

An intraperitoneal injection of tamoxifen (4mg/mice) was performed to induce CreERT2 recombinase activity in 8–12-week-old male or female iLy6GtdTom mice [9], immediately after wounding of the skin (day 0). Mice were sacrificed 1, 2, or 3 days after wounding and tamoxifen induction. A group of day 0 mice sacrificed 10 minutes after wounding and tamoxifen induction were used as controls of tomato expression. Maximum pulse labelling efficiency was reached either 2 or 3 days after tamoxifen administration in the bone marrow, blood and the skin, and affected 1%–20% of the overall neutrophil population depending on the analyzed time point.

Human tissues

Source and analysis of human neutrophils from blood, spleen, lung and skin

Human skin samples were collected in Fudan University Shanghai Cancer Center in Shanghai, China, under the Shanghai Cancer Center Institutional Review Board (SCCIRB) protocol 050432-4-2108*. Skin samples were non-cancerous, perilesional discarded skin that was excised to access the papillary thyroid carcinoma of the patients. Human blood, lung and spleen samples were collected in Renji Hospital in Shanghai, China, under the Renji Hospital Ethics Committee protocol KY2021-063-B. Both protocols are in accordance with the Declaration of Helsinki. Blood samples were collected from healthy donors. Lung and spleen samples were collected from perfused organ donors. Skin biopsies were cut into small pieces and enzymatically digested with the whole skin dissociation kit (130-101-540, Miltenyi Biotec) according to the manufacturer's instruction. Blood was collected in BD vacutainer K2E (EDTA) tubes (BD Healthcare, 367525) to prevent from coagulation, and lysed in 1× RBC lysis buffer (diluted from 10× BD Pharm Lyse™, 555899) for 5 minutes twice to deplete erythrocytes. Lung and spleen were cut into small pieces before digested in collagenase IV (385U/mL, Sigma) and DNase I (2.5mg/mL, Sigma) mix for 30 minutes at 37ºC, and the samples were homogenized into single-cell suspension using syringe plungers and 70μm cell strainers. Single-cell suspensions were blocked with Fc-blocker (Biolegend), and stained with Fixable Viability staining 700 (564997, BD Biosciences) (1:1000), CD45 APC-CY7(304014, Biolegend) (1:200), CD3 PE-CY7 (300316, Biolegend) (1:200), CD19 PE-CY7 (302216, Biolegend) (1:200), CD56 PE-CY7(362510, Biolegend) (1:200). Samples were subsequently washed with FACS buffer and sorted with a FACS Aria III cell sorter (BD Biosciences). We sorted Live CD45+CD3-CD19-CD56- cells and performed cytospin. Cells were fixed on slides with 100 µl of 2% PFA for 30 minutes, then permeabilized with 0.3% Triton in PBS for 35 minutes, followed by blocking with PBS containing 5% BSA and 5% FBS for 30 minutes. Cells were then incubated with 1:200 primary antibodies (anti-Col3a1 #ab7778 and IgG isotype #ab37415 from Abcam, Alexa Fluor 594 anti-human CD66b #562940 from BD Biosciences) in PBS for 1 hour and washed with excess PBS. Secondary antibody mix (1:500 goat anti-rabbit IgG Alexa fluor 647 (A-21245, Life Technologies), and 1:2000 DAPI in PBS were then applied for another 30 minutes, before washing with excess PBS. Slides were mounted with Mowiol (4-88, Sigma) until ready for imaging with a fluorescence

microscope (Dragonfly 200) with a 20× objective. Imaris software (version 9.5, Bitplane) was used to surface individual CD66b+ neutrophils and determine percentages of ECM+ neutrophils detected in the images.

The immunofluorescence analyses of the Shanghai samples were validated at the Yale site by flow cytometry (blood and skin) and whole mount staining (skin) of non-cancerous, perilesional discarded skin that was excised for the repair of primary defects resulting from Mohs-confirmed surgical excisions of keratinocyte cancers, while the blood samples were collected from healthy donors, provided by the Department of Dermatology. These samples were collected under Yale Institutional Review Board (IRB) protocol #2000027571 in accordance with the Declaration of Helsinki. Blood was collected in heparin vacutainer tubes (BD Healthcare) and leukocytes were isolated using HetaSep (Stemcell) solution, according to the manufacturer's instructions. Skin biopsies were cut into small pieces and were enzymatically digested with Liberase TM (Roche) and DNAse1 (Sigma) in RPMI for 40 minutes at 37ºC. Skin was then homogenized into single-cell suspension using syringe plungers and 70µm cell strainers. Surface staining was carried out at 4ºC for 20 minutes with an antibody mixture of CD45, CD66b, and CD16, as well as the Zombie UV viability stain. Samples were subsequently washed with FACS buffer, fixed and permeabilized with BD Cytofix/Cytoperm™ Fixation/Permeabilization Kit, according to manufacturer's instructions. Intracellular staining of col3a1 was performed in 1X Perm/Wash buffer. Samples were incubated with either the primary anti-col3a1 antibody or 1X Perm/Wash buffer alone, the latter in the case of fluorescence minus one (FMO) control samples for 20 minutes, washed twice with 1X Perm/Wash buffer, and then incubated for 20 minutes with the secondary anti-rabbit Alexa Fluor488 antibody. After a final wash with 1X Perm/Wash buffer, samples were resuspended in FACS buffer and acquired on BD Symphony.

For immunofluorescence of human skin, the subcutaneous fat was removed, the skin was cut into 1-5mm thick pieces containing epidermis and dermis, then fixed with 2% PFA overnight at 4ºC. Samples were then cleared with incubation with CUBIC-L (T3740, TCI Chemicals) for 5 to 7 days at 37ºC with agitation, then briefly washed with 0.05% PBST and incubated with primary antibodies against MRP14 (ab105472, Abcam) and Col3a1 (ab7778, Abcam) (1:200) in 0.05% PBST at room temperature for 2 days with agitation. Samples were then washed with 0.05% PBST for another day. Fluorescence staining was performed with secondary antibodies (1:500, goat anti-rat Alexa Fluor488 (A11006, Invitrogen) and goat anti-rabbit Alexa Fluor 647 (ab150079, Abcam) and in 0.05% PBST for two days with agitation. Samples were then washed by incubating in 0.05% PBST for another day, before overnight refractive index matching using CUBIC-R (T3983, TCI Chemicals) with DAPI (1:1000). Imaging was performed using an SP8-STED confocal microscope (Leica) with 40X objective at a resolution of either 512 x 512 or 1048 x 1048 pixels in 16-bit in z-stacks covering a tissue depth of 50-100µm with a z-step size of 1µm. Fiji software was used to identify MRP14+ neutrophils and to determine the Col3a1 signal inside and outside neutrophils.

Transcriptomics

RNA sequencing (RNA-seq) of sorted tissue neutrophils from parabiont mice

Parabiosis was described in detail in [7], and source data was previously uploaded and described in [9] (GSE141745). Briefly, CD45.1 (B6.SJL-Ptprca Pepcb/BoyJ) mice were paired with CD45.2 mice in parabiosis for 4 weeks and partner CD45.2 neutrophils were isolated from various CD45.1 mice tissues (blood, BM, spleen, lung, skin and gut) and submitted for bulk RNA sequencing. Genes of interest were initially identified based on GO terms for: collagen-containing extracellular matrix (GO:0062023), extracellular matrix structural constituent (GO:0005201), collagen fibril organization (GO:0030199) and collagen metabolic process (GO:0032963). These gene lists were further curated manually to logically grouped into 'Collagens' (genes that contain the term 'collagen' as part of their official main name), 'Major ECM' (elastin, fibronectin and laminins), 'Other ECM' (from GO:0005201 but removing the duplicated entries), 'Fibril-forming' (from GO:0030199 and removing the duplicated entries) and 'Matrix metallopeptidase-related' (from GO:0032963 and further refined with known 'Matrix metalloproteinase' ('Mmp'), 'A Disintegrin and Metalloproteinase with Thrombospondin motifs' ('Adamts') and 'Tissue inhibitors of metalloproteinases' ('Timp') genes), generating a combined list of up to 158 genes of interest.

Aggregate averages and standard deviations were calculated from the non-barrier tissues (Blood, BM, Spleen) on a per gene basis, then heatmaps were generated by renormalizing the TPM count data based on the calculated Z-scores, derived from subtracting the individual values from the calculated averages and dividing by the calculated standard deviations. Further analysis was performed on these data by calculating for each barrier tissue the TPM count values against the aggregate averages and standard deviations of the non-barrier tissues, for negative log p-values and log2 fold changes.

Single cell RNA sequencing analyses

All downstream analyses were implemented using R v4.0.3 and the package Seurat v4.0.5. Raw counts from each sample were merged and normalized using the Seurat standard normalization, scaling and clustering with the shared nearest neighbor (SNN) algorithm. Cells were annotated using SingleR. The scaling and PCA were performed using all features, while the UMAP was constructed using the significant PCs, scored by the ScoreJackStraw function.

For the *in silico* analysis of existing datasets, we downloaded the Tabula Muris dataset to test the expression of different cell signatures. We used SingleR with the Immgen database to annotate cells tagged as "myeloid cell", "granulocyte", "granulocytopoietic cell", "common lymphoid progenitor", "hematopoietic precursor cell" or "leukocyte". To generate the scores for the neutrophils analyzed by bulk RNAseq, we used the top 500 most expressed genes in each tissue of our bulk sequencing. We then assigned a score based on those genes to each cell in the Tabula Muris dataset, using Seurat function AddModuleScore. For the barrier and sterile signatures, we merged the previously obtained genes from the different tissues into two categories: sterile (BM, Spleen and blood) and barrier (Lung, Gut and Skin) and a new score was assigned to each Tabula Muris cell, again calling Seurat function AddModuleScore.

Circadian RNA-seq of total bulk tissue

Mice were treated with 3 µg/g mouse bodyweight of either anti-Ly6G (neutrophil depleted) or control IgG (nondepleted) antibodies for two consecutive days, in normal light-controlled mouse facility or 12 h inverted light cabinets. In the morning of the third day, mice were bled before lung harvest to obtain blood samples for confirmation of neutrophil depletion using a standard hemocytometer (ABX Pentra 80; Horiba), as well as flow cytometry. Lung samples were collected every four hours (ZT1-5-9-13-17-21) from 3 mice per group. In the $Mrp8^{CRE}$; iDTR model, mice were injected intraperitoneally with 10 µg/kg of diphtheria toxin (DT; Calbiochem) for two consecutive days, and tissues were collected on the third day. Ear skins, colon and marrow samples were harvested after perfusion of mice with saline at ZT1-3-4-5-7-9-10-12-13-15-16-18-19-21-22-24 from one mouse per time point and snap-frozen in 1 ml of TRIzol each. Whole RNA was obtained subsequently using mechanical disruption (Polytron PT 6100; Kinematica) and chloroform extraction and cleaned up using silica-based spin columns (Qiagen) according to manufacturer instructions. RNA quality was checked using capillary electrophoresis (Agilent). Samples were submitted for whole RNA next generation sequencing in the Genomics Unit of CNIC. 200 ng of total RNA was used to generate barcoded RNA sequencing libraries using the NEBNext Ultra RNA Library preparation kit (New England Biolabs). Libraries were sequenced with HiSeq2500 (Illumina) to generate 50-nucleotide single reads, with a minimum of eight million reads per sample. FastQ files for each sample were obtained using CASAVA v1.8 software (Illumina). Reads were further processed with RTA v1.18.66.3. FastQ files for each sample were obtained using bcl2fastq v2.20.0.422 software (Illumina). For data analysis, sequencing adaptor contaminations were removed from reads using Cutadapt v1.7.1, and the resulting reads were mapped on the transcriptome (GRCm38 Ensembl gene-build 84) and quantified using RSEM v1.2.20 and Kallisto v0.43.1.

To examine specific genes for circadian perturbations, raw normalized counts (RPKM) of the various genes were further transformed by custom Python scripts. Raw reads were smoothed by averaging across 3 (lung) or 5 (skin, gut, bone marrow) nearest time points for control or neutropenic tissues, then normalized to the higher average of either the control or neutropenic tissues. To focus on showing only the variations in gene

expression amplitudes, we then subtracted each curve by their own respective values using ZT where control curve was at minimum as baseline to plot against the central zeitgeber timing (ZT) for each gene of interest and each tissue. Estimates of value distribution were generated by calculating the pooled variance for each central ZT time point per sample (this includes all the neighbouring time point values that were used for calculating the smoothed averages), then taking the square root of the pooled variance. Neutropenic and control line charts were plotted on the same subplot per gene per tissue in order to clearly identify perturbations to the normal circadian patterns from the loss of neutrophils. To generate a representative summary of the extent of circadian perturbations for the tissues, the smoothed neutropenic gene averages were first subtracted from the control averages for each individual gene to generate the delta curves. For each individual gene, the delta curves from the various tissues were then combined and normalized to the largest absolute value among the datasets. Thus, the maximum or minimum value out of all the tissues will be set as 100% or -100% respectively, and the rest of the delta curves would be proportionally normalized based on differences in their RPMK values. These normalized delta curves were then plotted separately for each tissue for all the genes of interest. Further, to objectively quantify whether gene levels were following circadian rhythms we used CircaN v2.0. [12]. We used R2 > 0.7 and BH combined q-value < 0.05 to determine whether the genes showed circadianicity.

RNA-sequencing of TGFbR$^{\Delta N}$ lung neutrophils

This experiment was performed at the SIgN Genomics unit (Singapore). Total RNA was extracted using Arcturus PicoPure RNA Isolation kit (Thermo Fisher Scientific) according to manufacturer's protocol. All tissue RNAs were analyzed on Agilent Bioanalyser for quality assessment with RNA Integrity Number (RIN) ranging from 6.8 to 8.2 with median of 7.8. cDNA libraries were prepared using 2 ng of total RNA and 1 µl of a 1:50,000 dilution of ERCC RNA Spike in Controls (Thermo Fisher Scientific) using the SMARTSeq v2 protocol [PMID: 24056875] with the following modifications: 1. Addition of 20 µM TSO; 2. Use of 200 pg cDNA with 1/5 reaction of Illumina Nextera XT kit. The length distribution of the cDNA libraries was monitored using a DNA High Sensitivity Reagent Kit on the Perkin Elmer Labchip. All samples were subjected to an indexed paired-end sequencing run of 2x151 cycles on an Illumina HiSeq 4000 system (~20 million read-pairs per sample).

STAR aligner was used for mapping paired-end raw reads to mouse genome build GRCm38. Reads that were mapped to genes were counted using featureCounts based on GENCODE vM22 gene annotation. edgeR Bioconductor package was used to calculate log2 transformed counts per million mapped read (log2CPM) and log2 transformed reads per kilobase per million mapped reads (log2RPKM). Genes with log2CPM inter-quartile range (IQR) across all samples less than 0.5 were filtered out and Principal Component Analysis (PCA) was performed on log2RPKM values using R function 'prcomp'. Enrichment analysis for gene ontology with top 10% of the primary principal component loadings was performed using TopGo (R package version 2.36.0.). In the standard Gene Ontology analysis, for each specific GO term a corrected p value is calculated based on how many genes in the supplied list appear when compared to the number of genes that is expected to randomly appear by chance. To identify GO terms of interest, we plotted the negative log p-value from this analysis (y-axis) against log2 fold enrichment of the number of genes present in the top 10% of the primary principal component loadings divided by the expected numbers by chance (x-axis).

Nanostring of sorted neutrophils

Blood and lung neutrophils were isolated from Cre+ TGFbR2$^{fl/fl}$ mice or Cre-negative littermates by flow cytometry-assisted cell sorting, yielding cells of approximately 70 - 350 x 10^3 neutrophils per mouse and sample. Cells were then pelleted by centrifugation at 800 x g for 10 minutes, then supernatant was aspirated leaving behind approximately 20 µl of liquid. Cells were then lysed by addition of 350 µl of RLT-PLUS lysis buffer (Qiagen), then RNA was extracted using silica-membrane based columns (RNeasy PLUS micro kit, Qiagen) according to manufacturer instructions. Purified RNA was used directly in our custom Nanostring assay panel (nCounter Elements 48 gene) according to manufacturer instructions (NanoString

Technologies, Seattle, WA). For the analysis, a custom nCounter assay for quantitative assessment of expression of 48 gene element was designed and described previously [9]. Raw data was analyzed by nSolver software (NanoString Technologies, Seattle, WA, USA) and were normalized by positive controls and starting cell counts, then log-2 fold changes were calculated against each matched sample average per mouse.

ATAC Sequencing (ATAC-seq) and chromatin motif analysis

Source data was previously uploaded and described in [9]. Briefly, blood, lung, spleen and bone marrow neutrophils from WT male mice were sorted and processed for ATAC-seq as previously described [40]. Samples were size selected using AMPure XP beads (Beckman-Coulter) to yield libraries ranging from 100 bp – 1000 bp, and quality checked for nucleosomal phasing and size distribution using DNA hi-sensitivity Bioanalyzer assay (Agilent). Quantification was performed with KAPA Library Quantification Kit (Illumina) and samples were pooled at an equimolar ratio and sequenced on a HiSeq2500 using 75 bp paired-end chemistry in Welcome Centre for Human Genetics, Oxford. Raw sequencing reads were trimmed with Cutadapt prior to mapping to the mm10 version of the mouse genome using Bowtie2 with the following parameters–local–X 2000. PCR duplicates were removed with PicardTools, additionally, reads mapping to chrM, with MAPQ < 10, and insert sizes > 150 bp were removed prior to peakcalling. Peaks were called with MACS2 with the following settings: –format BAMPE–nomodel–keep-dup all–mfold 5 50. Peaks found in at least 2 biological replicates were kept for further analysis and merged peakset consisting on all discovered peaks was used for differential accessibility testing. Reads were counted over the merged peakset using BedTools and tested using DESeq2. Significantly differentially accessible peaks were deemed as having adjusted p values < 0.05 (LRT test), and adjusted p values < 0.05, and fold change > 1.5 (Wald test). For this paper, for a combined comparison between the lung against the other 3 non-barrier tissues of blood, bone marrow and spleen, the statistically significantly different peaks that were higher (i.e. representing more open chromatin regions) in lungs when compared against the other 3 tissues individually were combined together, and the rest of the peaks that were higher in the other tissues versus lung were used combined and used as the background peaks. Peaks were further filtered for only those within 30000 bp from the transcription start site. De novo motif discovery was performed using Homer findMotifs.pl on the peaks in each cluster using default settings. Motif scanning was conducted using Homer annotatePeaks.pl on 1 kb windows centered over ATAC peaks with a bin size of 10 bp using the top identified motif discovered from findMotifs.pl.

In vivo screening based on qPCR of sorted neutrophils

At least 3 mice from each control/wild-type or treatment/mutant groups were used for each experiment performed on the same day. Doses of reagents used, or mutant mice used were: GM-CSF (anti-GM-CSF (MAB415, R&D systems) at 100 μg/day for 3 consecutive days vs isotype IgG); Adrenergic ($MRP8^{Cre}$; Adbr3fl/fl vs matched WT mice) ; Circadian time (ZT5 vs light cabinet matched ZT17); Iron transport (Ferristatin II (Chlorazol black, Sigma) at 20 mg/kg/day in water for one day vs PBS); IFN-gamma(anti-IFN-gamma (R4-6A2, BioXCell) at 100 μg/day for 3 consecutive days vs isotype IgG); NF-kappa-B (BAY11-7082 (Sigma) at 5 mg/kg/day for 3 consecutive days vs vehicle (5% DMSO in saline); CXCR4 ($MRP8^{Cre}$;$CXCR4^{fl/fl}$ vs Cre-negative littermates); CXCR2 ($Lyz2^{Cre}$;$CXCR2^{fl/fl}$ vs Cre-negative littermates); TGFβ1 (anti-TGFβ (MAB240, R&D systems) at 100 μg/day for 3 consecutive days versus isotype IgG). All reagents were diluted in PBS (unless otherwise stated) and delivered by subcutaneous injections using 30G insulin syringes.

Blood and lung neutrophils were isolated from wild-type/control or treated/mutant mice by flow cytometry-assisted cell sorting. Approximately 10^5 blood and 2-3 x 10^5 lung neutrophils were collected from each mouse after the cell sorting. Cells were then pelleted by centrifugation at 800 x g for 10 minutes, then supernatant was aspirated leaving behind approximately 20 μl of liquid. Cells were then lysed by addition of 350 μl of RLT-PLUS lysis buffer (Qiagen), then RNA was extracted using silica-membrane based columns (RNeasy PLUS micro kit, Qiagen) according to manufacturer instructions. Quantitative mRNA to cDNA

conversion was performed using the commercial high-capacity cDNA reverse transcription kit (4368814, Applied Biosystems) according to manufacturer instructions. qRT-PCR was performed on the extracted RNA using a standard real-time PCR instrument (Applied Biosystems 7500) using SYBR green master mixes (Applied Biosystems) according to manufacturer instructions. Primers were used at 0.4 μM final concentration with 2 μl of cDNA in 10 μl total volume wells. Primers used were: *Lama3* (primer bank ID 2098725a1, 5'- CTGTGACTACTGCAATTCTGAGG-3', 5'- CAAGGTGAGGTTGACTTGATTGT-3'); *Col3a1* (Primer bank ID 33859526a1, 5'-ACGTAGATGAATTGGGATGCAG-3', 5'-GGGTTGGGGCAGTCTAGTG-3'); *Eln* (primer bank ID 31542606a1, 5'-TTGCTGATCCTCTTGCTCAAC-3', 5'-GCCCCTGGATAATAGACTCCAC-3'); *Paf1* (Primer bank ID 31980912a1, 5'-TGGAGTAGTCTGCCGAGTCAA-3', 5'-CAAGGAGGTTGCTTTGTACTGA-3'); *Rplp0* (5'-ACTGGTCTAGGACCCGAGAAG-3', 5'-TCCCACCTTGTCTCCAGTCT-3').

To estimate the impact of treatments/mutations on the overall ECM signature, Ct values from the lung and blood samples for each experiment were first translated to relative linear abundance ratios (L) by the delta-delta Ct method using the average Ct of Paf1 and Rplp0 genes as housekeeping reference, followed by normalization of these values by setting the lung control average ($\bar{L}_{control}$) as 100% for each of the 3 genes (Col3a1, Eln, Lama3). Ct values from the blood were also processed as a reference, but the relative abundance levels of these gene transcripts in blood samples were consistently negligible (less than 0.1%) when compared to matching lung samples, and were thus ignored for subsequent calculations. The mean differential lung gene expression attributed to the treatment/mutation ($\Delta\bar{L}$) was calculated as $\Delta\bar{L} = \bar{L}_{treated} - \bar{L}_{control}$. These values were plotted as a heatmap in the figure for each treatment and gene. To obtain a simple score of whether the changes were likely to be attributable to the treatment/mutation, a consistency p-value was calculated by performing a one-sample location t-test versus the null hypothesis that the average $\Delta\bar{L}$ for all 3 genes was zero. This parameter thus measures how consistently the gene changes among all 3 genes were moving in the same direction away from zero.

Protein analysis

Quantitative proteomics by mass spectrometry of the skin (in neutropenia)

To assess how neutropenia affected tissue composition, total skin was harvested at ZT7 from control wild-type (Cre-negative DTR-floxed littermates), Mcl1$^{\Delta N}$ or iDTR mice, with 3 biological replicates per condition, and samples were distributed in three independent Tandem Mass Tag (TMT) 10-plex experiments, one experiment per tissue. In each TMT experiment one of the channels was reserved for a common internal standard (I.S.) made by pooling the 24 peptide samples. DT injections were performed 1 and 3 days for all 3 groups of mice before harvest. For skin tissues, hair was removed with Veet cream immediately after harvest and ears were split into dorsal and ventral portions with its cartilage mechanically removed by forceps before further processing. To study the effects of neutrophil depletion and TGFβ receptor signalling on the wound proteome, WT, iDTR or TGFbR$^{\Delta N}$ mice were subjected to ear injury. A limited area around the wound was dissected (6-10 mg tissue) and subjected to ECM extraction and TMT proteomics analysis. From each animal, an equivalent amount of skin from the other (healthy) ear was also excised and used as an internal control. 4 biological replicates per condition (WT, iDTR and TGFbR$^{\Delta N}$) with 2 samples per animal (injured and healthy control) were distributed in three independent TMT 10-plex experiments. Samples from the same animal were kept together in the same TMT experiment.

ECM proteins were extracted from each sample using the CNMCS Kit following manufacturer's instructions. Briefly, protein extracts were obtained by tissue homogenization with ceramic beads (MagNa Lyser Green Beads, Roche, Germany) in CS buffer (Pipes pH6.8, MgCl2, NaCl, EDTA, sucrose, SDS, sodium orthovanadate; Biochain Institute, Inc. #K3013010-5) freshly supplemented with protease and phosphatase inhibitors. After 20 min incubation at room temperature, extracts were centrifuged at 18,000 g, 4°C for 20 min and the pellet was resuspended in 200 µl ice cold buffer C (HEPES pH7.9, $MgCl_2$, KCl, EDTA, Sucrose, Glycerol, Sodium orthovanadate) freshly supplemented with protease and phosphatase inhibitors. After a 20 min incubation at 4°C, extracts were spun at 18,000 g, 4°C for 20 min. The pellet was taken up in 50 µl

buffer X (Tris H-CL 100 mM pH8.8, EDTA 1 mM, SDS 6%, DTT 0.1M), boiled for 5 min and spun at 8,000 g at RT for 5 min. The supernatant, enriched in ECM proteins, was subjected to deglycosylation using PNGase F (New England) following manufacturer's instructions. The resulting proteins were subjected to filter-aided digestion (Nanosep Centrifugal Devices with Omega Membrane-10K, PALL) [41]. Briefly, urea was added to each sample to bring SDS concentration down to 0.06%. Samples were then transferred to the filter and centrifuged at 14,000 × g for 10 min. Cys residues were blocked with 50 mM iodoacetamide for 1 h at room temperature in the dark. After three washes with 100 µl 50 mM ammonium bicarbonate pH 8.8, proteins were digested with trypsin (1:40 trypsin:protein, Promega) overnight at 37 °C. After protein digestion, peptides were eluted from the filter in two steps, first with 40 µl 0.5M ammonium bicarbonate and then with 50 µl 0.5M NaCl. Peptides were acidified with trifluoroacetic acid to a final concentration of 1%, desalted on C18 Oasis HLB cartridges (Waters, Milford, MA, USA), and vacuum-dried. Peptides were TMT-labeled following manufacturer's instructions and analysed by nanoLC-MS/MS as described above, except that a 120 min acetonitrile gradient was used. Protein identification was performed as described above, except that Methionine, Lysine and Proline oxidation (+15.994915 Da) and Asparagine and Glutamine deamidation (+0.984016 Da) were set as variable modifications. Cysteine carbamidomethylation (+57.021464 Da) and TMT labeling (+229.162932 Da) at peptide N-terminal end and Lys were considered as fixed modifications. Peptides were identified from MS/MS data at 1% FDR as described above [42,43]. For semi-quantitative estimates of changes in post translational modifications (PTM) by amino acid positions in neutropenic tissues, we modified the proportion (rate) of each modified site using the following formula: $Rate_{PTM} = \frac{I_{PTM}}{I_{PTM}+I_{unmodified}} \times 100\%$ where I_{PTM} is the sum of reporter intensities of identified peptide species containing the modified site and $I_{unmodified}$ is the sum of reporter intensities of all peptide species containing the non-modified site. Sample PTM percentage rates from control mice were then subtracted from those of the neutropenic samples to yield the differential PTM rates for each amino acid position.

For protein quantitation, the quantitative information from TMT reporter intensities was integrated from the spectrum level to the peptide level, and then to the protein level based on the WSPP model [42] using the GIA integration algorithm. Briefly, for each sample i, the values $x_{qps} = log_2 {}^{A_i}/_{C}$ = were calculated, where A_i is the intensity of the TMT reporter of the corresponding sample i in the MS/MS spectrum s coming from peptide p and protein q, and C is the mean intensity of the TMT reporters from all the samples of the experiment (Effect of neutropenia experiment) or the intensity of the TMT reporter from the internal standard (Wound skin experiment). The log2-ratio of each peptide (x_{qp}) was calculated as the weighted mean of its spectra, the protein values (x_q) were the weighted mean of its peptides, and the grand mean ($\bar{x}$) was calculated as the weighted mean of all the protein value [42]. The statistical weights of spectra, peptides, and proteins (w_{qps}, w_{qp} and w_q, respectively) and the variances at each one of the three levels (σ_S^2, σ_P^2, and σ_Q^2, respectively), were calculated as described. Protein abundance changes were expressed in standardized units z_q [42]. For clarity, in the figures the z_q scores were renormalized on a per protein basis by subtracting the average of the control samples, and only the most abundant proteins presented to avoid biased conclusions for the poorly represented proteins, whose enrichment is sensitive to loss of the most represented proteins. To compare PTM rates of lysine hydroxylation of Col3a1 protein, z_q scores per peptide sequence (with at least 3 detected peptide-spectrum matches (PSM)) were compiled and plotted as cumulative distribution functions for two-tailed two sample Kolmogorov–Smirnov (KS) tests, checking neutropenic curves against the control curve individually.

Immunofluorescence

Intracellular immunofluorescence of tissue neutrophils

Mice were euthanized and 500 µl of blood was harvested by cardiac puncture with a 25G needle and 1 ml syringe and immediately mixed with 14 ml of ice-cold PBS to prevent clotting. Mice were then perfused with 20 ml of PBS, and lungs were harvested. For blood, cells were centrifuged at 800g for 7 minutes at 4C, then supernatant was removed and erythrocytes were lysed with 7 ml of 1X ACK buffer (0.15 M ammonium chloride, 0.01 M potassium bicarbonate, 0.1 mM EDTA) on ice for 10 minutes. Lysis was stopped by the

addition of another 7 ml of ice-cold PBS, then centrifuged again at 800 x g for 5 minutes at 4C to obtain since cell suspension. Lungs were harvested and cut dry into small pieces before being digested in liberase TM (Roche) and DNase1 (Sigma) for 30 min at 37°C. Lungs were then homogenized into single-cell suspensions using 70 μm nylon mesh sieves and syringe plungers. Single cell suspensions of total blood and lungs from mice were obtained and resuspended in 500 μl PBS. Rat anti-mouse Ly6G FITC (clone 1A8, eBioscience) was added to each sample (1:500). Hydrophobic barriers were drawn on standard microscope glass slides (76 mm x 26 mm x 1 mm, Marienfeld) with the use of a wax pen (Dako), generating containment wells of approximately 1.2 cm, and 100 μl of cell suspensions were added to each well as appropriate. Slides were incubated at 37°C for 20 min for cells to adhere to the glass slide, before PBS was removed and wells were gently washed with 200 μl of PBS twice. Adherent cells remaining on the glass slide were fixed with 80 μl of 2% PFA for 30 minutes, then quenched with glycine-Tris (500 mM glycine and 500 mM TrisHCl) and high salt solution (30% NaCl). Cells were then permeabilized with 0.1% PBST for 35 minutes, followed by blocking with blocking buffer (5% BSA in PBS) for 30 minutes. Wells were then incubated with 1:200 primary antibodies (anti-Col3a1 #ab7778 and IgG isotype #ab37415 from Abcam, anti-Col1a1 #600-408 from Novus biological, anti-Fibronectin #4470-4339 fromBio-Rad, anti-Laminin #L9393 from Sigma) in PBS for 1 hour and washed with excess PBS. Secondary antibody mix (1:500 goat anti-rabbit IgG Alexa fluor 555 (A-31572, Life Technologies), and 1:2000 DAPI in PBS were then applied for another 30 minutes, before washing with excess PBS. Slides were mounted with Mowiol (4-88, Sigma) until ready for imaging with a fluorescence microscope (Zeiss LSM 700) with a 40x oil objective. Imaris software (version 9.5, Bitplane) was used to surface individual Ly6G+ neutrophils and determine percentages of ECM+ neutrophils detected in the images.

For skin, colon, bone marrow and spleen, sorted cells were obtained as indicated below (cell sorting section) and resuspended in 100 μL PBS. Hydrophobic barriers were drawn on standard microscope glass slides (76 mm x 26 mm x 1 mm, Marienfeld) with the use of a wax pen (Dako), generating containment wells of approximately 1.2 cm, and 100 μl of cell suspensions were added to each well as appropriate. Slides were incubated at 37°C for 20 min for cells to adhere to the glass slide, before PBS was removed and wells were gently washed with 200 μl of PBS twice. Adherent cells remaining on the glass slide were fixed with 80 μl of 2% PFA for 30 minutes, then quenched with glycine-Tris (500 mM glycine and 500 mM TrisHCl) and high salt solution (30% NaCl). Cells were then permeabilized with 0.1% PBST for 35 minutes, followed by blocking with blocking buffer (5% BSA in PBS) for 30 minutes. Wells were then incubated with 1:200 primary antibodies (anti-Col3a1 and biotinylated anti-MPO; R&D Systems, anti-PDPN #14-5381-82 from Invitrogen) in PBS for 1 hour and washed with excess PBS. Secondary antibody mix (1:500 goat anti-rabbit IgG Alexa fluor 647 (A-21245, Thermofisher); 1:500 A488-conjugated streptavidin (BioLegend), 1:500 goat anti-Syrian hamster fluor 488 (A21110, Invitrogen) and 1:2000 DAPI in PBS were then applied for another 30 minutes, before washing with excess PBS. Slides were mounted with Mowiol (4-88, Sigma) until ready for imaging with a fluorescence microscope (Zeiss LSM 700) with a 40x oil objective. Imaris software (version 9.5, Bitplane) was used to surface individual MPO+ neutrophils and determine percentages of Collagen 3 positive neutrophils detected in the images. The same protocol was used to stain FACS-sorted neutrophils isolated from different skin areas, including ear, back, plantar, and tail.

Immunofluorescence of neutrophils for pSmad3

Single cell suspensions of total blood and lungs from mice were obtained and resuspended in RPMI (600 μl RPMI per left lung lobe, 200 μl RPMI from starting 500 μl of total blood). Rat anti-mouse Ly6G FITC (clone 1A8, eBioscience) was added to each sample (1:600). Hydrophobic barriers were drawn on standard microscope glass slides (76 mm x 26 mm x 1 mm, Marienfeld) as above and 200 μl of cell suspensions were added to each well as appropriate. Cells were given 1 minute to sink, before 100 μl of liquid was removed carefully from the top of the droplet. Slides were incubated at 37°C for 20 minutes for cells to adhere to the glass slide, before RPMI was removed and wells were gently washed with 200 μl of PBS twice. Adherent cells remaining on the glass slide were fixed with 80 μl of 2% PFA for 30 minutes, then washed with excess PBS thereafter. Cells were then permeabilized with 0.2% PBST for 10 minutes, followed by blocking with

blocking buffer (5% BSA in PBS) for 20 minutes. Wells were then incubated with 1:200 primary rabbit anti-anti-Smad3 [p Ser423, p Ser425] antibody (NBP1-77836PE, Novus Biologicals) in blocking buffer for 30 minutes, and washed with excess blocking buffer. Secondary antibody mix (1:500 donkey anti-rabbit IgG Alexa fluor 555 (A-31572, Life Technologies), 1:500 donkey anti-rat IgG Alexa fluor 488 (A21208, Invitrogen), and 1:2000 DAPI in blocking buffer) was then applied for another 30 min, before being washed with excess blocking buffer. Slides were kept in PBS until ready for imaging with a fluorescence microscope (EVOS, Thermofisher) using a consistent light intensity and capture parameters with a 20x/0.7 air objective. Imaris software (version 9.5, Bitplane) was used to surface individual Ly6G+ neutrophils and determine percentages of pSmad+ neutrophils detected in the images.

Immunofluorescence of naïve lung, skin and gut tissues for Col3a1

Mice were injected intravenously with 50µg of *Lycopersicon esculentum* (Tomato) Lectin conjugated to DyLight 649 (Vector Laboratories, Cat no: DL-1178-1) 15 to 60 minutes before euthanasia then, euthanized and perfused with 20 ml of PBS for blood removal. Lungs (post-caval lobes), gut (colon) and skin (ears) were harvested. Lung lobes were immediately placed in 2% PFA for fixation. For gut tissues, colons were split open by cutting with a pair of fine scissors and pinned to a gently shaking board covered with 0.05 M disodium ethylenediaminetetraacetate (EDTA) in RPMI 1640 at room temperature for 20 minutes, before gentle removal of the inner gut epithelia by mechanical assistance with a pair of blunt forceps, and fixation in 2% PFA. For skin, hair was first removed by application of depilatory cream (Veet), then fixed with 2% PFA. Tissues were allowed to incubate at room temperature overnight, then washed briefly in excess PBS. At this point, lungs were cut into smaller pieces (approximately 1 mm by 1 mm). The ears were split, the dorsal skin was carefully removed from cartilage, and the ventral portions were discarded. Samples were then cleared with incubation with CUBIC-L (T3740, TCI Chemicals) for 5 to 7 days at 37ºC with agitation, then briefly washed with 0.05% PBST and incubated with primary antibody (1:100) in 0.05% PBST (Col3a1: ab7778, Abcam) at room temperature for 2 days with agitation. In some cases, samples were also incubated with primary antibody (1:100) against MRP14 (Abcam, ab105472) at room temperature for 2 days with agitation. Samples were then washed with 0.05% PBST for another day. Fluorescence staining was performed with secondary antibody (1:500, donkey anti-rabbit Alexa Fluor 555 (A-31572, Life Technologies)) in 0.05% PBST with DAPI (1:1000) for two days with agitation. Samples were then washed by incubating in 0.05% PBST for another day, before overnight refractive index matching using CUBIC-R (T3983, TCI Chemicals). Imaging was performed using an SP8-STED confocal microscope (Leica) with 63X objective at a resolution of either 512 x 512 or 1048 x 1048 pixels in 16-bit in z-stacks covering a tissue depth of 50-100µm with a z-step size of 1µm. Imaris software (version 10.0, Bitplane) was used to segment individual $Ly6G^{Tomato}$ or MRP14+ neutrophils and to determine the intensity of Col3a1 signal inside and outside neutrophils.

Immunofluorescence of wounded ear skin

Wounds were performed and harvested at the indicated time points, and hair was removed by the application of depilatory cream (Veet) from ears at the time of tissue collection. Tissues were washed and immediately fixed in 2% PFA overnight, then washed in excess PBS for 1 hour, and wounded regions were isolated from the whole tissue (approximately 3.0 mm by 1.5 mm) without removing the cartilage. Samples were then permeabilized in 0.5% PBST for one to two days with agitation, then briefly washed with 0.05% PBST and incubated with primary antibodies (1:100) in 0.05% PBST (IgG isotype: ab37415, Abcam; Col3a1: ab7778, Abcam; Col4: MA5-13437, Invitrogen; Col1a1: ab21286, Abcam; Laminin: NB300-144, Novus Biologicals; Elastin: ab21610, Abcam) for 2 days with agitation. Samples were then washed with 0.05% PBST for another 1-3 days. Fluorescence staining was performed with secondary antibodies (1:500) in 0.05% PBST with DAPI (1:1000) for a day. Secondary antibodies used were Donkey anti-Rabbit Alexa Fluor 555 (A-31572, Life Technologies) and Donkey anti-Mouse Alexa Fluor 555 (A-31570, Life Technologies). Samples were then washed by incubating in 0.05% PBST for another day, before dehydration with 70% ethanol in water for at least 1 hour, followed by 100% ethanol twice for at least 1 hour each time. Samples were then cleared by incubation with BABB and imaged as above.

For 3D imaging of wounded ear skin at day 3, samples from wild-type mice were harvested and fixed overnight at 4 °C in BD Fix/Perm buffer (BD Biosciences) diluted 1:4 with PBS. Samples were permeabilized with BD permeabilization buffer (BD Biosciences) and stained overnight at room temperature with rabbit anti-mouse Col3a1 (Abcam) followed by secondary staining with anti-rabbit AlexaFluor 647 (Invitrogen). After washing, samples were incubated overnight at room temperature in Ce3D clearing solution and mounted for immediate microscopy [44,45]. Imaging was performed using an LSM 880 microscope (Zeiss) equipped with a 20x NA 1.0 objective and a tunable Ti:Sapphire two-photon laser system with non-descanned detectors, at a resolution of 512x512 pixels in 16-bit in z-stacks covering a tissue depth of 300-400 μm with a z-step size of 2 um. The Col3 imaging data and the second harmonic data generated by two-photon excitation were aligned using the channel alignment tool of the ZEN software (Zeiss) and stitched using the IMARIS stitcher (Bitplane). 3D-Visualization and volumetric rendering were performed using Dragonfly software (OCS). All imaging was performed at the Microscopy unit at CNIC or SIgN.

Multiphoton in vivo imaging of the ear skin

Hair from albino Lyz2GFP mice was first removed using depilatory cream according to manufacturer instructions, then ear wounds were performed, and imaged with an in vivo multiphoton microscope (TriMScope, LaVision Biotec) with a 20X/1.0 water objective according to previously published protocol [39]. Imaging was performed on Days 0, 1, 2, 3, 5 and 7 post-wound for 10 minutes on the same mice which were allowed to recover from light anesthesia after each imaging session. Excitation wavelength used was 950 nm, with 495nm dichroic mirror and bandpass filters used were 475/42 (SHG) and 525/50 (GFP). Time lapse of 1-minute intervals for a Z-stack of approximately 72 μm with a step size of 4 μm were recorded.
For imaging steady-state neutrophils in ear skin in LysM$^{GFP/WT}$ or Ly6G^{CRE}; Rosa26^{Tomato} mice, intravital imaging of the ear skin was performed as in [46]. We used a Zeiss LSM880 NLO intravital microscope system equipped with a femtosecond-pulsed Ti:Sapphire two-photon laser (Coherent), external non-descanned detectors and a “Plan-Apochromat" 20x lens with an NA of 1.0. Animal anesthesia was induced and maintained using isoflurane. Care was taken not to touch the ears directly to avoid any mechanical damage and low-energy 2-photon excitation (approximately 15 mW at a wavelength of 930 nm) at maximum detector sensitivity was used for skin imaging to avoid light damage resulting in highly noisy time-lapse images. Noisy images were subjected to a deep self-supervised denoising algorithm to improve the signal-to-noise ratio [47]. For some experiments, individual cells were segmented using the spot function of Imaris and tracked over time. The individual cell tracks were transferred to the same starting point and plotted in an x/y diagram. Based on the covered area over time and average density within the collagen-rich, subepidermal compartment, estimates for dynamic or static coverage by migratory neutrophils and non-migratory fibroblasts were calculated. To investigate the direct effect of neutrophils on collagen structure, we acquired high-resolution image stacks at Nyquist rates, one before and one after the passage of a neutrophil through an area, using the same LSM setup as described above. Care was taken not to inadvertently activate the neutrophils during the first image acquisition. Dynamic tracking between the two time points was then performed at low laser power and resolution as described above, and volumetric reconstruction was used to define the traversed area.

Volumetric multiphoton imaging of the skin ex vivo

LysM$^{GFP/WT}$ mice were injected under anesthesia, with 10μg anti-CD31 SuperBright 436 (clone PECAM-1; #62-0311-82; ThermoFisher) followed by perfusion with ice-cold PBS/5mM EDTA and 4% PFA (#28906; ThermoFisher) 3 min later. Ear tissues were harvested and further fixated overnight in 1:3-diluted fixation/permeabilization buffer (BD Cytofix/Cytoperm; #554714) at 4 °C. Tissue samples were further permeabilized (BD Cytoperm) and blocked using rat serum (ThermoFisher) and stained with AlexaFluor 647 anti-Ly6G (clone 1A8; Biolegend), before optical clearing using Ce3d Tissue Clearing solution (Biolegend). Whole-mount imaging was performed using a Zeiss LSM 880 NLO as above. First, GFP and AlexaFluor 647 signals were recorded using 488nm and 633nm 1-photon laser excitation, respectively, using internal detectors. Next, SuperBright 436 and second harmonics (collagen structure) were recorded with 2-photon excitation at 690nm and 940 nm, respectively, using external non-descanned detectors. Imaging was

performed in tiles at a zoom of 2.0 in stacks of 200-300 μm at step size of 2 um. After stitching (Imaris stitcher, Bitplane) a pixel classifier (Ilastik) was trained semantic segmentation of vessels. Probability masks were imported into Imaris to create volumetric surface models. GFP signals are used to create individual "LysM spots", which were further classified as neutrophils based on the presence of Ly6G surface staining. Spatial spot analysis allowed to unambiguously distinguish intra- from extravascular cells based on their location inside or outside of the reconstructed vessel model.

CNA35-mCherry imaging

To image CNA35-mCherry in the skin, the ears were cleared by incubation with CUBIC-L (T3740, TCI Chemicals), as previously described. Antibody staining for Ly6G-AF488 (Biolegend, 127626) was performed at room temperature for 2 days with agitation. Samples were then washed with 0.05% PBST for another 24h before overnight refractive index matching using CUBIC-R (T3983, TCI Chemicals). Imaging was performed using an SP8-STED confocal microscope (Leica) with 40X objective at a resolution of either 512 x 512 or 1048 x 1048 pixels in 16-bit in z-stacks covering a tissue depth of 50-150μm with a z-step size of 1μm. Imaris software (version 10.0, Bitplane) was used to identify neutrophils in the skin and segment the % volume covered by CNA35-mCherry in both neutrophil and fibroblast reporter mice.

Sample preparation and flow cytometry-assisted cell sorting

Mice were euthanized and perfused with 10 ml of PBS for blood removal. Skin (ears), colon, bone marrow and spleen were harvested as required. For BM cells, femurs were flushed using a 23–gauge needle in PBS containing 2mM EDTA and 2% fetal bovine serum (FBS). Spleens were harvested and homogenized into single-cell suspensions using 70 μm nylon mesh sieves and syringe plungers. Ear skins (dorsal and ventral side separately) were harvested and cut dry into small pieces before digested in liberase TM (Roche) and DNase1 (Sigma) for 90 min at 37°C. Skins were then homogenized into single-cell suspensions using 70 μm nylon mesh sieves and syringe plungers. Colons were harvested and cleaned of fecal matter before cutting longitudinally. Colons were washed in cold PBS and shaken once in 20ml of cold PBS in a falcon tube. Colons were then incubated in 100mM EDTA for 30 min at 37°C in shaking incubator (250rpm). Tubes were shaken once to remove epithelial cells. Colons were cut into pieces and digested in 6-well plates containing liberase TM and DNase1 for 30min at 37°C and homogenized into single-cell suspensions using 70 μm nylon mesh sieves and syringe plungers. Single-cell suspensions were stained with DAPI (1:10000), CD11b-BV510 (Clone M1/70, BioLegend) (1:200) and Ly6G-FITC (Clone 1A8, eBioscience) (1:200), and mEF-SK4-PE for fibroblasts (130-120-166, Miltenyi) (1:100). Sorting experiment was performed using a FACS Aria cell sorter (BD Biosciences) at the cytometry unit at CNIC. For experiments involving immunofluorescence of ECM proteins, we sorted $DAPI^{NEG}$, Cd11b and $Ly6G^{HI}$ cells from bone marrow and spleen, and $DAPI^{NEG}$ Cd11b+ cells from tissues with low neutrophil abundance (colon and skin), and then the cells were counter-stained for neutrophil-specific MPO. For all experiments involving transcriptomic or transcriptional analyses, neutrophils from all the different organs were exposed to the same digestion enzymes and temperature to ensure that the isolation procedure did not influence differential gene expression. In a series of additional control experiments, we have confirmed that our sample preparation protocols do not induce artifacts in gene expression.

Tissue and fiber characterization

Transmission Electron Microscopy (TEM)

Mice were sacrificed and perfused with 4% PFA, and ear skins were placed in 4% PFA and kept at room temperature for 1 hour and overnight at 40C. The skin was fixed in 2.5% glutaraldehyde and 2% paraformaldehyde in 0.1M sodium cacodylate buffer (pH 7.4) for 2 hours at room temperature, followed by overnight at 4°C. The skin was further post-fixed in 1% OsO4 and 0.8% potassium ferricyanide in the same buffer at room temperature for 1 hour. Specimens were then stained *en bloc* with 2% aqueous uranyl acetate for 1 hour, dehydrated in a graded series of ethanol up to 100%, substituted with propylene oxide, and embedded in EMbed 812 resins (Electron Microscopy Sciences, Hartfield, PA). Sample blocks were

polymerized in an oven at 60°C overnight. Ultrathin sections (60 nm) were cut using a Leica ultramicrotome (UC7) and post-stained with 2% uranyl acetate and lead citrate. The thin sections were examined with an FEI Tecnai transmission electron microscope at an 80 kV accelerating voltage, and digital images were acquired with an AMT NanoSprint15 MK2 camera (Advanced Microscopy Techniques, Woburn, MA. Processing and imaging were done at Yale School of Medicine Center for Cellular and Molecular Imaging, Electron Microscopy facility. For analysis, we segmented individual collagen fibers with Cellpose algorithm. We removed the regions not corresponding to collagen fibers (with extremely large or small areas) and we applied the watershed algorithm to ensure that each one of the detected regions corresponded to unique collagen fibers.

Scanning Electron Microscopy (SEM)

Ear samples were collected, and hair was removed by the application of depilatory cream (Veet). Skin specimens were sliced into small pieces of 2x2 mm. Ventral and dorsal halves of the ears were separated manually with forceps. Dorsal halves (without cartilage) floated for 40 min at 37˚C on 2 mg/mL dispase (Sigma-Aldrich) dissolved in PBS. The epidermal sheet was mechanically separated from the dermis. Skin samples were fixed for 30 minutes under gentle agitation in 3% glutaraldehyde solution in cacodylate buffer (100mM, Sigma C4945-25G) at room temperature. The samples were washed three times for 10 minutes in cacodylate buffer and dehydrated via ethanol series (10-100%) for 10 minutes per incubation. The surface of the samples was coated with 7 nm carbon using a Leica EM ACE600 coater before observation. Imaging of collagen fibers in the samples was performed using a Zeiss Auriga Field-Emission Scanning Electron Microscope.

Second Harmonic Generation (SHG) of collagen fibers

Mice ears were harvested, and hair was carefully and thoroughly removed by the application of Veet for 5 to 10 minutes using cotton-tip applicators, followed by several washes with PBS. Dorsal skins were then imaged with a multiphoton microscope (Olympus) at 950 nm with a water objective (20X, NA 1.0), and SHG channel was captured using ultrasensitive GaAsp photomultiplier tubes, coupled to a 500 nm long pass dichroic and a 475/42 bandpass filter, with at least 2x line averaging. For objectivity and consistency, ears were imaged at multiple fixed locations pre-defined from the tip of the ear, with 1 μm Z-step sizes for at least 16 slices from the top of the dermis. Images were then submitted to Fiji for format conversion and then subsequently submitted to CT-FIRE (version 2.0) [15] algorithmic analyses in an unbiased manner using identical batch settings. The algorithm identified approximately 800 to 1200 fibers per image, and the mean values of the fiber widths for each image was calculated separately by Python scripting.

Frangi analysis of collagen fibers from SHG

For structural analysis of the tissue collagen data in a second set of experiments, second harmonics were recorded using two-photon microscopy at Nyquist rate at a wavelength of 940 nm and then deconvoluted using Huygens software (SVI). The deconvoluted images were imported into Fiji (NIH) and the “Frangi vesselness filter” was applied to detect fiber-shape structures in the volumetric image data [48]. The filtered results were rendered in Dragonfly (OCS) or imported into the IMARIS software to be segmented with standard parameters and to extract the "vesselness" intensity as well as morphometric data of the segmented objects.

Mechanical stretch assay for tissues

Uniaxial end-to-end traction testing was used to measure the force response of lung, intestine (colon), and skin tissues. Tests were performed using a home-built tensile tester as described [49]. The tester consisted of a cell load and a linear actuator connected to a computer through a USB-6002 data acquisition system (National Instruments). Custom programming in IGOR Pro (Wavemetrics) was used to input extension protocols and to obtain output force readouts. In this setup, tissue samples were gripped at both ends by tweezers attached to the cell load or the linear actuator. After allowing the tissue samples to reach room temperature in PBS, they were assayed at a strain rate of 5 mm/s. Tissues were kept in the buffer for the

entirety of the experiment. To estimate gauge lengths, consecutive 0.4 nm extension-retraction cycles were applied at initial lengths that were increased in 0.1 mm steps. A parabolic (for gut and skin) or linear (for lung) curve fitting was applied to the maximum force values obtained at each stretch cycle. The minimum of the curve (for gut and skin) or the x-intercept (lung) was considered to mark gauge length, which was then used to determine applied strains. Tissue stiffness was calculated as the slope of the force-strain response of the first stretching cycle, and assumed that the cross-sectional area did not vary among the experimental groups.

Atomic Force Microscopy (AFM)

To measure the mechanical properties of lung, intestine, and skin tissues, we performed AFM nanomechanical spectroscopy experiments. Cre^{NEG};$TGFbR^{flox}$ control and $TGFbR^{\Delta N}$ littermate mice were euthanized and perfused with 10 ml of PBS for blood removal. Lungs (left lobe), gut (colon) and skin (left and right ears) were harvested in cold PBS. The lung lobe was cut into 1 mm slices. For gut tissues, colons were split open by cutting with a pair of fine scissors and divided into two specimens. For skin, hair was first removed by the application of depilatory cream (Veet), and a 5x3 mm rectangle specimen was cut. Measurements were performed with a commercial JPK NanoWizard III instrument (Bruker-JPK, Berlin, Germany) coupled to an inverted Axio Observer D1 optical microscope (Carl Zeiss, Germany). Freshly harvested tissues were glued to a Petri dish using Histoacryl tissue adhesive, consisting of monomeric n-butyl-2-cyanoacrylate that polymerises quickly in contact with tissue fluid (B. Braun SE, Germany).

Tissues were probed at room temperature in PBS using CP-qp-CONT-SiO cantilevers (Nanoandmore GmbH, Germany) with colloidal probes 6.6 µm in radius and a nominal spring constant of 0.1 N m^{-1}. The cantilever spring constant was calibrated before each experiment using the thermal noise method [50]**.** Force-distance (FD) curves were recorded in contact mode on the tissue surface to determine their Young's modulus. Approach-retract cycles were performed with a tip velocity of 10 µm s^{-1}, an amplitude of 7 µm and a setpoint force of 5 nN. FD measurements were spread across at least three different areas of 100 x 100 μm^2 and several millimeters apart on each tissue sample. We analyzed between 150-500 FD curves per tissue sample. Young's modulus values were calculated using the JPK Data Analysis software, by fitting the approach section of the curve to the Hertz model for spherical indenters using Equation 1:

$$F = \frac{4}{3}\frac{E}{1-\nu^2}\sqrt{R\delta^3} \quad (1)$$

In Equation 1, F is the applied force, R is the sphere radius, v is Poisson's ratio, δ is the indentation and E is Young's modulus. Tissues mostly consist of water and are considered incompressible, hence the Poisson ratio v is chosen as 0.5.

Giemsa staining of neutrophils

Cytologic examination of FACS-sorted bone marrow neutrophils from 10-week-old $TGFbR^{fl/fl}$ control and $TGFbR^{\Delta N}$ male mice was performed on cytospin preparations stained with Giemsa solution (Sigma). Sections were examined with a FSX100 microscope (Olympus).

Comparative histology of wild-type and $TGFbR^{\Delta N}$ mice

For immunohistochemical analysis on paraffin, sections were dehydrated and paraffin wax embedded. For standard Hematoxylin and Eosin staining samples were rehydrated in decreased concentrations of ethanol, then 3 min in Harris Hematoxylin, 3 seconds in Acid Alcohol and 5 min in alcoholic eosin 5% solution, dehydrated again and mounted with DPX. For Masson's Trichrome staining, the sections were deparaffinized and rehydrated in decreased concentrations of ethanol, then washed in distilled water and stained in Weigert's iron hematoxylin working solution for 10 minutes. Then the sections were washed in distilled water and stained in Biebrich scarlet-acid fuchsin solution for 10-15 minutes, washed in distilled water, and differentiated in phosphomolybdic-phosphotungstic acid solution for 10-15 minutes. Sections were transferred directly to aniline blue solution and stained for 5-10 minutes, rinsed briefly in distilled water, differentiated in 1% acetic acid solution for 2-5 minutes and washed again in distilled water. Finally, sections were dehydrated very quickly through 95% ethyl alcohol, absolute ethyl alcohol, cleared in xylene and

mounted with a resinous mounting medium. For Ki67 staining, sections were deparaffinized and brought to TBS buffer. Antigen unmasking was performed using heat-induced epitope retrieval (HIER). The citrate buffer used was Dako pH6 Target Retrieval Solution (S1699) and we used the Dako PT Link for the retrieval. The PT Link protocol is set for 20 minutes at 95º and another 20 minutes at room temperature. The slides are then washed in Wash buffer (TBST) and the immunohistochemistry is carried out in the Dako Autostainer. Endogenous peroxidase was blocked by incubation with H_2O_2 for 5 minutes and non-specific binding was prevented by incubation with fetal bovine serum (FBS) for 20 minutes to subsequently incubate with the primary antibody (anti-Ki67, Termofisher). As secondary antibodies, we used an HRP-conjugated goat anti-rabbit polymer (EnVision® K4003, Dako). For image analysis, the samples were digitalized with a scanner (NanoZoomer-2.0RS, Hamamatsu). The percentage of the skin layers (dermis, fat, muscle) was quantified with QuPath software [51] by measuring the area of every layer and the total area.

Functional assays

In vitro neutrophil culture and Col3a1 production assay

Blood and lung neutrophils from mice (1-3 x 10^5 cells) were purified by FACS, then centrifuged at 450 x g for 4 minutes, and resuspended in 450 μl of RPMI 1640 with 10% fetal calf serum (FCS). Hydrophobic barriers were drawn on standard microscope glass slides (76 mm x 26 mm x 1 mm, Marienfeld) with the use of a wax pen (Dako), generating containment wells of approximately 1 cm. 60μl of the single cell suspensions were aliquoted into each well for blood and lung samples as appropriate. The glass slides were then kept in a humidified petri dish (100 mm x 20 mm, Nunc) with 30 ml of water and a wet M-fold towel. Petri dishes containing glass slides with neutrophils were then incubated at 37˚C and 5% carbon dioxide for the designated durations. After incubation, cells were briefly washed in PBS and tapped dry against M-fold towels to remove excess liquid, then fixed with 2% paraformaldehyde (PFA) for 30 minutes. PFA was then quenched with 250 mM glycine (in water) for 5 minutes and kept overnight in PBS to prevent dehydration. Cells were subsequently permeabilized with 0.2% PBST (Triton-X 100 v/v in PBS) for 10 minutes, followed by blocking with 5% bovine serum albumin (BSA) in PBS. Primary staining was performed with 1:200 rabbit anti-mouse Col3a1 (ab7778, Abcam) and MRP14 (Abcam, ab105472) in 5% BSA for 30 minutes, followed by washes with excess PBS. Secondary staining was then performed with 1:500 goat anti-rabbit IgG Alexa fluor 555 (A-31572, Life Technologies) in 5% BSA, and followed with washes with excess PBS. Slides were mounted with Mowiol (4-88, Sigma) until ready for imaging with a fluorescence microscope (Zeiss LSM 700) with a 40x oil objective. Images were then analyzed by FIJI to determine percentages of Col3a1+ neutrophils detected in the images.

Ex vivo assessment of collagen production with CNA35 proteins.

For CNA35-GFP and CNA35-mCherry staining, live CD45+ CD11b+ Ly6G+ mCherry+ neutrophils were FACS sorted from the lungs of naïve $Ly6G^{CRE}$; $R26^{CNA35\text{-}mCherry}$ mice and incubated overnight on glass coverslips at 37°C in DMEM containing 10% FBS, 10ng/ml TGFβ and 10ng/ml G-CSF and 0.2μM CNA35-GFP. After 16-hour incubation, we performed fixation, permeabilization, and blocking as outlined above. The cells were then incubated overnight at 4°C with 1:200 primary chicken anti-GFP and rabbit anti-RFP antibodies (A10262, Invitrogen, and 600-401-379, Rockland, respectively) and washed with excess PBS. Secondary antibody staining with anti-chicken Alexa Fluor 488 (A-11039, Invitrogen) and anti-rabbit 647 (ab150079, Abcam) was performed at room temperature for 1 hour, followed by washing and 1:2000 DAPI staining for 5 minutes at room temperature. Deposits of CNA35 surrounding individual collagen-producing and non-producing cells were quantified within an area of 100μm x 100μm by masking the intracellular collagen signal, applying uniform thresholds for signal intensity and voxel size across different images, and subsequently generating volumetric reconstruction of extracellular collagen signal. The total area of and the total number of extracellular collagen specks were compared between collagen-producing and non-producing neutrophils. CNA35-GFP was produced in bacteria transduced with the pET28a-EGFP-CNA35 plasmid was purchased from Addgene (#611603).

Permeability assays

Skin permeability: Wounds were performed on mice ears and harvested after 3 days. Hair was removed by the application of depilatory cream (Veet). Thereafter, 2 μl of 10 mg/ml Evans blue dye (E2129, Sigma) in PBS was carefully applied directly over the wounded region and incubated for 1 hour at room temperature. To prevent the Evans blue dye from drying out, ear tissues were placed on dry glass slides, which were in turn placed on wet C-fold towels held in partially filled water-containing petri dishes. After incubation, samples were washed briefly in excess PBS for a few seconds, and submitted for imaging by multiphoton microscopy (Oympus) at 1200 nm. Images were subsequently analyzed using Fiji software. For naïve ear and plantar skins, mice were anesthetized and a 25 μl drop of Evans blue dye (concentration 10 mg/ml) in PBS was spread on the ear. After 1 hour, mice were sacrificed and ears were harvested and weighed. After being washed briefly in excess PBS, samples were submerged in 0.5 ml formamide and incubated at 55 °C for 24 h. Then, tissues were removed and centrifuged for 5 min at 645g. Finally, supernatants were measured for absorbance at 610 nm using an xMark Microplate Spectrophotometer (BioRad) plate reader.

Intestinal and lung permeability: to measure intestinal permeability, mice were water-starved the night before. The next day fluorescein isothiocyanate conjugated dextran (FITC-dextran) (222 mg/Kg; Sigma-Aldrich F4) was administered by oral gavage. After 4 hours, blood was collected, and mice were sacrificed. For lung permeability, FITC-dextran (30 mg/Kg) was administered intratracheally, and blood was collected after 2 hours. The concentration of FITC in serum was determined by spectrofluorometry (Fluoroskan™ Microplate Fluorometer; Thermo Fisher) with an excitation of 485 nm and an emission wavelength of 538 nm. Serum from mice not administered with FITC-dextran was used to determine the background.

Vascular permeability: A 0.5% solution of Evans blue in sterile saline was prepared and 200 μl of the solution was injected intravenously. Mice were sacrificed 30 minutes later, and tissues were extracted, weighed, and processed as above for absorbance reads.

Infection susceptibility assay of wounded ear skin

Staphylococcus aureus (Newmann strain) was grown in Brain Heart Infusion (BHI) overnight at 37˚C. The overnight culture was then diluted in sterile BHI and grown to an optical density at 600 nm (OD600) of 1. The culture was centrifuged at 5524 g for 15 minutes. The pellet was resuspended at a concentration of 10^9/ml. Mice were anesthetized and 6 wounds were performed on the left ear with a 30G insulin syringe. After 3 days, mice were anesthetized and a 150 μl drop of S. aureus (concentration 10^9/mL) was positioned on the ear. After 1 hour, the S. aureus drop was thoroughly washed with PBS and 3 days post infection mice were sacrificed and left ears were collected. Ears were cut into small pieces and digested for 40 minutes at 37˚C with Liberase. Skin samples were then filtered through 70 μm cell strainer and centrifuged at 1000 g for 5 minutes. The supernatant was discarded, and the pellet was resuspended in PBS with 0.1% Triton X. Desired serial dilutions with PBS were made and plated on BHI dish at 37˚C overnight. CFU/ear was calculated based on the dilutions performed.

Bacterial dissemination from the wound

Neutrophils were depleted by intraperitoneal administration of the anti-Ly6G antibody into C57BL/6 wild-type mice for two consecutive days, as indicated above. Six wounds were performed on the ears of neutrophil-depleted, TGFβR$^{\Delta N}$, Col3a1$^{\Delta N}$ mice and their respective littermate controls with a 30G insulin syringe. Three days after wounding, mice were anesthetized and a 150μl drop of 10^9/ml CFU of *S. aureus* was placed on each ear. After 1 hour, the drop was thoroughly washed with PBS and at 4 hours post-infection mice were sacrificed. The ears were harvested and fixed overnight at 4 °C in 4% PFA, and the next day washed 3 times with PBS for 1 hour at room temperature, permeabilized in methanol gradients, and blocked for 1 hour (0.3% Triton X100, 0.2% BSA, 5% DMSO, 0.1% Azide, 5% serum in PBS). Samples were then stained overnight with the primary anti-*S. aureus* antibody (Abcam), followed by 2-hour staining with anti-rabbit AlexaFluor 647 (Invitrogen) secondary antibody and DAPI. After two one-hour washes with

PBS, the samples were cleared with ethyl cinnamate (ECI). Imaging was performed using an SP8-STED confocal microscope (Leica) with 20X objective at a resolution of either 512 x 512 or 1048 x 1048 pixels in 12-bit in z-stacks covering a tissue depth of 100-200µm with a z-step size of 1-3µm. Distance of *S. aureus* to the wound edge was performed using Imaris software by automatically or manually creating a wound surface based on the DAPI signal and calculating the distance transformation for the *S. aureus* AlexaFluor647 signal.

Ex vivo functional assays of neutrophils

DH5a Escherichia coli (E. coli) expressing GFP [52] were grown in LB medium overnight at 37˚C, at which point the bacteria were diluted and grown for 3 hours to an OD600 of 0.5, and thereafter washed twice with PBS. *S. aureus* (strain Newman) were grown in Tryptic Soy (TS) medium overnight at 37˚C, at which point the bacteria were diluted and grown for 2 hours to an Optical Density (OD) at 600nm (OD600) of 0.4-0.6, and thereafter washed twice with PBS. To check for intracellular cytokine expression and phagocytosis rates, 1 x 10^6 sorted lung neutrophils were stimulated with either bacteria (1:100 neutrophil:bacteria ratio) in complete RPMI media with 10% FCS in 96-well plate wells for 2 hours (37˚C, 5% CO2) in the presence of GolgiStop and GolgiPlug (BD Biosciences) at dilutions recommended by manufacturer instructions. Cells were stained with a fixable viability dye (Zombie UV fixable viability kit; Biolegend), then fixed with fixation/permeabilization buffer (BD Biosciences) before staining with anti-TNFα antibody (MP6-XT22, eBioscience), and iNOS/NOS2 (CXNFT, eBioscience), washed, then submitted for flow cytometry (BD LSR II using FACSDiva software, and data was subsequently analyzed by FlowJo software (Tree Star). For killing assays, sorted neutrophils were incubated with bacteria (ratio of 1:50) in complete RPMI media (RPMI, 10% FCS) in 96-well plate wells for 2 hours (37˚C, 5% CO2). After incubation, the culture media was diluted (10^{-4} for S. aureus, 10^{-6} for E. coli) and 100µL was plated evenly on LB agar plates, then incubated overnight at 37˚C. Colonies on the plates were counted and normalized colony-forming units (CFU) was calculated.

For in vitro NET formation assays, 4x10^4 Ly6G+ lung neutrophils were plated in serum-free RPMI medium on poly-l-lysine covered 8-well µ-Slides (Ibidi) and left for 30 minutes at 37°C in a cell culture incubator to adhere. Cells were plated in a drop of medium in the center of the well to enhance their adhesion in the central area of the well and to avoid their deposition in the edges. Cells were subsequently incubated for 2 hours with 100 nM PMA. Then cells were fixed using 4% paraformaldehyde (PFA) in PBS for 10 minutes, blocked, and permeabilized with PBS containing 0.1% Triton X-100, 25% FBS, and 5% BSA; they were stained with antibodies against citrullinated histone 3 (citH3, ab5103, Abcam) and myeloperoxidase (MPO, AF3667, R&D Systems) in 1:200 dilution in blocking buffer, at 4°C overnight. Then, the cells were washed and stained with secondary antibodies: donkey anti–goat-Cy2 (705-225-147, Jackson ImmunoResearch) and donkey anti–rabbit-AF555 (A31472, Invitrogen) 1:400. They were counterstained with DAPI (1:1000) for 2 hours at room temperature. Images were acquired with an EVOS and analyzed with ImageJ (NIH) to identify NETs (defined as triple-positive colocalization events of DNA, citH3, and MPO).

To measure reactive oxygen species (ROS, using Oxidative Burst Assays), 3x10^4 Ly6G+ lung neutrophils were incubated with 2.5mg/mL Dihydrorhodamine 123 (DHR) (ThermoFisher) in RPMI and subjected to 50nM Phorbol 12-Myristate 13-Actetate (PMA) (Sigma-Aldrich) for 20 min at 37°C. Cells were subsequently washed with PBS and the median fluorescence intensities were measured by flow cytometry.

For chemotaxis assays (Transwell Migration Assay), sorted Ly6G+ lung neutrophils were positively selected using EasySep selection kits (Stem Cell Tech), and 10^5 neutrophils were used per condition. 12-well transwell plates (Corning) containing 3 µm PET membranes inserts were used. Bottom wells were filled with 250 µL RPMI + 10% FCS before placing the insert on, and were left to equilibrate for 1hr 37°C. We then added 20 µl of CXCL12 chemokine (Peprotech, 2µg) or RPMI to each bottom well. The membrane inserts were placed back on 100 µl of cells were added onto the membrane insert. After 90 min of incubation at 37°C, 5% CO2, inserts were removed and 100µl 0.5M EDTA was added into each bottom chamber and

incubated for 10 min, 4°C. Then, media from the bottom well was collected and washed with 1ml FACS buffer before quantification by flow cytometry.

Transepidermal water loss measurement (TEWL)

Hair from the back and ear skin of TGFbRΔN mice and $TGFbR^{fl/fl}$ littermates was removed with depilatory cream (Nair) two days prior to TEWL measurements. Mice were anesthetized with isoflurane and Tewameter TM 300 (Courage-Khazaka Electronic, Germany) was used to measure TEWL. As positive control measure, the back skin of control $TGFbR^{fl/fl}$ mice was tape-stripped prior to TEWL measurement.

Data and Code Availability

All the transcriptomics data are available in Gene Expression Omnibus (GEO) and proteomics data in Proteomics Identification Database (PRIDE). The individual GEO accession numbers are as follows: bulk RNA-seq from neutrophils in parabiotic tissues (GSE141745); bulk RNA-seq from tissues at varying circadian timepoints (GSE198770); bulk RNA-seq from $TGFbR^{\Delta N}$ neutrophils (GSE198654); bulk RNA-seq from skin fibroblasts (GSE202738); single cell RNA-seq from skin tissue (GSE229493, GSE271969), ATAC-seq from tissue neutrophils (GSE141285). For proteomics data, they have been deposited to the ProteomeXchange Consortium via the PRIDE partner repository with the dataset identifiers as follows: blood and lung cell lysates (PXD031943); neutropenic tissues (PXD031950); and wounded skin tissue (PXD031952).

Statistical analysis

Unless otherwise indicated, data are represented as mean ± standard error of the mean, box and whiskers or showing individual values, and analyzed using Prism software (GraphPad, Inc.). Datasets were analyzed by a D'Agostino-Pearsons normality test to define normality and implement the appropriate statistical test. Data consisting of only two datasets were analyzed using two-tailed Student´s t-test unless otherwise stated. To identify statistically significant differences for treatment/genotype over time or more than two datasets we used two-way ANOVA or one-way ANOVA with Tukey's or multiple comparisons tests, respectively. For determination of diurnal patterns, we used COSINOR fitting of circadian curves and the Amplitude versus zero test [19]. A p-value below 0.05 was considered statistically significant. Experimental findings were confirmed in independent experiments and found to be reproducible. All experiments were repeated at least 2 times using separate cohorts.

Extended data

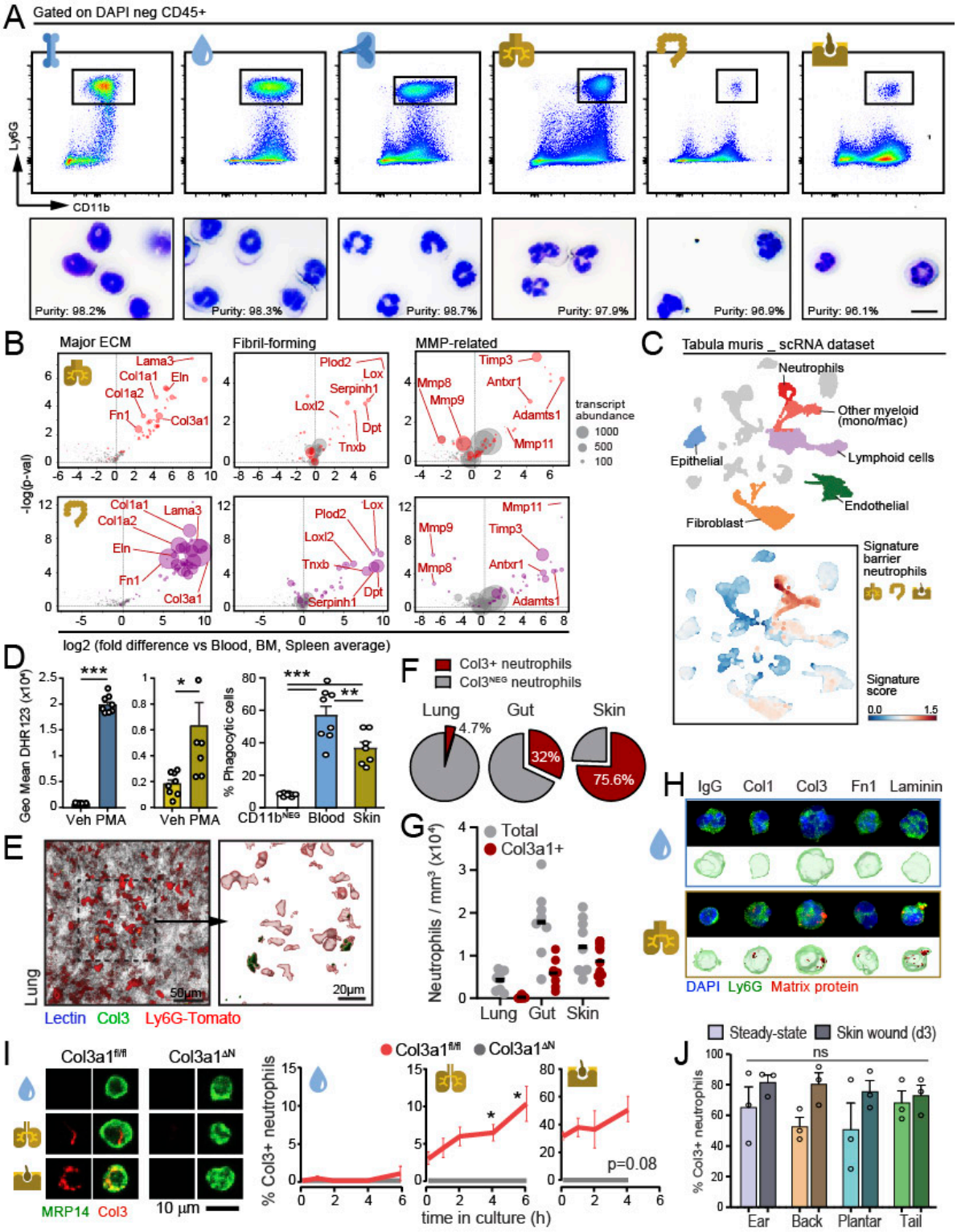

Extended data Fig.1. Matrix-producing neutrophils in barrier organs. (A) Isolation gates for sorting Ly6G^{HI} neutrophils from the indicated tissues, with representative images of cytospins of the sorted cells and purities from a representative experiment; scale bar, 10 µm. (B) Volcano plots showing transcript enrichment in lung, skin and intestine relative to the levels found in the three sterile tissues. Data from the transcriptome shown in Fig.1A. (C) Computational validation in single cell datasets showing that cells sorted for the analyses shown in Fig.1A retain a neutrophil transcriptional identity. A signature score of the cells sorted and sequenced in Fig.1A (top 500 genes) was projected over a map of multiple cell types from the Tabula muris dataset and show strongest identity with the neutrophil cluster. (D) Left, ROS production after vehicle or PMA stimulation by blood or skin neutrophils, measured by fluorescence of the probe DHR123. Right, frequency of neutrophils from blood and skin that phagocytose fluorescent beads, using CD11b^{NEG} cells as negative control. Data is from 7-9 mice per group and shown as mean ± SEM. **, p<0.01; ***,

p<0.001 determined by two-tailed Student´s t-test (ROS) or one-way ANOVA (phagocytosis). (E) Immunofluorescence analysis of barrier tissues to score the abundance of Col3a1+ (green) neutrophils in $Ly6G^{Tomato}$ mice (red) stained for vessels with *L. esculentum lectin* (grey). Left, representative images of neutrophils in lungs; right, 3D reconstructions showing the presence of Col3a1 inside the neutrophils (F) Pie charts show the frequencies of Col3a1+ Mrp14+ cells in the indicated tissues; data from 8-9 images per tissue from 4 mice. (G) Number of all neutrophils or only Col3a1+ neutrophils per imaged volume area in the indicated tissues; data from 8-9 areas from 4 mice. Note that in lung the calculated neutrophil densities were lower due to the much greater tissue volumes compared to skin and gut, despite having higher absolute total counts. (H) Representative immunofluorescence micrographs of the indicated matrix proteins in neutrophils from blood and lungs. Images are representative of 300 cells from 3 mice. (I) Production of collagen by neutrophils ex vivo. Neutrophils sort-purified from blood, lung or skin of wild-type and $Col3^{\Delta N}$ ($Mrp8^{CRE}$; $Col3a1^{fl/fl}$) mice were set in culture for the indicated times and stained for the presence of Col3a1. Graphs show the kinetics of the frequency of Col3a1+ neutrophils. Data are shown as mean ± SEM and is compiled from 3 independent experiments and 3-4 mice. Statistical comparison of every time point versus time zero was calculated by unpaired Student's t-test. *, p<0.05. (J) Percentage of Col3a1+ neutrophils extracted from the indicated skin regions. Data from 30-80 neutrophils from 3 mice. Bars show mean ± SEM analyzed by two-way ANOVA with Tukey's multiple comparisons test.

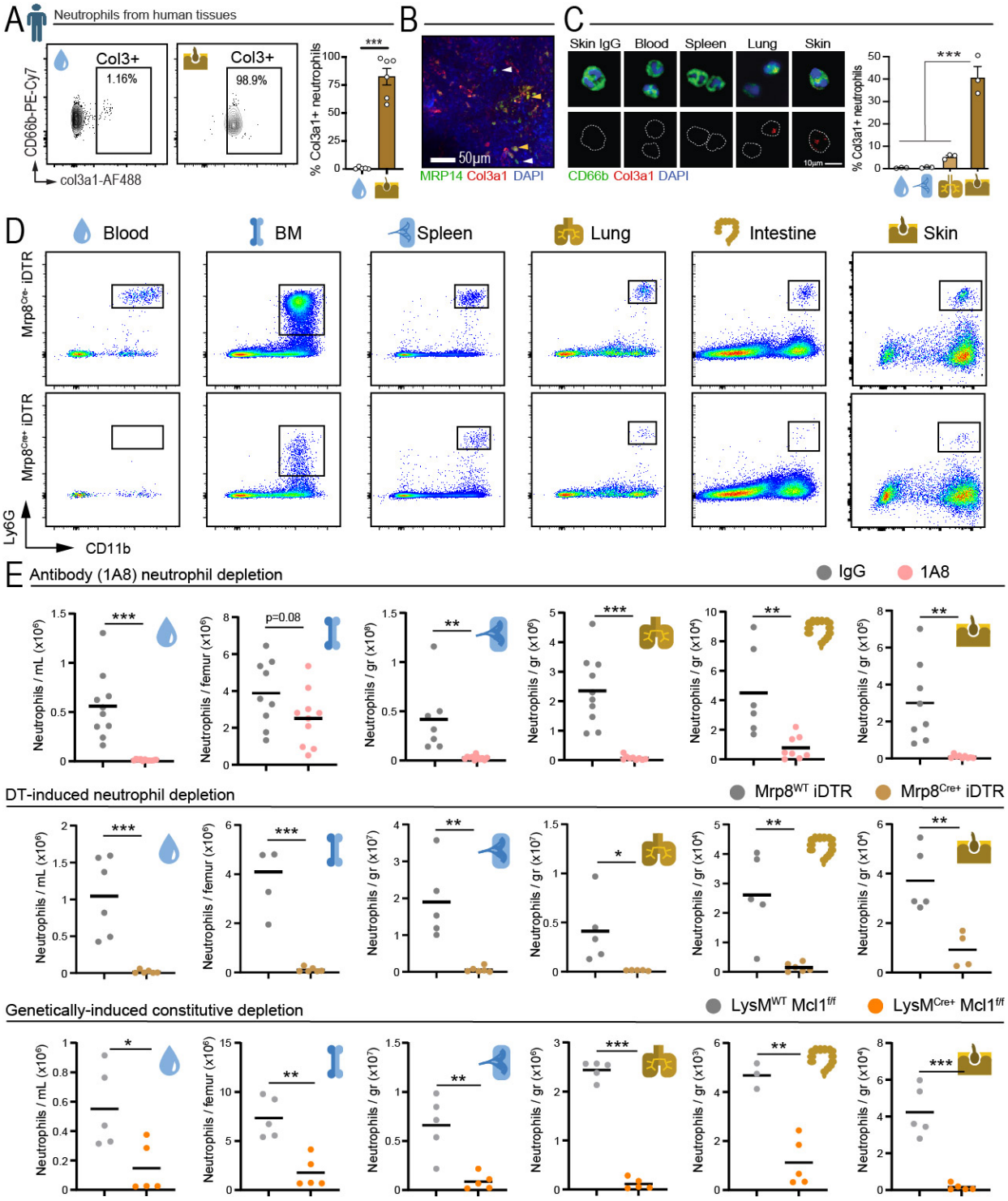

Extended Data Fig.2. Human neutrophils and neutropenia mouse models. (A) Cytometry plots showing the frequency of Col3+ neutrophils of human skin and blood and quantification of percentages (right). Bars shown mean ± SEM from 5 to 6 samples. ***, p<0.001 determined by unpaired t-test. (B) Image of a cleared human skin sample stained for neutrophils and Col3a1. White arrowheads show Col3-negative neutrophils, and yellow arrowheads Col3+ neutrophils. Image is representative of 3 donors. (C) Representative images of Col3a1 staining in sorted neutrophils from human blood, spleen, lungs, and skin. Negative control IgG staining is shown for human skin neutrophils. Right, percent Col3a1+ neutrophils in barrier and non-barrier human tissues. Data is from 3 human specimens per tissue. ***, p<0.001 as determined by one-way ANOVA with multigroup comparison test. (D) Representative cytometry plots and gating strategy for neutrophils across the indicated tissues (iDTR model). (E) Neutrophil numbers in tissues by flow cytometry of the three neutropenia mouse models and their respective controls (IgG, MRP8^{WT}; iDTR and LyzM^{WT}; Mcl1^{flox}, respectively). Mice were treated intraperitoneally with either anti-Ly6G (1A8, 3 µg/g) or control IgG (3 µg/g) antibodies or diphtheria toxin (DT, 10 µg/kg) for two consecutive days and tissues were collected on the third day. Data from 5-9 mice per group. *, 0.05; **, p<0.01; ***, p<0.001 as determined by unpaired t-test.

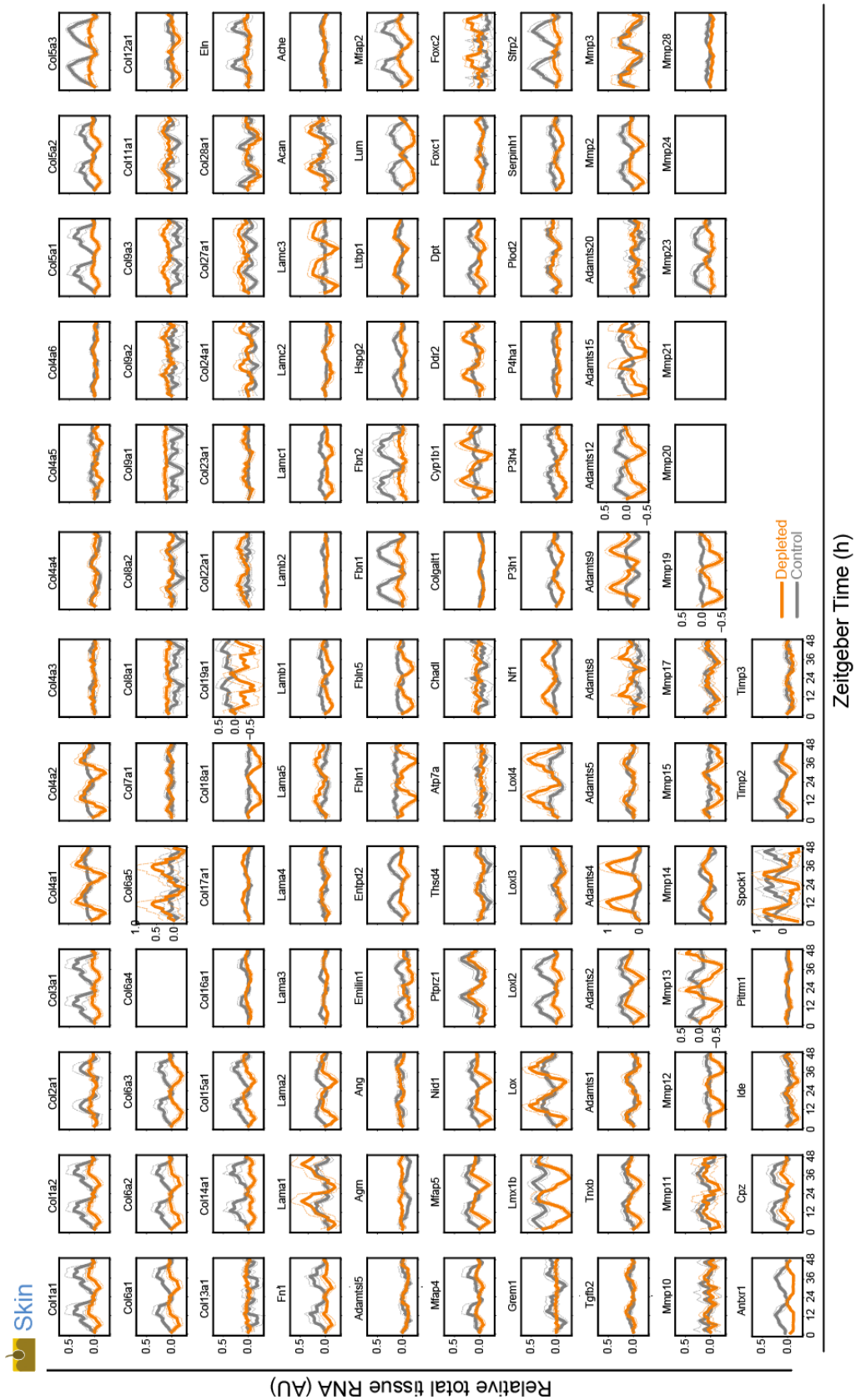

Extended Data Fig.3. Circadian patterns of the matrix transcriptome in the skin. Circadian expression pattern of total skin mRNA in neutrophil-depleted (iDTR, orange) or control (gray) mice. For each gene, total tissue RNA levels were smoothed and normalized to the ZT where control curve was at minimum as baseline to focus on showing the variations in gene expression. (raw data available through this paper). Empty boxes represent undetected genes. See Fig.2A-B for the experimental scheme and general representation of the data.

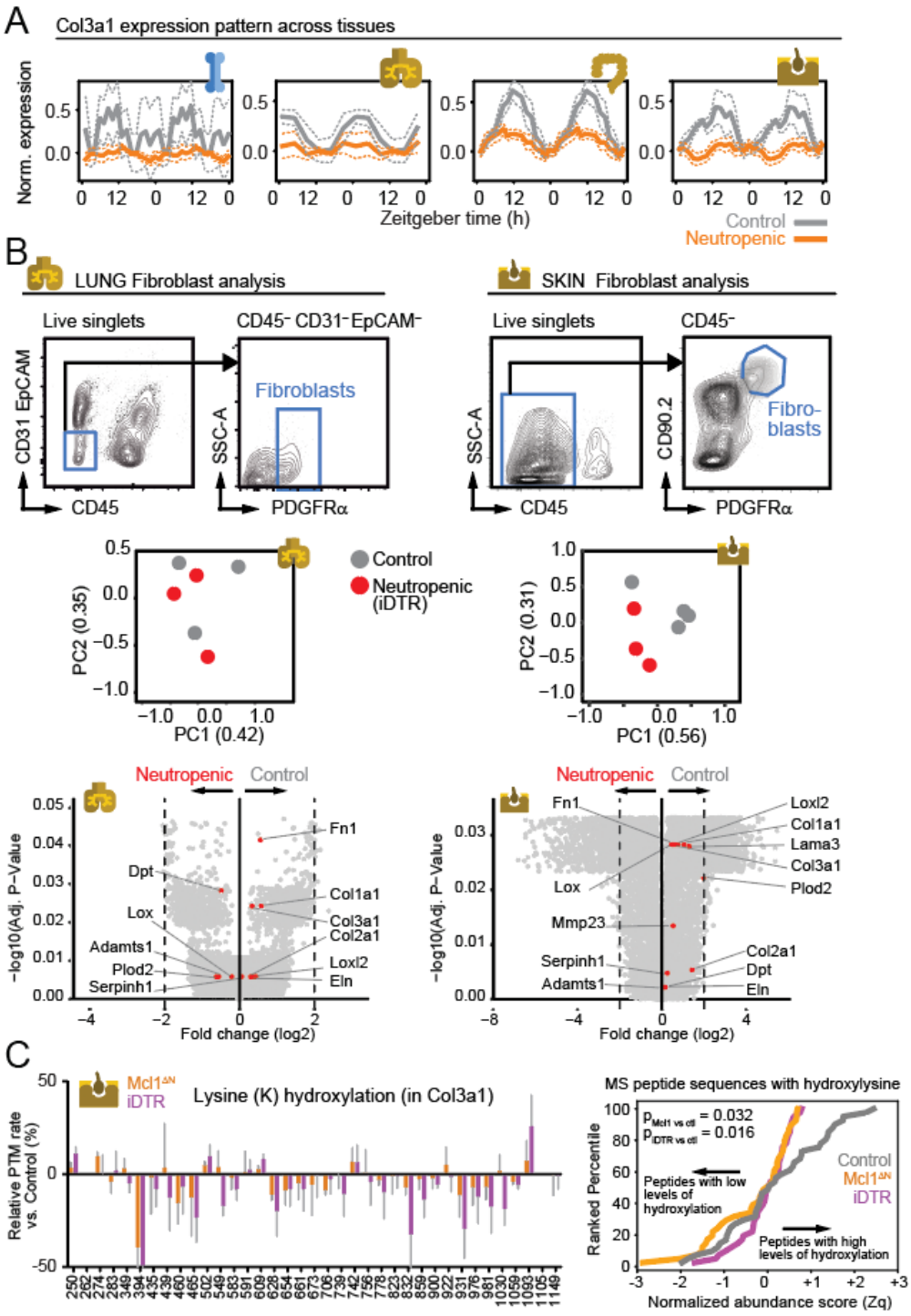

Extended Data Fig.4. Matrix production in the skin of neutropenic mice. (A) Circadian expression patterns of *Col3a1* across different tissues, in control or neutrophil-depleted mice. Experimental design as in Fig.2A. (B) Sort-based isolation of fibroblasts from lung and skin of control and neutropenic mice (iDTR, 7 days), which we used for bulk RNA sequencing. Principal component analyses show no effect of depletion in the global transcriptional profile of fibroblasts, and volcano plots (bottom) highlight similar transcription for key matrix genes as defined from Fig.1 and the circadian analyses in Fig.2. Note that –log adjusted p values are well below significance levels (defined as > 1.3). (C) Analysis of lysine hydroxylation of Col3a1 in the skin as determined by mass spectrometry. Controls for both groups were wild-type Mcl1 littermates (n=4) treated with DT (with no effect in absence of expression of DTR). (Left) Hydroxylation post-translational modification (PTM) rates were estimated per lysine residue and relative PTM rates were derived by subtracting the baseline PTM rates (control mice) from neutropenic groups. X-axis indicates Col3a1 protein lysine residue position labels. The midline represents the control group against which the values in neutropenic mice are calculated. Error bars are SEM, from 3-4 mice per group. (Right) Cumulative distribution functions of all permutations of Col3a1 peptide sequences (n=42 sequences) detected to contain hydroxylysine, analyzed by two-tailed two sample Kolmogorov–Smirnov (KS) tests, comparing neutropenic curves against the control curve. Only high-confidence peptide sequences with at least 3 detected peptide-spectrum matches (PSM) were plotted for analysis.

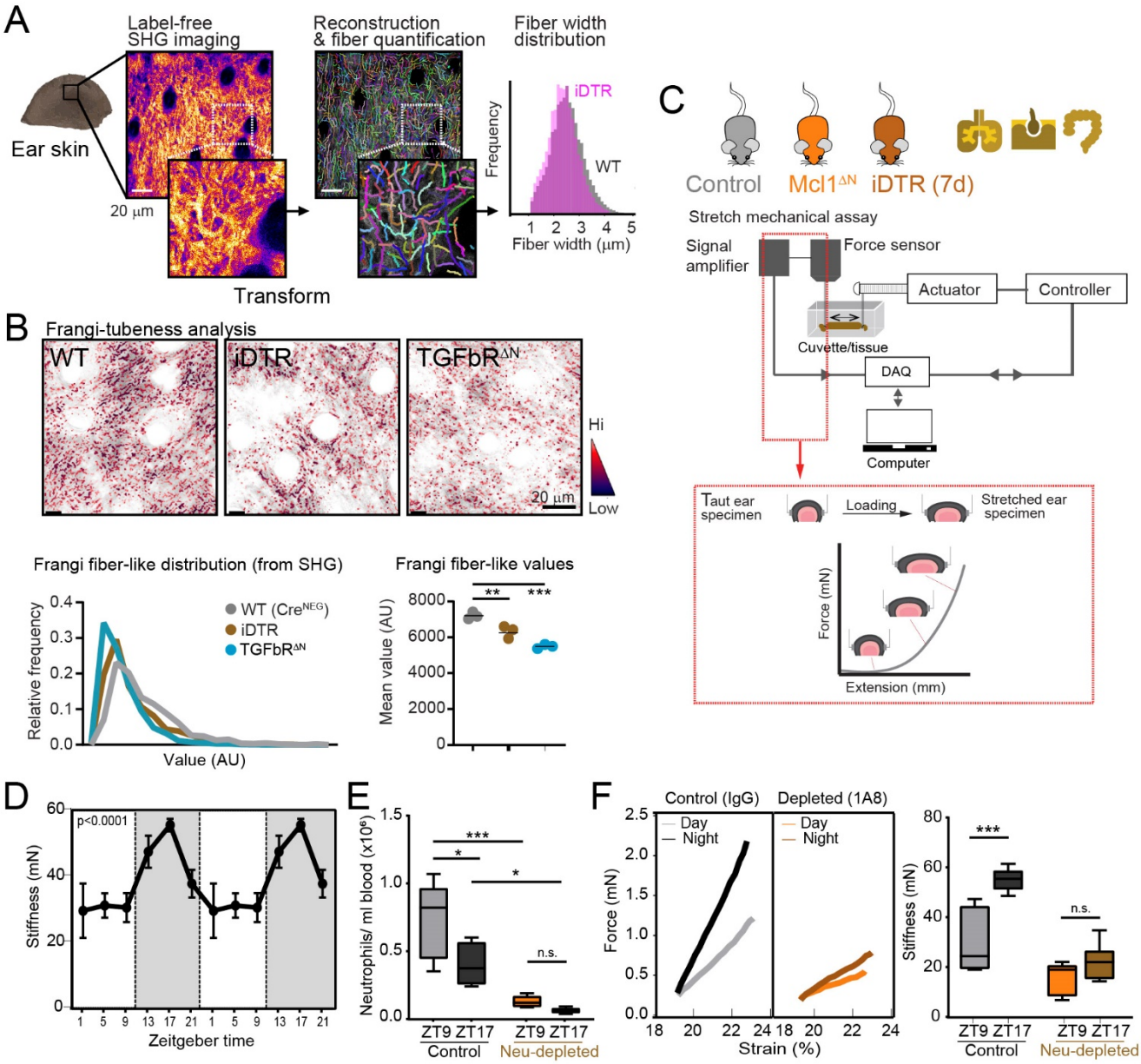

Extended Data Fig.5. Structure and mechanics of the skin. (A) Second Harmonic Generation (SHG) in the ear skin to determine average fiber width using CT-FIRE (see Methods). (B) We also used an alternative approach to measure fiber "vesselness" to detect potential changes in fiber structure using the Frangi score (colored as shown in the scale). More signal in the control group (Cre-negative Rosa26^{iDTR} littermates) defines more typical fibrous structures for matrix than the iDTR and TGFbR$^{\Delta N}$ mice, as also shown in the quantifications below; data is from 3 mice per group. **, p<0.01; ***, p<0.001 as determined by multiple t-test. (C) Experimental design and schematics of the tensile tester used to measure the passive force of tissues at defined strains (see Methods). (D) Skin stiffness at different times of day (zeitgeber or ZT), which display marked circadian variations; n=5-8 mice per time point; p value was calculated using the amplitude vs. zero test [19]. Neutrophil depletion using anti-Ly6G antibody (1A8) (E) caused loss of diurnal variations in skin stiffness (F) measured at the trough and peak times (ZT9 and ZT17). Data from 6-8 mice. *, p<0.05; **, p<0.01; ***, p<0.001 as determined by one-way ANOVA analysis (C, E, F).

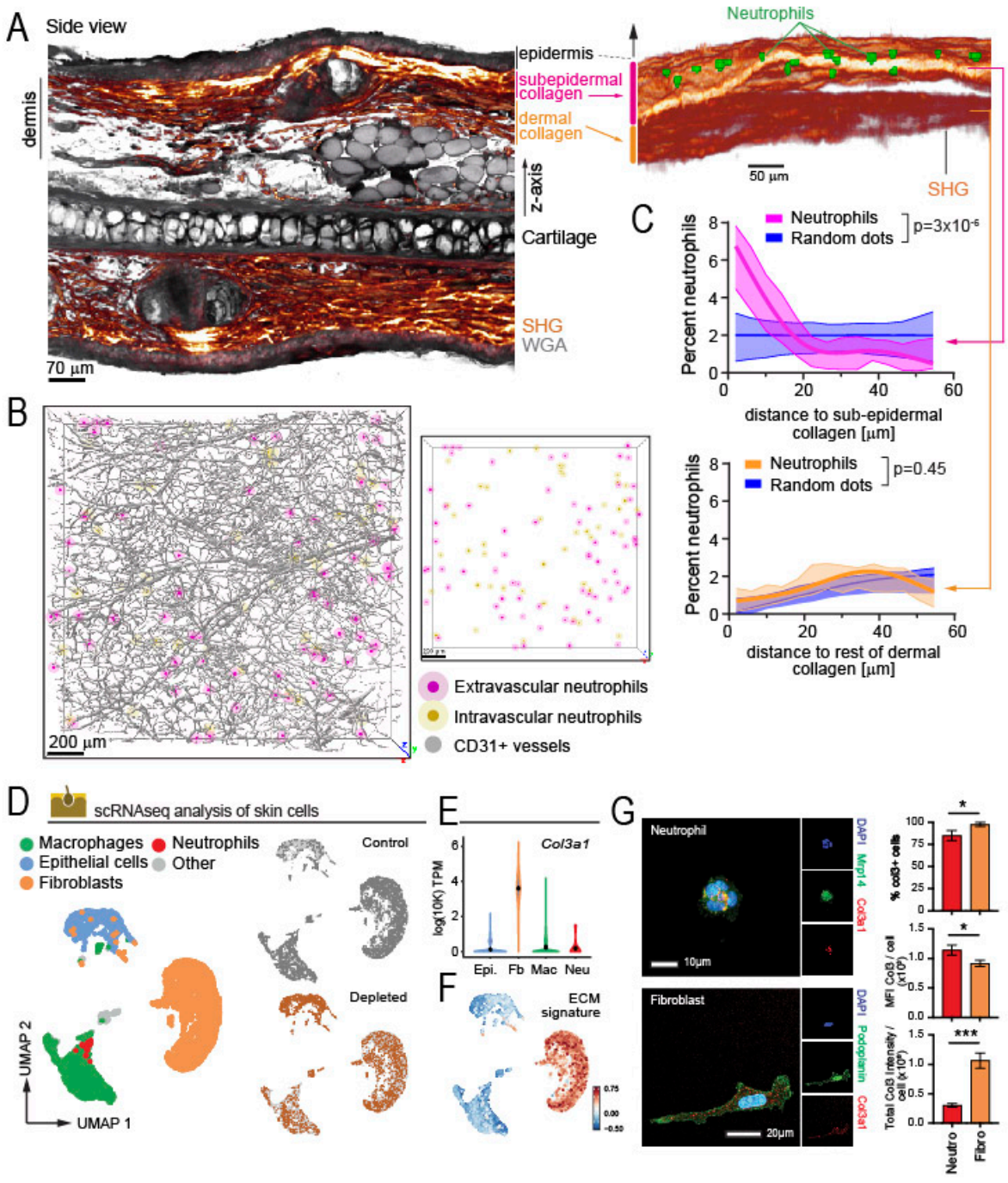

Extended Data Fig.6. Collagen-producing neutrophils localize near sub-epidermal fibers. (A) Multiphoton sectional imaging of ear skin explants of LysM^{GFP} mice with anti-Ly6G (for neutrophils) and wheat germ agglutinin (WGA, for vasculature), combined with SHG to show the position of the subepidermal collagen layer and, at right, SHG imaging of this layer above looser collagen in the rest of dermis, with several neutrophils shown from a side view. (B) Reconstruction of a 1.5 x 1.5 mm region of the ear skin imaged from the top by two-photon imaging showing the network of CD31+ vessels as well as intravascular (yellow) and extravasated (pink) neutrophils as also shown in the inset at right. Images are representative of 4 mice. (C) Distribution of distances for neutrophils to sup-epidermal and dermal collagen compared with random dots, illustrating the preferential localization of neutrophils near the sub-epidermal layer of collagen. Data from 193 cells and 3 mice. P values were calculated using the two sample Kolmogorov–Smirnov tests comparing the sample distributions of the empirical distances against the simulated randomly generated dots. (D) scRNA-seq of the ear skin, with UMAP showing the main identified clusters corresponding to the indicated cell types, and distribution of the cells in control and neutrophil-depleted (anti-Ly6G, 2 days) skins. (E) Violin plots showing expression of the *Col3a1* gene across the different cell types in the skin and (F) expression of the matrix signature (genes from Fig.1A) in the different clusters, showing the strongest expression in fibroblasts. (G) Representative images of one neutrophil and one fibroblast stained for Col3 and specific markers (Mrp14 and Podoplanin, respectively). Right, quantification of Col3+ frequencies and Col3 signal intensity per cell area or in total cells from the immunofluorescence images. Data is shown as mean ± SEM from 60-70 neutrophils and 30-40 fibroblasts from 3 mice. *, p<0.05; ***, p<0.001, determined by unpaired Student's t-test.

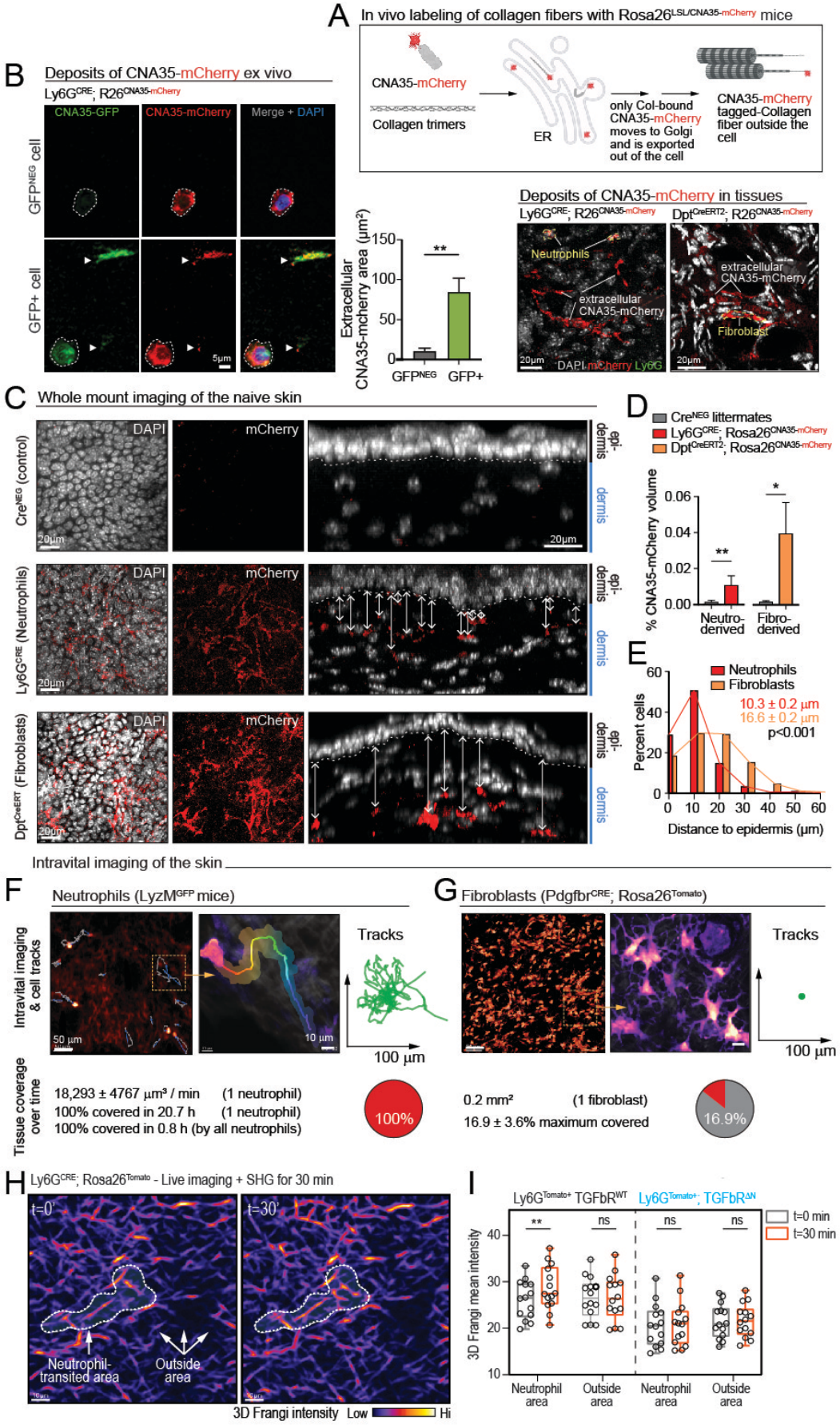

Extended Data Fig.7. Neutrophils deposit collagen and regulate collagen fibers in the skin. (A) Mechanism of collagen tagging by CNA35-mCherry inside cells. This strategy was used to generate the Rosa26$^{LSL;\ CNA35\text{-}mCherry}$) reporter model, which allows Cre-dependent expression of a fluorescent form of CNA35, a collagen-binding protein of bacterial origin. Cell-specificity in this model is permitted because the fluorescent protein lacks an export signal and

cannot be sorted out of the endoplasmic reticulum unless it binds trimeric collagen, thereby preventing unspecific labeling of collagen produced by other cells. (B) Left, representative images of ex vivo cultured lung neutrophils from CNA35-mCherry reporter mice showing deposition of CNA35-mCherry that also binds CNA35-GFP (arrowheads). These extracellular deposits are not seen in neutrophils that do not produce collagen. Right, in vivo CNA35-mCherry labelling extracellular matrix in the neutrophil and fibroblast reporter mice. (C) Top and side views of the skin from $Rosa26^{LSL/CNA35\text{-}mCherry}$ reporter mice crossed with Cre^{NEG} control mice, and $Ly6G^{CRE}$ or $Dpt^{CreERT2}$ driver lines to induce CNA35-mCherry expression in neutrophils and fibroblasts. $Ly6G^{CRE}$ targets mature neutrophils, while $Dpt^{CreERT2}$ is expressed by 60% of fibroblasts. Arrows show distances of CNA35-collagen to the epidermis. (D) Volume percent of CNA35-mCherry in the naive skin of the indicated reporter lines, and (E) distance to the epidermis of collagen produced by neutrophils or fibroblasts. *, $p<0.05$; **, $p<0.01$, determined by two-way ANOVA. (F-G) Intravital imaging experiments of the ventral ear skin of $LysM^{GFP}$ (F) or $Pdfgr^{CRE}$; $Rosa26^{tdTomato}$ (G) mice performed over 2.5 hrs to visualize and measure the dynamics of neutrophils ($LyzM^{GFP}$; 3 mice) and fibroblasts ($Pdfgbr^{Tomato}$; 4 mice). Individual cell tracks (green) are shown for neutrophils and fibroblasts. Imaging was performed by two-photon microscopy at low energy and high sensitivity followed by AI-driven image restoration to minimize tissue damage and prevent immune activation or death. Bottom, values are calculations based on parameters extracted from the imaging experiments that estimate tissue coverage for each lineage over time. Note that area coverage on a per cell basis is much higher for neutrophils because they constantly scan the skin tissue (area of coverage shown in the left top image). (H) Neutrophil tracks (white outline) and collagen fibers (visualized by Frangi intensities) captured by 2-photon microscopy over 30 min in the living skin of $Ly6G^{CRE}$; $Rosa26^{TOMATO}$; $TGFbR^{\Delta N}$ and $Ly6G^{CRE}$; $Rosa26^{TOMATO}$ control mice. (I) Quantification of the Frangi intensities at times 0 and 30min inside or outside areas transited by neutrophils. Frangi scores, reflecting fiber size and structure, are higher only in areas transited by wild-type neutrophils, and the response is lost in $TGFbR^{\Delta N}$ mice. Data is from 14 cells per group, from 6 mice. *, $p<0.05$; n.s., not significant, determined by two-way ANOVA with Sidak multigroup comparison test.

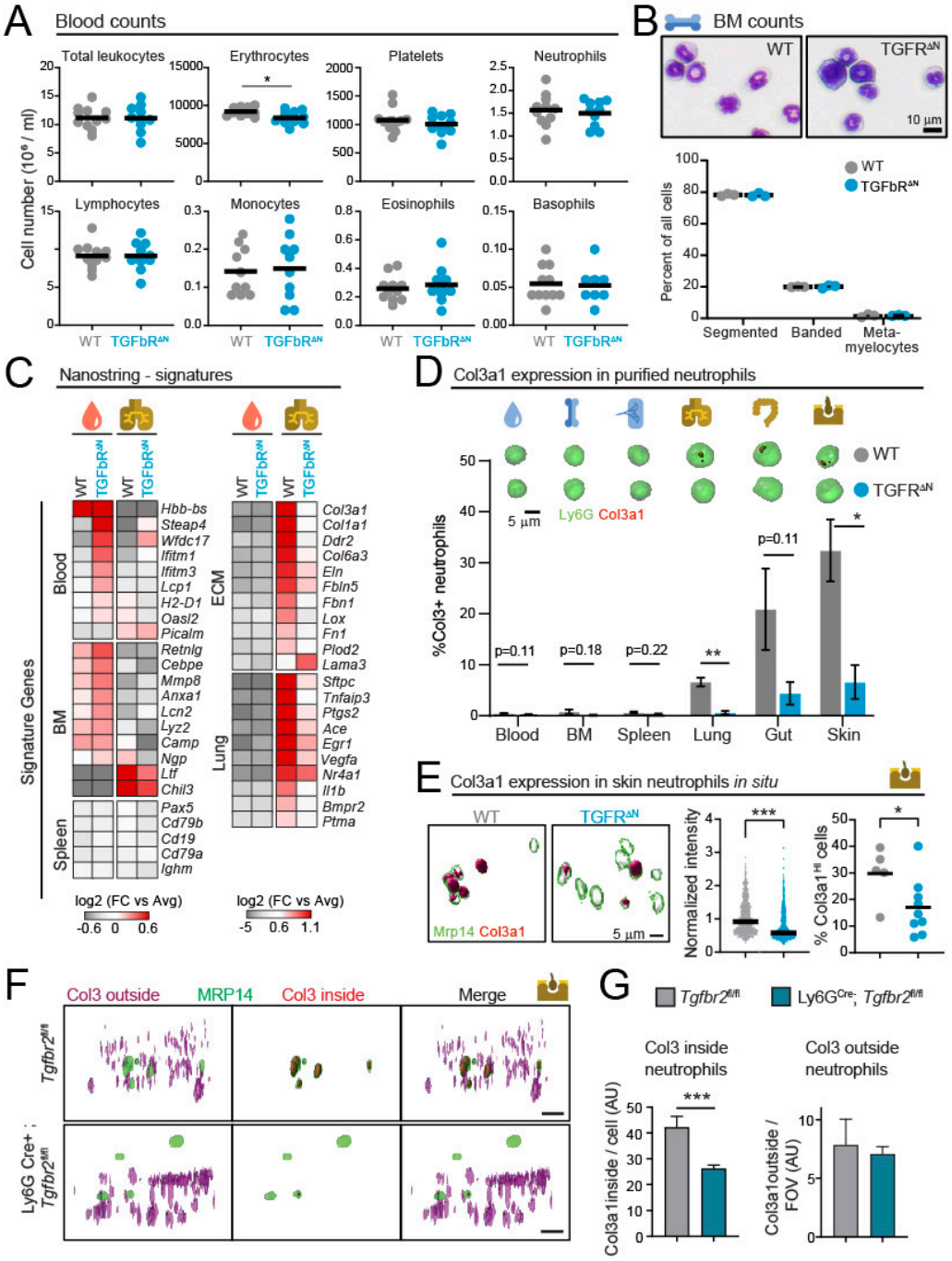

Extended Data Fig.8. Characterization of TGFbR$^{\Delta N}$ mice. (A) Blood counts in control and TGFbR$^{\Delta N}$ mice showing normal values for mice lacking neutrophil-specific TGFβ signaling. Data from 10 mice per group. (B) Characterization of granulopoiesis in TGFbR$^{\Delta N}$ mice showing segmented, banded and metamyelocytic stages as percentages defined by imaging of Giemsa stains of bone marrow samples. (C) Differential expression of genes associated with blood, bone marrow (BM), spleen and lung signatures as defined in (*3*), as well as genes associated with the matrix signature (ECM) as defined in Fig1A. Comparisons are for neutrophils extracted from blood and lungs of wild-type control and TGFbR$^{\Delta N}$ mice. Data is from 3 mice per group. (D) Representative reconstruction of neutrophils from the different tissues (top), and frequency of Col3a1+ neutrophils (bottom) extracted from tissues of wild-type control and TGFbR$^{\Delta N}$ mice. Data representative of 3 mice per group. (E) Col3a1 expression in neutrophils imaged directly in the skin of wild-type control and TGFbR$^{\Delta N}$ mice. Representative images (left), showing neutrophils detected using Mrp14 which was used to normalize Col3a1 expression across samples (normalized intensity, middle dot plot). Using relative Col3a1+ levels >2000 arbitrary units we stratified cells in tissues as Col3a1lo/hi and calculated the percent of Col3a1hi cells in each group, where bars show median values. Data from 5-9 images from 2-3 mice. (F) Representative images of Col3a1 expression inside and outside neutrophils imaged in the steady-state skin of Ly6GCre^{NEG} control and Ly6G Cre+; TGFbR$^{fl/fl}$ mice, showing neutrophils detected using Mrp14 (green), Col3a1 inside neutrophils (red) and Col3a1 outside neutrophils (magenta). (G) Quantification of Col3a1 protein inside neutrophils (left; 143-275 cells) and outside neutrophils (right; 11-17 images) from 2-3 mice. *, p<0.05; **, p<0.01; ***, p<0.001 as determined by two-tailed Student's t-test. All controls here are Cre-negative TGFbR^{flox} littermates.

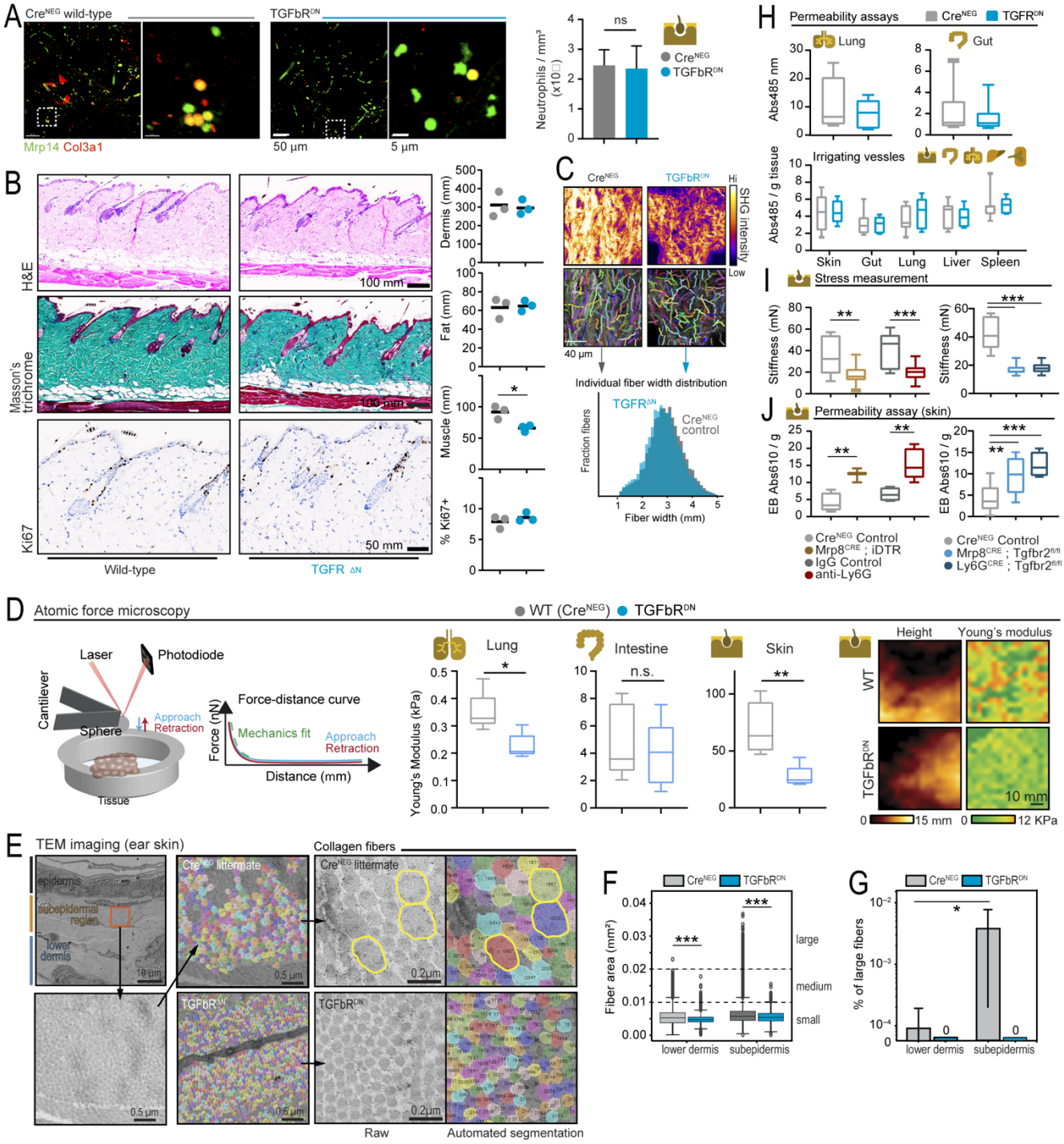

Extended Data Fig.9. Characterization of the skin of TGFbR$^{\Delta N}$ mice. (A) Representative images of neutrophils (green) stained for Col3a1 (red) in the skin of WT control (Cre^{NEG} TGFbR^{flox} littermates) and TGFbR$^{\Delta N}$ mice, which we used to quantify the number of neutrophils per volume area is shown at right; data are from 2-3 mice per group, compared by unpaired Student's t-test. (B) Histological characterization of the skin of wild-type control and TGFbR$^{\Delta N}$ mice by hematoxylin-eosin staining for cell and tissue structure, Masson's trichrome for collagen-rich structures, and Ki67 staining for dermal and epidermal proliferation. Images are representative of 3 mice per group and are quantified in the dot plot graphs below. *, p<0.05, unpaired Student's t-test. (C) Examples of SHG and fiber reconstruction using CT-FIRE for estimation of fiber width in control and TGFbR$^{\Delta N}$ mice also shown as distribution of widths in the histogram below (and in Fig.S5A for control vs. iDTR mice). All comparisons in (A-C) between both groups of mice used unpaired Student's t-tests. (D) Schematics of the atomic force microscopy (AFM) setup used to measure the stiffness of tissue samples (left) and its quantification in the form of elastic Young's modulus in lung, intestine and skin of Cre^{NEG};TGFbR^{flox} control (referred to here as WT) and TGFbR$^{\Delta N}$ littermates. Each dot represents the median Young's modulus value calculated from ~250 individual force-distance analyzed curves per mouse. Data is from 5 mice per group and compared by unpaired Student's t-test. Right, representative height images and corresponding Young's modulus maps of skin from control and TGFbR$^{\Delta N}$ littermates acquired by AFM indentation experiments. Images are representative of

5 mice per group. *, p<0.05; **, p<0.01 as determined by unpaired Student's t-test. (E) TEM images of the ear skin transversal sections showing collagen fibers in the subepidermal and lower dermis regions, which were automatically segmented for analysis (colored fibers). Yellow circles highlight large collagen fibers (>0.2μm^2) in the subepidermal region. (F) Quantification of fiber size in the skin of $TGFbR^{\Delta N}$ mice and Cre^{NEG} littermate controls; data is from 3,000-40,000 fibers from 2 independent experiments. (G) Percent of "large" fibers in the subepidermis and lower dermis of the same mice. *, p<0.05; ***, p<0.001 determined by Kruskal-Wallis non-parametric test. (H) Permeability assays in control and $TGFbR^{\Delta N}$ mice measured by FITC-dextran injected either intratracheally (lung) or by oral gavage (gut), or Evans blue given intravenously and then measured in the indicated tissues; data from 5-11 mice per group. All controls here were Cre-negative $TGFbR^{flox}$ littermates. (I) Stiffness and (J) permeability assay using Evans blue in the ear skin of $Mrp8^{CRE}$; *Tgfbr2*^{flox} and $Ly6G^{CRE}$; *Tgfbr2*^{flox} mice, as well as Cre^{NEG}; *Tgfbr2*^{flox} littermates, or mice treated with anti-Ly6G to deplete neutrophils or isotype control antibody. Data for is from 6-14 mice for the stiffness assays and 3-16 for the permeability assays. **, p<0.01; ***, p<0.001 as determined by two-tailed Student's t-test comparing each depletion method with their controls (left panels), or one-way ANOVA with multiple comparison test (right panels).

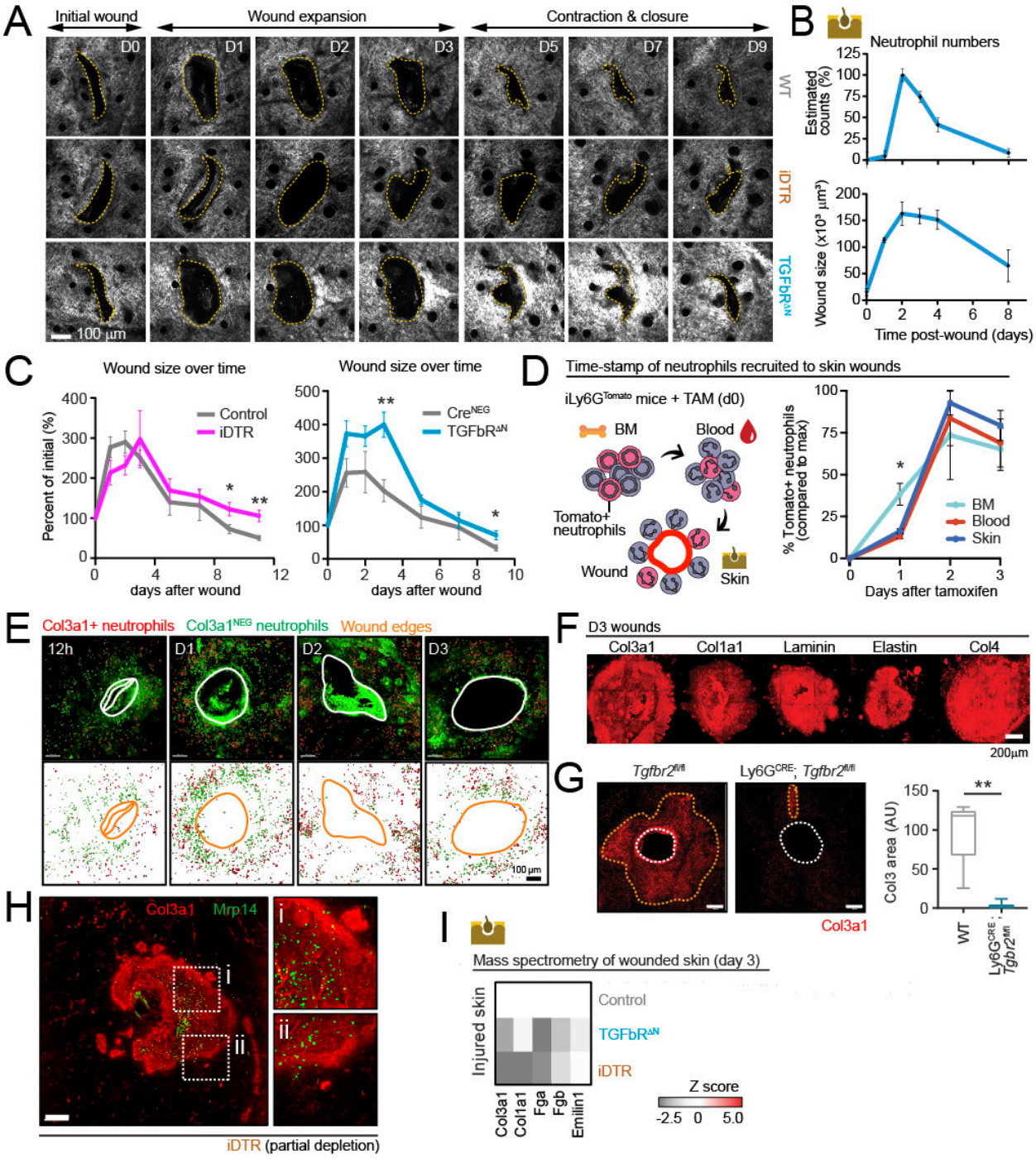

Extended Data Fig.10. Dynamics of the skin needle wound model. (A) Imaging of puncture-induced wound healing (days 0 to 9; D0-D9) as visualized by SHG acquired by multiphoton imaging of the ear skin from control (WT), iDTR and TGFbR$^{\Delta N}$ mice. Wound area is highlighted with yellow dotted lines. Note the different stages indicated on top. For simplicity, only Cre-negative *Tgfbr2*^{flox} littermates are shown as representative controls. (B) Kinetics of neutrophil counts in the wound estimated by confocal imaging and wound size (dotted areas in (A)) in control mice. (C) Kinetics of wound healing in controls and matched iDTR (left) or TGFbR$^{\Delta N}$ mice (right). Controls refer to the respective Cre-negative floxed littermates. Data from 2 ears per mouse and 3 mice per group, analyzed by unpaired t-test between the same time-points. (D) Left, scheme of in vivo neutrophil labeling in iLy6G mice to assess transit between tissues. Right, frequencies of CD11b+ Ly6G+ Tomato+ neutrophils in the BM, blood, and wounded skin of iLy6GtdTom mice at the indicated times after tamoxifen injection. Data are mean ± SEM from 2-9 mice per group. *p<0.05, determined by mixed effect model with Tukey's multiple comparison test. (E) Representative images of the skin at different times after generating a needle wound, showing the kinetics of neutrophils that express or not Col3. The quantification of these images are shown in Fig.4B. (F) Staining for the indicated matrix proteins around wounds on day 3. Images representative of at least 4 mice per group. (G) Representative images and quantification of Col3+ matrix rings around skin wounds in Cre^{NEG} control and Ly6G^{CRE}; *Tgfbr2*$^{fl/fl}$ mice at day 3, with quantification of Col3+ areas shown in the box and whisker plot at right. Data from 3-4 mice. (H) Image of a day 3 needle wound from the skin of iDTR mice with

incomplete neutrophil depletion, showing the spatial correlation between Col3a1 deposition and the presence of residual neutrophils. (I) Heatmap of proteomic analysis of wounded skin from control, iDTR and TGFbR$^{\Delta N}$ mice, with color scales showing z-scores. Control represents combined data from 2 Cre-negative floxed littermates for iDTR and TGFbR$^{\Delta N}$ mice, for a total of 4 mice per group. Note that because the quantification relies on the relative abundance of proteins for each sample, the strong reduction in the most abundant proteins (Col1, Col3, and Fibrinogens (Fga and Fgb)) results in an apparent increase in other less abundant proteins (e.g., Col2a1). *, $p<0.05$; **, $p<0.01$ as determined by two-tailed Student's t-test comparing the same time points between groups (C) or the two experimental groups (G).

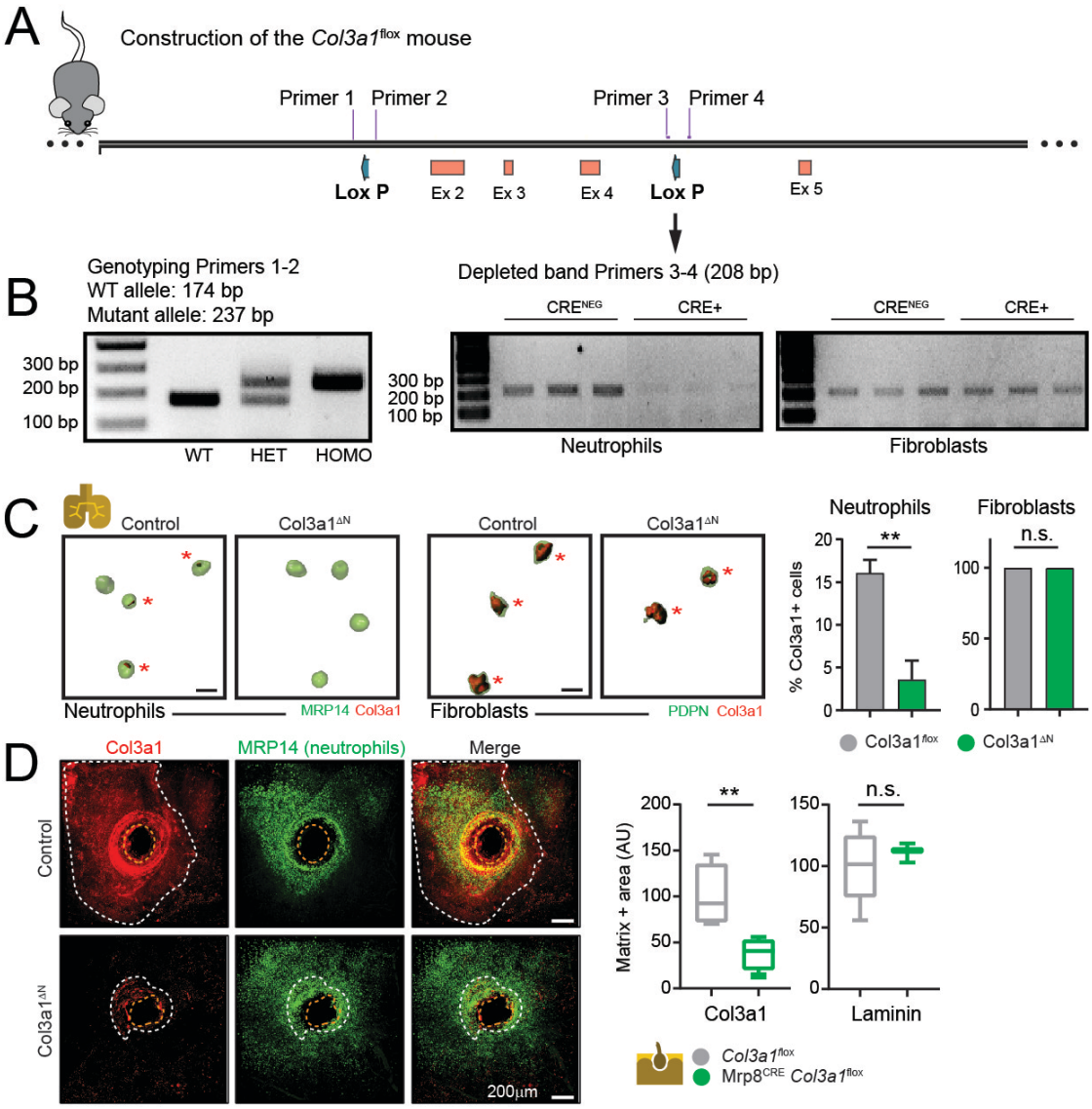

Extended Data Fig.11. Characterization of Col3a1$^{\Delta N}$ mice. (A) Schematic representation of the Col3a1$^{fl/fl}$ mouse gene construct. Exons 2-3-4 are flanked by loxP sites which are recognized as targets of DNA cleavage by Cre recombinase. Primers 1 and 2 are used for the genotyping. Primers 3 and 4 are used for detection of depletion of gene construct after crossing with the Mrp8^{CRE} driver line. (B) Genotypes of Mrp8^{CRE} Col3a1$^{fl/fl}$ (Col3a1$^{\Delta N}$) mice determined by PCR of genomic DNA using primers 1 and 2 that target the inserted loxP site (left). Deletion of the Col3a1 gene was confirmed by PCR of genomic DNA of lung neutrophils using primers 3 and 4 (right). Controls are Cre^{NEG} floxed neutrophils. DNA from lung fibroblasts was used as control for driver specificity. (C) Representative 3D reconstructions of MRP14+ neutrophils and PDPN+ fibroblasts stained for Col3a1, with Col3a1+ cells indicated with asterisks (left). Percentage of Col3a1+ neutrophils and fibroblasts extracted from lungs of Cre-negative controls and Mrp8^{CRE}; Col3a1$^{fl/fl}$ (Col3a1$^{\Delta N}$) mice (right). Data from 450-500 neutrophils and 100-150 fibroblasts from 4-5 mice per group. (D) Representative images and quantification of Col3+ matrix rings around day 3 skin wounds in the same control and Col3a1$^{\Delta N}$ mice. Right, quantification of Col3+ and laminin+ areas (from Fig.4H) is shown in the box and whisker plot. Data from 3-5 mice. **, p<0.01 as determined by two-tailed Student's t-test.

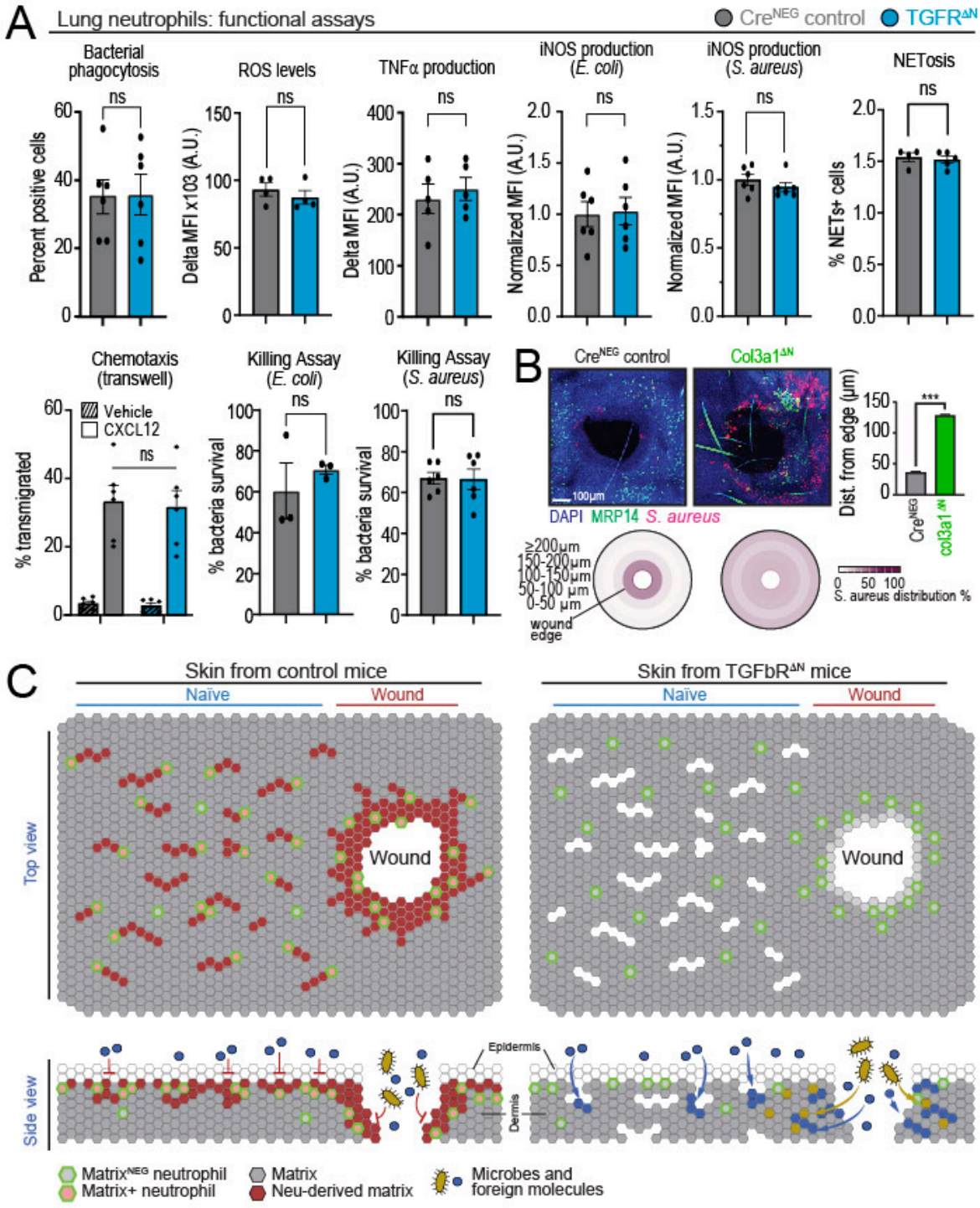

Extended Data Fig.12. Preserved antimicrobial activity of neutrophils from TGFbR$^{\Delta N}$ mice. (A) Functional assays to compare the immune-competence of lung neutrophils purified from TGFbR$^{\Delta N}$ mice against Cre-negative floxed littermate controls, including chemotaxis, bacterial uptake (*E. coli* phagocytosis) and killing and production of iNOS (for both *E. coli* and *S. aureus*), as well as ROS and TNFα production by flow cytometry, and NET release. Each dot represents one mouse, showing sample size for each assay (n=3-6 from 2 to 3 independent experiments). Data are shown as mean ± SEM. *, p<0.05; **, p<0.01; ***, p<0.001 as determined by two-tailed Student's t-test. (B) Representative images showing the spatial distribution of *S. aureus* 4 hours after exposure to wounds of Col3ΔN mice or littermate controls. Distribution is shown in radial plots and distances to the wound edge are quantified in the bar graph. Data is from 4 wounds from 3-4 mice per group. ***, p<0.001 determined by unpaired t-test. (C) Model of skin shielding by neutrophils in the steady-state or after a wound, highlighting the deposition of matrix components (collagen) and reinforcement of the subepithelial matrix in the naïve skin. Potential invasion of the tissue by foreign molecules or microbes in the absence of neutrophils or TGFβ signaling is depicted in the bottom scheme, which shows a side view of the skin. Not shown here are the contribution of neutrophils to matrix structure and tissue mechanics described in this study.

Legends for Supplementary Movies

Movie S1. 3D imaging of the naïve skin. Whole mount confocal imaging and 3D rendering of a representative immunofluorescence of the cleared naïve skin of a Ly6G^{CRE}; Rosa26^{Tomato} mouse, showing neutrophils (red), vessels (blue), Col3 protein (green) and nuclei (DAPI, grey). The video is from a representative ear skin of 5 mice analysed.

Movie S2. Spatiotemporal dynamics of neutrophils in live murine skin. Representative intravital microscopy sequences depicting tdTomato+ neutrophils (CatchUp mice) exhibiting distinct motility patterns and compartmental distribution: (A) intravascular trafficking within blood vessels and (B) interstitial migration through the collagen-rich extracellular matrix. (C) Side-by-side comparison demonstrating the dual-compartment neutrophil distribution in naïve skin. Colors: CatchUp neutrophils (red), second harmonics (teal), anti-CD31 injected IV (grey).

Movie S3. Quantitative analysis workflow of neutrophil-induced collagen remodeling. Sequential high-resolution confocal microscopy volumes (t0, t1) captured structural changes in the subepidermal collagen network, visualized through second harmonic generation (SHG). Initial volume acquisition was followed by deconvolution and 3D Frangi filtering to enhance fibrillar structures. Between timepoints, tdTomato+ neutrophil migration (CatchUp mice) was monitored using ultra-low, minimal-perturbation imaging parameters. Migration path reconstruction enabled comparative analysis of collagen reorganization through quantification of 3D Frangi filter intensities within and adjacent to neutrophil trajectories.

Movie S4. Time-lapse multiphoton intravital microscopy of Lyz2 GFP neutrophils around skin wounds. Ear skin was wounded in albino Lyz2-GFP mice with needlestick injury, and the wound regions were imaged repeatedly for 10 minutes each at the timepoints indicated (from Day 0 to Day 7). Neutrophils are observed to be highly motile on day 1 within the initial wound, but from day 2 onwards only those at the periphery of the wound remain motile. Video is representative of 4 independent mice and is looped three times. Each image: 450 um x 450 um, time lapse of 1 min between frames, maximal intensity projection of approximately 72 µm in Z-axis with 4 µm step size. (Green: Lyz2-EGFP neutrophils, Blue: SHG).

Movie S5. Structure of the matrix ring around wounds. The wounded ear skin from a wild-type mouse was explanted on day 3, fixed and stained for Col3a1 staining. Multiphoton imaging allowed the capture of second harmonic signal (grey) together with the Col3a1+ areas (orange). Video is representative of 4 independent experiments. The image is 950 x 950 µm and has a depth of 250 µm.